University of Glasgow

APPLICATION OF CONDUCTING POLYMER ELECTRODES IN CELL IMPEDANCE SENSING

By

Affar S. Karimullah

Submitted in fulfillment of the requirements for the

Degree of Doctor of Philosophy

School of Engineering and Science

University of Glasgow

November 2012.

"Everything you can imagine is real"

Pablo Picasso

I was never first in my class, but then they never measured my imagination.

Dedicated to my loving parents who have

never stopped believing in me…

Author’s Declaration

I declare that all the work presented in this thesis has been carried out by me, unless otherwise acknowledged or referred to.

Affar S. Karimullah

November 2012

Abstract

Research in label free methods for biological analysis has brought interesting developments. Cell impedance spectroscopy has been one of the promising outcomes. It allows the measurement of cell proliferation and motility whereby it is possible to study wound healing and cell behavior *in vitro*. This thesis presents the progress towards an 8-well impedance measurement setup that uses conducting polymers as electrode material in cell impedance spectroscopy. A step by step fabrication of devices with PEDOT:PSS electrodes is described along with the hardware and software, developed and integrated, to perform impedance measurements of cell cultures.

Electrochemical analysis was performed for PEDOT:PSS and Au electrodes to compare the two materials for use in cell impedance spectroscopy. PEDOT:PSS electrodes showed lower interfacial impedance and reach electrochemical equilibrium faster than Au electrodes. It was observed through electrochemical impedance analysis that the lower interfacial impedance is due to the low charge transfer resistance of PEDOT:PSS. MDCK cell proliferation experiments were performed using both types of electrode materials to provide a comparative study. The impedance measurement results showed differences between the two materials that led to a different kind of electrical model for the changes measured due to cell proliferation. Curve fitting results to the electrical model provided an understanding of the cell-substrate interactions and the capabilities of cell impedance spectroscopy.

The application of cell impedance spectroscopy to human embryonic stem cells was also explored. The impedance changes of pluripotent stem cells during differentiation to trophoblasts were measured and analyzed. Analysis of changes to the phase values in the frequency spectrum show that by measuring the frequency where the phase is minimum, it is possible to distinguish between the two cell types. It provides a new method of using cell impedance spectroscopy to study stem cells behavior in real time and help researchers in the maintaining of stem cell cultures in the lab. Another new application of cell impedance spectroscopy to determine cell types based on the flexibility of the cytoskeleton was also explored. Some preliminary data is presented in the last chapter.

Acknowledgement

I would like to thank my supervisor, Dr. Nikolaj Gadegaard, for his immense support and faith in me. He gave me a chance to prove my abilities in research and was always a door knock away for discussions and help, literally. Though I might have bored him at many times with my daily reports, his kind words and appreciation always helped my motivation and dedication to my project. I always aimed to live up to his expectations and I hope to continue collaborating with him in the future on more research projects.

I would like to thank Prof. David R. S. Cumming and Dr. Helena Gleskova for their support as my advisors during my Ph.D. We never really got on to creating biosensors with organic electronics but I have plenty of time in m career and I still have not given up on that idea. I hope neither have you two. There is no way I can forget all the guys in the Biomedical and Nano group (I won't be surprised if we have renamed it by now). Thank you to Ali and Ainhoa, the first two people from the group that I met and who helped me with my project. Johnny and Rasmus, you have been my oldest colleagues and friends at the University. It was great to have your company in that huge office. Thank you to Paul, Alex, Daniel, Andy, Elena, Alistair, Kiryl and all those who joined later as well. It was great to have more company. I will miss our crazy discussions, "*Star Wars*" chatter on the clean room radios and the football. Thank you for all the help with my work and being part of a great time during my studies. You all really made it fun to be at work.

I believe I owe plenty of thanks to the folks in CCE (center for cell engineering). Dr.Mathis Riehle for his immense support and advice whenever I needed it. His ideas were unique and I hope we can continue exploring them. Prof. Adam Curtis and Prof. Chris Wilkinson, you two were the titans of cell biology and research for me and I was always encouraged by you. I still remember talking to Adam every now and then and he was always happy to answer my questions in the most eloquent manner. Chris, your very trip to Nikolaj's office and our discussion on this project provided me with a lot of encouragement and I wish you were still here so I could present my results to you and discuss them with you. I would also like to thank Abhay, Stephanie, Lewis, Andy Hart, Carol Anne, Theo, Laura, Hannah and Monica. You all were great help throughout my time in CCE, teaching me biology and helping me out with my cell culturing and

experiments. I really enjoyed your company and support. Than k you to Scott Cowan who collaborated on the hESC research and the squash matches on Monday mornings.

I spent a lot of time in the engineering department and would like to thank all the guys in the level 2 labs. Pete Shields (will miss your classical music), Balazs Nemeth, Peter MacPherson, Chris, James and Anne. You guys were great help whenever I needed it and when I was ranting about my failing experiments. Thank you for being patient. The staff in the Rankine building, especially Bill Monaghan, Stewart, Alan, and Shona. I would also like to thank Prof. John Weaver for his help initially regarding my electronics design. All the staff of the JWNC clean room especially Donald and Linda for teaching me the basics and always solving my problems and helping me out.

Thank you to my wife Saba, for her love, support and help during my studies, especially with the explanations about biology and cells. I would also like to thank Sabs's parents for their love and support for my work over the years. Thank you to all my friends, I have enjoyed our sports, video gaming and silly nights out. A special thanks to Zeeshan who was always ready to help and has guided me throughout my senior resident job and postgraduate life.

Finally, thank you to my parents who have been essential to my journey till this point in time, and beyond. Your efforts towards instilling good behavior, good work ethics and always pushing me academically have brought me here. I will never forget your sacrifice and desire to make me better. I owe you everything, my education, my language skills, and a great childhood.

Experiments to test the compatibility of PEDOT:PSS with astrocytes and neurons were done in collaboration with Lewis Ross, and Stephanie D. Boomkamp where they cultured the cells on samples provided by me and performed the subsequent staining and imaging. The seeding, culture maintenance, staining and imaging for the human embryonic stem cell experiments were done by Scott Cowan. AFM images were taken by John S. Darling of my samples and Paul Reynolds helped with images of the embryonic stem cell experiment on microstructured gold devices.

This work was made possible by the funding of *Glasgow Research Partnership in Engineering (GRPE)* and the *Scottish Funding Council*.

Publications and Presentations

1. Affar S. Karimullah, David R. S. Cumming, Mathis Riehle, Nikolaj Gadegaard, *"Development of a Conducting Polymer Cell Impedance Sensor"*, Sensors and Actuators B: Chemical (2012) doi:10.1016/j.snb.2012.09.075
2. *"Cell Impedance Spectroscopy Using Conducting Polymer Electrodes"*, Glasgow Orthopedic Reseach Initiative, GLORI 2012, conference.
3. Poster presentations at GRPE conferences in 2009 and 2010

Contents

Table of Contents

List of Figures

List of Tables

Abbreviations

AFM	Atomic force microscopy
ATP	Adenosine triphosphate
BMP 4	Bone morphogenetic protein 4
CIS	Cell impedance spectroscopy
CPE	Constant phase element
DNA	Deoxyribonucleic acid
ECIS	Electrical cell impedance sensing
ECM	Extra cellular matrix
EIS	Electrical impedance spectroscopy
FEM	Finite element method
hESC	Human embryonic stem cells
HS	HEPES saline where HEPES is *4-(2-hydroxyethyl)-1-piperazineethanesulfonic acid*
IPA	Iso-propanol
MDCK	Madin-Darby canine kidney
PCR	polymerase chain reaction
PEDOT	Poly (3,4 ethylenedioxythiophene)
PLL	Poly-L-lysine
PMMA	Poly (methyl methacrylate)
PSS	Poly (styrene sulfonate)
PPy	Polypyrole
RO	Reverse osmosis
RPM	Revolutions per minute
SEM	Scanning electron microscopy
UV	Ultraviolet
VI	Virtual Instrument

Chapter 1: **Introduction**

The human race is distinguished for its intellect, curiosity, and creativity. Where once an artificial heart or a fully walking robot were anything but a dream, today they are realities. The history of our endeavors in science, provide us with a constant belief that we can achieve more. We recognize that our knowledge of the laws of Nature and how it works are not complete. Many times we have mimicked Nature or developed tools that work on the very basics that drive it. The human body is perhaps one of the greatest pieces of complexity devised by Nature. What better melting pot of chemistry, physics, and mechanics to explore than ourselves. We have studied our bodies to know how to repair them, enhance them and simply understand how they work for many centuries and have achieved a lot over that extensive time. The understanding of mammalian cells and their working over many years have enabled us to cure diseases and perform techniques like genetic engineering and cloning. It is vital to biologists to be able to understand more about the response and behavior of cells during experiments. Techniques such as fluorescent staining, polymerase chain reaction (PCR) analysis, scanning electron microscopy and various optical microscopy techniques, to name just a few, have been paramount to biologists over many decades. Development of such research tools is essential to the development of cell biology.

The need for label free and real time analysis in cell biology is constantly increasing. While traditional techniques of staining and chemical analysis are still the mainstay of biological analysis, there is a need of analyzing biological experiments without destroying the samples. Furthermore, there is a need to be able to know more about the processes and cell behavior as they progress through time such as measurement of wound healing rates and drug toxicity. The nature of cell biological research also requires parallel experiments in large numbers that yield cumulative statistical results. Research to meet these demands has led to many technological advances in fields such as lab-on-chip devices and instrumentation that process large work intensive experiments in a factory line style. Most lab-on-chip devices still require cells to be labeled before analysis [1]. Novel ways of detection along with parallel processing are required which do not interfere with the cells in culture. Electrical cell-substrate impedance sensing (ECIS), a method pioneered

by Giaever and Keese [2] , provides such a possibility. ECIS has been an evolving label-free tool for over two decades. It allows cells to be monitored *in vitro* and data can be collected for multiple experiments in parallel. Early research showed that the method could not only be applied for cell proliferation and motility measurements, but also be used to assess morphological characteristics (confluence of the cells) and behavioral aspects (such as metastasis) of the cells [3, 4]. With the addition of multiple frequencies, some have termed it a spectroscopic technique and called it cell impedance spectroscopy (CIS). The applications and research for CIS have been growing rapidly including in field toxicological studies [5], drug testing [6], measuring mesenchymal stem cell differentiation [7-9] , the measurement of cell substrate separation [10] and the monitoring of relaxation and contractility of muscle cells [11]. Electrodes for CIS have predominantly been based on noble metals. Conducting polymers have been researched thoroughly for antistatic coatings, electrodes (electrochemical capacitors [12], electrochromic devices, ion sensors [13]) and have been instrumental in new forms of biosensors. [14].

Conducting polymers were first reported in the mid 20th century [15-17] but it was the discovery by Shirakawa *et al*. in 1977 that is considered the highlight for their discovery of polyacetylene [18] and earned him, along with Alan J. Heegar and Alan G. MacDiarmid, the Nobel Prize in chemistry in 2000. By the 1980's organic semiconductor based FET's were made possible and polymer field effect transistors in 1988 by R.Friend and colleagues [19]. Organic light emitting diodes were already under research before the discovery of polyacetylene and now the field of organic electronics is under heavy investigation by researchers [20]. The combination of conducting polymers, organics/polymer light emitting diodes and organic/polymer semiconductors for transistors has spewed out remarkable applications such as transparent flexible screens and plastic touch screen displays. There is a lot of room for further development and understanding about the materials and their mechanics as well as room for growth in their applications. The conductivities of many types of conducting polymers are low for most of the current electronic applications, however many biomedical applications do not have such a requirement. The characteristics and flexibility of applications with conducting polymers makes them very useful in biomedical applications. The fact that conducting polymers are organic materials, flexible, chemically/structurally alterable, versatile, inexpensive and can be fabricated on various organic substrates gives them a great advantage over metals. It also opens the doors to new ideas and methods for sensing applications.

Polymer	Conductivity (S/cm)	Stability	Applications in Biomedical
Polyacetylene	10^4	Poor	
Polyphenylene	500	Poor	
Polypyrole (PPy)	100-200	Good	Tissue Engineering, neural probes, drug delivery, bio-actuators, amperometric sensors
Polythiophene	100-200	Good	Neural process, tissue engineering, drug delivery, micropumps
Polyanaline (PANI)	**10**	**Good**	**Tissue Engineering, bio-actuators.**

Table 1: Table of different conducting polymers, their conductivities (from [21, 22]) and some applications in biomedical research.

The application of conducting polymers in biological research are numerous and they are being extensively used for tissue engineering, neural probes, biosensors, drug delivery and actuators [22]. Their conductivity, hydrophobic characteristics and reactive functionalities can be tuned. This allows them to be used in applications like detecting binding events[22], timed release of drugs [23], drug delivery [24] ,tissue engineering[25, 26], neural probe applications [27-29], bio-sensors [30-32], bio-actuators[33], electrochemical DNA sensors[34] and new form of ion pumps used for micro fluidic delivery in implants[35, 36]. They can be modified using physical adsorption, entrapment of molecules, doping (can be done during synthesis of the polymers), and covalent attachment. Such modifications have allowed biomedical engineers to use conducting polymers as a form of tool for sensing, enhancing adhesion and proliferation and also improve their biocompatibility [14, 22]. Their mechanical properties can also be varied by various means including addition of other polymers or addition of molecules to their backbones [37]. One of the most common uses is in transducers that pick up signals produced by elements such as enzymes for biological sensing applications. These could be based on measuring current, voltage, resistance, absorbance or emission spectra or mechanical variations.

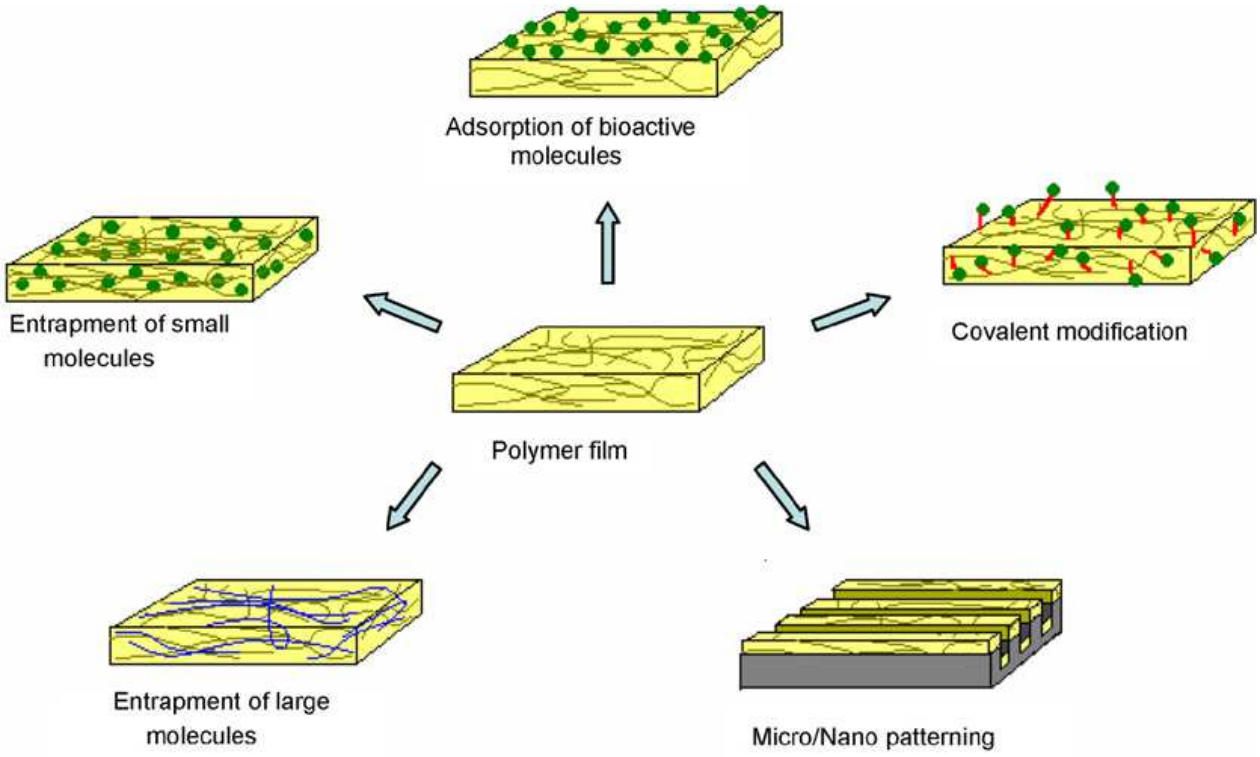

Figure 4: Modification strategies used with conducting polymers. From Guimard *et al* [22].

Polypyrole (PPy) has often been used for biosensor applications. In 1994 Wong, Langer and Ingber studied cell attachments on PPy films and their dependence on the proteins in the media by excluding the serum. It was also found that by varying the electrochemical state (by means of applying potential) cell adhesion and shape differed. Thus giving conducting polymers a new useful property [25]. Commercially available conducting polymers, such as poly(3,4-ethylenedioxythiophene) (PEDOT), are commonly used as conductive coatings and intermediate layers in organic electronics [38]. PEDOT has the advantage of being transparent and biocompatible [32, 39] while being considered the most stable (in the atmosphere and oxidizing environments) conducting polymer currently available [40-42]. It allows for simple and flexible methods for patterning, and also has the ability to be blended with other polymer compounds to create novel materials with unique properties [43, 44]. By using lithography techniques and inkjet printing, it is possible to create printable, inexpensive, flexible and simple electrodes for biological experiments.

PEDOT has been found to retain its conductive properties better than PPy in an aqueous environment [28, 45, 46]. PEDOT has been proven to have good electrochemical stability in phosphate buffer solutions, even when polarized [46, 47]. It has been studied as a neural electrode coating and is considered one of the promising new materials with higher charge injection limits and better signal to noise ratio in measurements of neural

activity. [48-50]. However it suffers from delamination [28] and variation in its conductive properties which are not always linear nor necessarily follow any pattern which could be expressed mathematically. Thaning *et al*'s study [28] on the stability of PEDOT showed that the delamination depends on the substrate the PEDOT layer is coated on, however during the course of my work I have found that delamination might also be dependent on the thickness of the layer and the dimensions of the structure. The delamination occurs over a period of a few weeks when in a saline solution [47]. Reza *et al*. [51] found PEDOT nano tube based coatings, on their neural electrodes, have improved adhesion to the substrate and the lower impedance provides better neural signal recordings. They also found that the material improved the neural attachment and neurite outgrowth [52] and by coating an electrospun biodegradable polymer (loaded with drugs) with PEDOT, they were able to use electrical stimulations to release these drugs [53]. Furthermore, Hansen *et al*. have been able to integrate PEDOT with PDMS substrates to create a more mechanically strong and adhesive conducting polymer network which can also be considered for creating the electrodes.

Most CIS setups work at frequencies where the higher impedance of metal electrodes is of little concern. However lower frequencies can contain information useful for curve fit analysis and possibly distinguish the cell type. Not only can PEDOT as an electrode material for CIS to provide a lower interfacial impedance but due to its transparency, cells are accessible to high resolution microscopy, which makes this a well suited material for this application. This thesis presents the development of a cell impedance measurement device that utilizes PEDOT:PSS (solution processable PEDOT with poly(styrenesulfonate) (PSS) as doping agent) as the electrode material. The devices were fabricated using photolithographic methods and a complete impedance measurement setup was implemented using Labview, which provides more flexibility in the device design and data analysis. A multiplexer was also designed and implemented for a multi-well device that allows me to measure eight experiments in parallel. The design has the same electrode connection lengths, ensuring, that results for all the wells are not impacted by variations in inductance and series resistance of the material. The design shows the possibilities of creating simple and cost effective polymer based cell impedance measurement electrode devices.

The electrodes were characterized and compared to Au electrodes. Impedance measurements with 4-(2-hydroxyethyl)-1-piperazineethanesulfonic acid (HEPES) saline solution showed a lower interfacial impedance (at frequencies below 1 kHz) of PEDOT:PSS electrodes in comparison to similar sized and shaped Au electrodes,

highlighting the electrical advantage of PEDOT:PSS as an electrode material. Through electrochemical impedance analysis and curve fitting of the results to Randle's theoretical model [54] of an electrode-electrolyte interface, I determined that the lower charge transfer resistance of PEDOT:PSS as compared to Au is the reason for the reduced interfacial impedance. Experiments with the epithelial Madin-Darby Canine Kidney (MDCK) cell line showed that the PEDOT:PSS electrodes were fully capable of being used for CIS. Due to the fast charge transport capabilities of PEDOT:PSS, the electrodes quickly reach their equilibrium state. Curve fitting of the experimental data to typical electrical models of biological cells in series with the electrode equivalent circuit, show the versatility of CIS as a method to observe not only cell growth but also the cell-substrate interaction.

Human embryonic stem cells (hESCs) were first isolated in 1998 [55] and have become a hot topic for research due to their potential. Their most important property is their pluripotency, that is their ability to differentiate into almost any type of cell. Adult stem cells can only differentiate in relation to their particular germ layers (multipotent). Another advantage of hESCs is that extraction of adult stem cells can be problematic and they tend to loose their multipotency if cultured for too long. The extraction of adult neural stem cells is far too risky and it can be difficult to pinpoint where to extract them from. In such cases hESCs can help provide stem cells to derive into neurons and related cells for research and health care applications. However they can be hard to maintain and require strict conditions to maintain their pluripotency. They must be well monitored and their pluripotency can be checked by staining for transcription factors (Oct4, Sox2 or Nanog) that maintain the pluripotency by inhibiting the genes that cause differentiation [56]. It would be highly beneficial to be able to monitor hESC cell cultures in real-time without the need for staining [57]. Bagnaninchi *et al*. [44] used ECIS systems from Applied Biophysics to monitor differences between adipogenic and osteogenic induction, adipose derived stem cells. I have used hESCs and induced them using BMP4 to differentiate into trophoblasts and monitored their impedance changes during the induction. Analysis of the frequency spectrum shows changes in the phase peaks that can possibly be used as an indicator of the cell type.

Chapter 2: **Theory**

2.1 **Conducting Polymers**

There are a vast number of semiconducting and conducting organic materials that are produced and characterized. The basis of their conductivity lies in the particular bonding arrangement, the alternating single and double bonds along the polymer chain. This type of arrangement is called a conjugate bond and thus the name for these materials, “Conjugated Polymers”. Before we understand this conjugated bonding in detail we need to look at carbon’s hybrid orbitals.

Electrons are arranged in orbitals around a nucleus. These orbitals are regions where the probability of finding the electron is high. Each orbit is a subunit of a shell. Each orbit is described by its shell number (1,2,3 etc) its orbital type (s,p,d) and if a hybrid type, it will have a power value which describes how many of that orbital type, are part of that hybrid (sp^2, meaning one s joined with two p orbitals). The last shell is called a valence shell. According to Pauli’s exclusion principle, each orbital can have a maximum of 2 electrons and those electrons must be of opposite spin. In the case of carbon, it has 4 electrons in its valence shell (shell 2). These are arranged as shown in Figure 1 (a). By looking at this configuration we would assume that the 2s orbital has reached stability and has no need for bonding, thus it would only make two bonds. However this is not the case in reality and carbon quite often makes four bonds. This is due to the fact that carbon makes hybrid orbitals of various types depending on the type of bond it will make. In the case of conjugated polymers it will make a sp^2 hybrid orbital by combing one s orbital and two p orbitals in its valence shell. The new configuration of electrons is shown in Figure 1 (b). The $2p_z$ orbital is left un-hybridized.

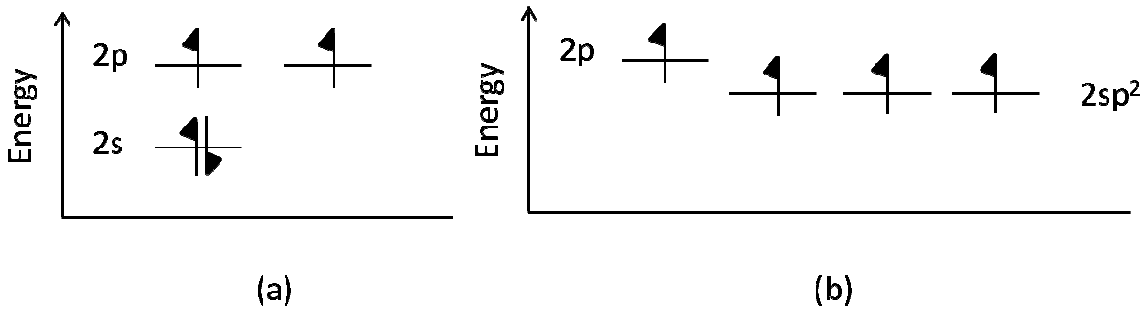

Figure 1: Electron configuration of carbon valence shell. (a) Basic configuration, (b) with sp2 hybridization.

Let's consider the example of ethylene (C_2H_4). Two of the $2sp^2$ orbitals (one from each carbon atom) will form a σ-bond. The other four $2sp^2$ orbitals (two from each carbon atom) will form covalent bonds with hydrogen atoms. The remaining un-hybridized $2p_z$ orbitals (one of each atom) will overlap with each other, forming a π (pi) bond, and hence the two carbons form a double bond, that is one σ bond and one pi bond. Figure 2 shows a representation of this behavior. [58]

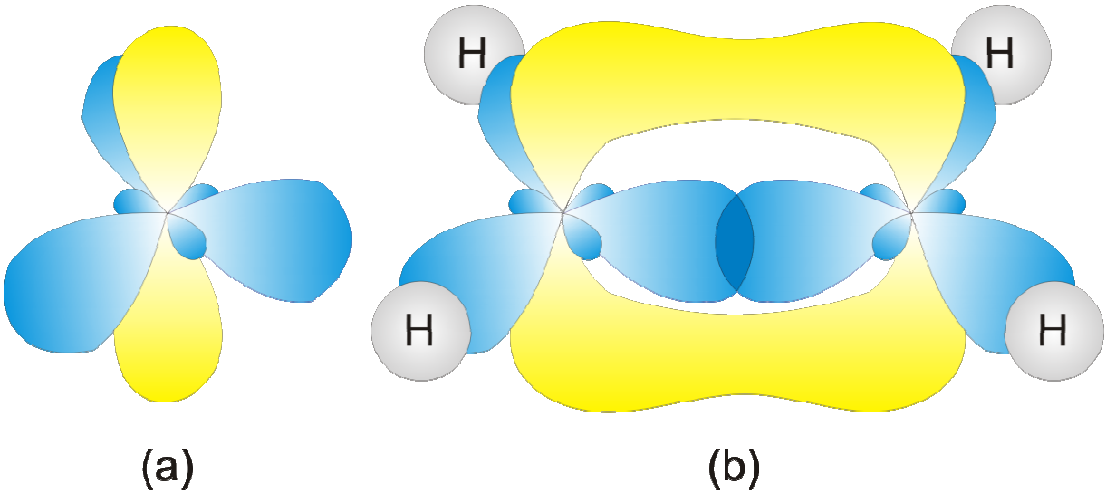

Figure 2: (a) 3D representation of hybridized orbital in a carbon atom. (b) Delocalized orbital in a carbon carbon bond. The p_z orbitals are yellow in color and the blue orbital are the sp^2 hybrid orbitals.

In cyclic conjugated systems such as benzene, these π-bonds are shared by the carbons in the chain. They are not "fixed" to a single atom and are shared by constantly alternating double and single bonds between the carbon atoms, also termed as "delocalized". [59]This provides the basis for conduction in conjugated polymers. Similar to semi-conductors, there is a valence and conduction band for pristine conjugated polymers. These are the π-band (highest occupied molecular orbit, HOMO) and the π*-band (lowest unoccupied molecular orbital, LUMO). The energy difference between the two provides us with the band gap of these materials and gives rise to the semiconducting

properties of conjugated polymers. By adding other chemical substances, termed "*doping*", these materials we can create conducting polymers. While inorganic semiconductors produce donor energy levels close to their conduction or valance bands (when doped), conjugated polymers have a different conduction mechanism. They rely on charge storage along the chain. When ionic compounds are used as dopants, they will cause delocalization in the polymer. As such localized states are formed along the chain where stable defects are present. Such a mechanism gives rise to quasi-particles called solitons, polarons and bipolarons. Solitons are un-charged and are a local confinement of the generally delocalized conjugation. This confinement is caused by a deformation in the polymer chain. It can only occur in polyacetylene due to the nature of the chain in the material. The polaron is a similar confinement but occurs due to the addition of an extra charge carrier, radical anion or cation to the polymer matrix. The introduction of a radical requires higher energy than the rest of the neutral chain and thus limits how many chain lengths the distortion occurs over. Further addition of dopant will generate bipolarons. Each deformation creates energy levels in the band gap [60]. As more and more bipolarons are introduced into the chain, continous bipolaron bands will form and eventually lead to overlapping of the band gaps causing metallic like conductivity [59-61].

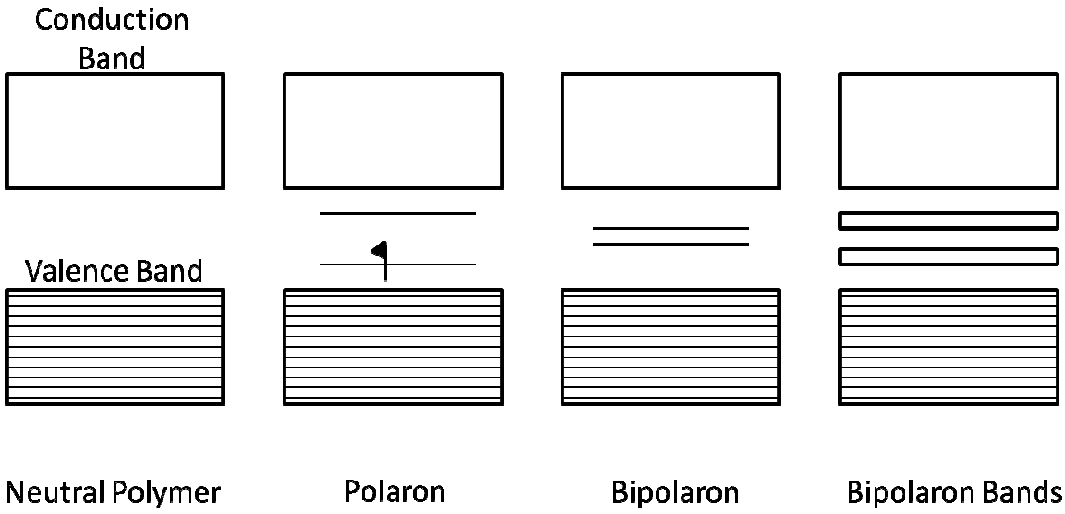

Figure 3:Energy bands of different states of a conjugated polymer with variation in states. [59]

Although polarons and bipolarons are known to be the reason for conductivity over the chain, the exact mechanism is still not known. Mott's variable range hopping (phonon induced hopping) model describes how charges move from one localized state to another. Other models use band theory and delocalization over the entire chain. Conduction in conjugated polymers decreases with lower temperatures and thus fails to imitate metallic behavior ruling out perfect delocalization. Another issue to consider is the fact that these

materials are highly disordered. The exact theories on how conduction occurs in organic material are still widely debated. Though the variable range hopping model is perhaps the most commonly accepted mechanism, it may well be that every type of organic conductor or semiconductor will have its own mechanism or a hybrid of various types [62].

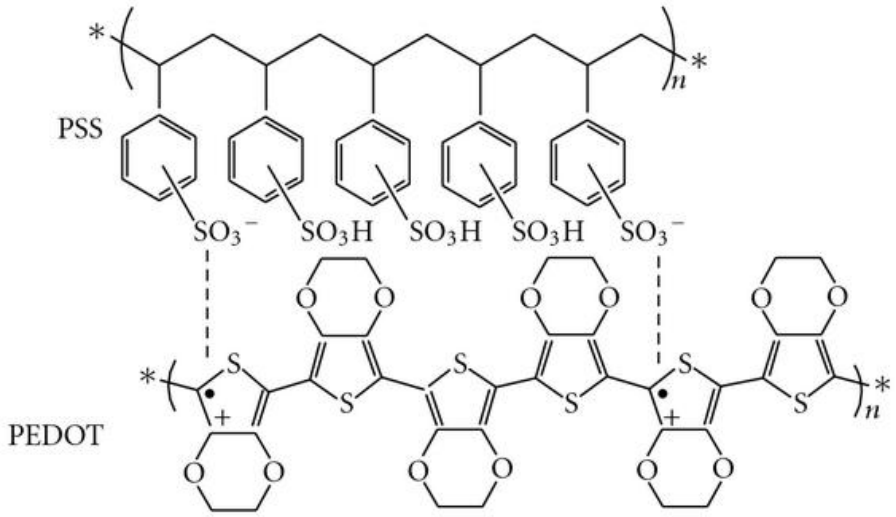

Figure 4: Polaron formations in PEDOT:PSS. Figure from *"On the conductivity of PEDOT:PSS thin films"*, thesis by A. M. Nardes [61].

PEDOT:PSS (poly (3,4 ethylenedioxythiophene) : polystyrene sulfonate) is one of the well known conducting polymers that is commercially available. PSS acts as the dopant and also allows solubility in water allowing the polymer to be spin coated. PSS is an anion and causes the solution to have a low pH. The PEDOT:PSS solution is a colloidal solution where the PSS surrounds the PEDOT chains. When dry powder PEDOT:PSS is immersed in an aqueous solution, the hydrophobic PEDOT will automatically orient itself in such a way that the hydrophilic PSS is on the outside of the colloidal micelle like particle. The size of this particle in solution and the conductivity of the polymer layer after coating will depend on the temperature the solution is at during the spin coating [63, 64]. PEDOT:PSS is used for anti-static coatings, as hole-injection layers in organic light emitting devices and in electrochromic devices. For a conducting polymer, it is highly stable in atmospheric conditions, which is a problem with most organic conductors and semiconductors. It also shows good thermal, electrochemical and electrical stability over time and in various conditions. PEDOT:PSS is a highly disordered polymer and is amorphous. It forms small globular groups of PEDOT surrounded by PSS rich layers [65, 66]. Figure 5 shows the AFM results of a PEDOT:PSS film spin coated on to glass. It shows high surface roughness.

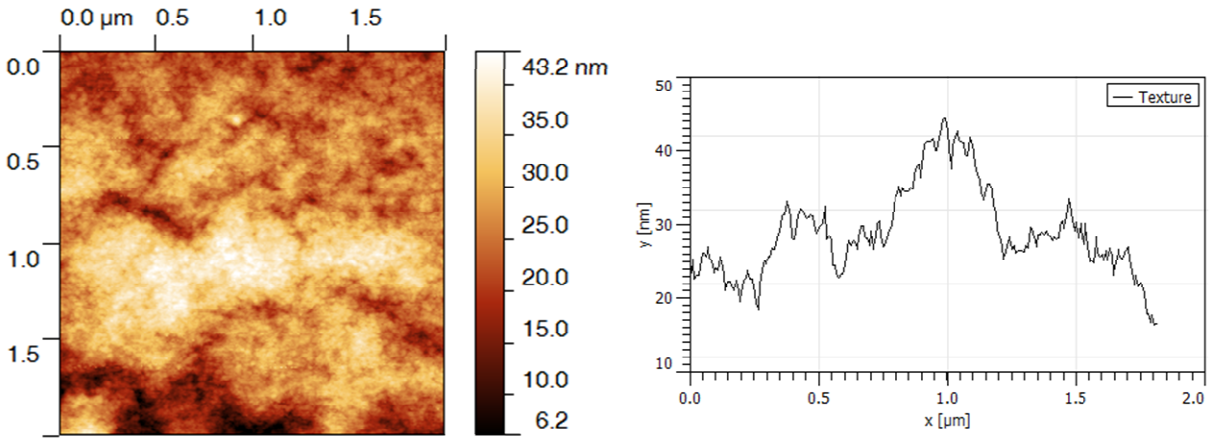

Figure 5: AFM results of a PEDOT:PSS spin coated on a glass slide. The roughness graph was generated for the data along a path down the middle (1µm mark) from top to bottom.

Additives such as DMSO (dimethyl sulfoxide), ethylene glycol, sorbitol and glycerol can be added to PEDOT:PSS to improve its conductivity by as much as 100-300 folds [67-69]. This has led to improvements in photovoltaic and other organic electronic devices. There are different theories as to why this occurs. One states that the PSS molecules surround the PEDOT chains and reduce its overall conductivity. PSS has also been known to move towards the surface and generate PSS rich surface layers. Thus these highly polar additives help reduce the PSS enrichment at sites and give charges access to the highly conducting PEDOT layer [70, 71]. Kim *et al* state that the screening effect of such additives between the counter ions and the polymer chain are the cause of improved conduction [72] while Inganas *et al* consider such additives to act as plasticizers [73]. Another theory is related to the fact that additives change the morphology of the polymer once heated. This is due to the reorientation of the chains and the change in the chemical structure of the PEDOT. The chain varies from a benzoid to a quinoid structure which allows delocalization over the entire chain increasing carrier mobility [74]. Hsiao et al looked into all the theories and deduced that while the observations shows that all of these effects were taking place, phase segregation of PEDOT and PSS domains had the major influence into increase in conductivity due to the additives [68]. Addition of surfactants has also been found to improve conductivity of PEDOT:PSS [75].

The PEDOT:PSS used in my experiments was acquired from AGFA under the product name of Orgacon. I used the IJ1000 ink for inkjet printing and S203, S305 plus for the spin coating processes. S305 plus was a later version of the S203 and had better adhesion and stability properties due to further surfactant addition, albeit the layers were

thinner and had higher total resistance as a consequence. The S305 plus solution has 0.54 % (by weight) PEDOT:PSS and includes ethylene glycol (EG) along with surfactants and stabilizers to improve its properties.

2.2 **Electrode Impedance Theory**

The moment a metal comes into contact with a liquid, it will go through a process of charge transfer and adsorption with particles (ions and molecules) in the electrolyte. These interactions are highly dependant on the conditions and the energy levels of the electrode and electrolyte. The interface eventually reaches a balance (net charge flow into the electrode and out of the electrode is equal). The balance can change depending upon external potential applied to the electrode. However such electron transfer is not in our interest for cell impedance sensing as this can cause an unwanted chemical change in the biological system being studied. Hence for that reason we will use impedance spectroscopy techniques, with low alternating current (AC) signals to perform measurements that are discussed later.

The second interaction that occurs is due to the process of adsorption and desorption, the so called non-Faradaic processes. When there is no charge transfer across the interface, then an ideally polarized electrode is formed. However there are very few practical cases that come close to this ideal (some liquid metal electrodes and some gold electrodes)[76, 77]. In all cases however the adsorption creates what is called the electrical double layer and any charge transfer occurs inside this layer. The entire system that includes the anode and cathode is called a cell and when only one electrode is looked at, we call it a half cell which is relevant to this study.

2.2.1 ***Electrical Double Layer***

The metal surface will accumulate charge on its surface and the net polarity will depend on the charge transfer that occurs (if any) and the type of ions/molecules that are present in the solution side of the system. The solution side of this interface will have two regions defined as the inner and outer Helmholtz layers. The inner Helmholtz layer (also called the inner Stern layer) is formed by specifically adsorbed ions and molecules. The outer Helmholtz layer consists of solvated ions and particles that are attracted due to

electrostatic forces. Both these layers will create a capacitance (the *"double layer"* capacitance) on the surface of the metal and certain theories need to be considered when modeling this interaction with electrical elements. [76, 77]

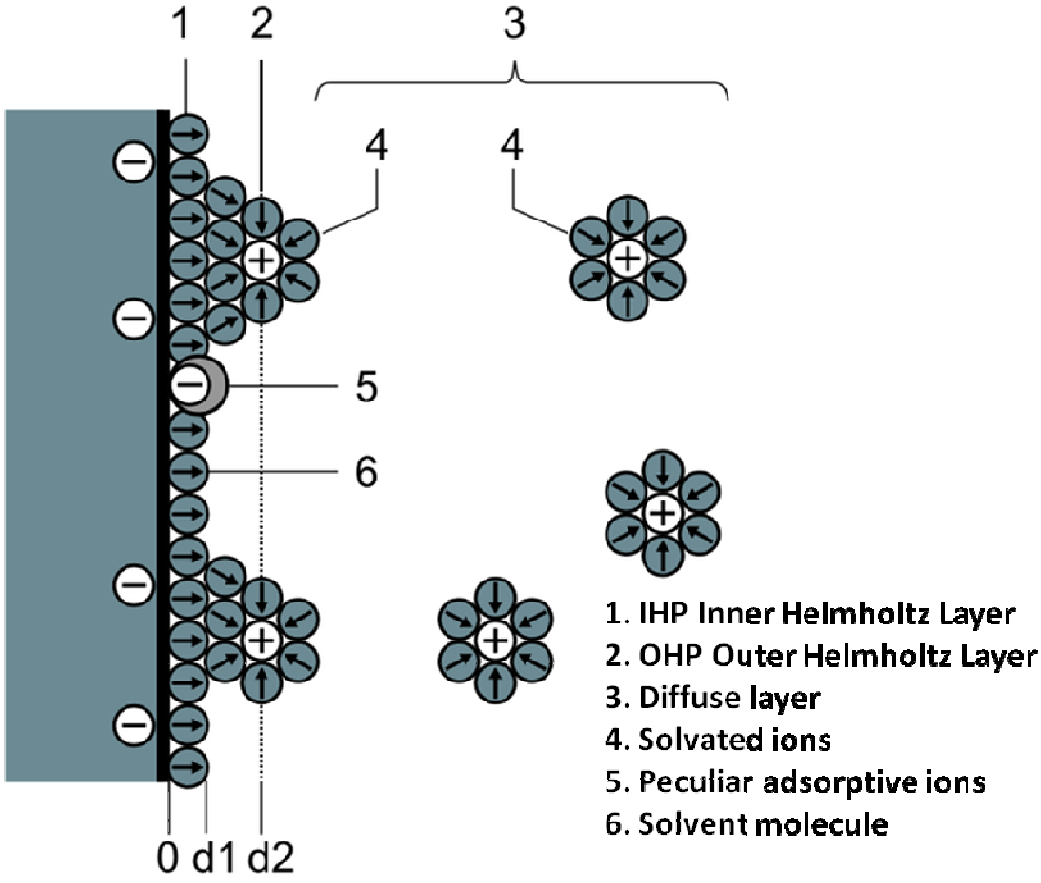

Figure 6: Scheme of the double layer on electrode (Gouy-Chapman-Stern model). Diagram taken from Wikipedia [78].

The Helmholtz model considers one side of the capacitor to be the charges at the metal surface and the other to be the ions at a minimum distance from the surface (0 to d1 in Figure 6) . This model assumes ions to be in a single plane and is only valid for high concentrations. When considering just the Helmholtz model, the capacitance is given by:

$$C_H = \frac{\varepsilon_0 \varepsilon_r}{d_{ohp}} \qquad \textbf{Eq. 1}$$

Where $\boldsymbol{d_{ohp}}$ (d1 in Figure 6) is the distance from electrode to the outer Helmholtz plane, ε_0 is the dielectric permittivity of space and ε_r is the relative permittivity of the electrolyte. For lower concentrations this model was inaccurate when experimental results were considered. The Gouy-Chapman model takes into consideration that along with coulombic forces, thermal motion also influences the distribution of ions [76]. The ions are not a single layer sitting on top of the electrode but have a varying concentration as we

move away from the interface towards the bulk solution forming a cloud of ions with a gradient of varying potential (layer 3 in Figure 6). This potential is described by:

$$V(x) = V_o e^{(-\frac{x}{L_D})} \quad \textbf{Eq. 2}$$

Here ***Vo*** is the potential at the electrode and ***x*** is the distance from the electrode towards the bulk. $\boldsymbol{L_D}$ is the Debye length (Figure 7) which characterizes the thickness of the diffuse layer and is given by:

$$L_D = \sqrt{\frac{\varepsilon_0 \varepsilon_r V_t}{2 c_0 z^2 q}} \quad \textbf{Eq. 3}$$

$\boldsymbol{V_t}$ is the thermal voltage (kT/q), $\boldsymbol{c_0}$ is the bulk concentration of ions (ions/dm^3), ***z*** is the charge on the ion, and ***q*** is the elementary charge. For a solution of concentrations such as 200-300 mM, this length can be approximately 10 Angstroms. The capacitance due to this theory is given by:

$$C_G = \frac{\varepsilon_0 \varepsilon_r}{L_D} \cosh\left(\frac{z V_0}{2 V_t}\right) \quad \textbf{Eq. 4}$$

The Stern model as shown in Figure 6, includes adsorption of the counter ions onto the surface (and not just the solvent molecules) [76]. This means we have a layer of adsorbed ions and a layer of ions beyond the distance that is dependent on the radius of the adsorbed ions. The model is thus essentially a combination of the Helmholtz, Gouy-Chapman and Stern models. The adsorption behaves in accordance to the Langmuir adsorption isotherm and is thus dependant on temperature and pressure. The Helmholtz layers (also called the internal Stern layer) can be divided into two parts, the inner Helmholtz layer that is due to specific adsorption of non hydrated ions (or neutral molecules) and the outer Helmholtz layer which is due to the hydrated ions. Water molecules may also adsorb to the surface, either themselves or as a hydration sphere of a counter ion (water molecules surround the ion due to the dipolar nature of water). The hydration layer is sometimes referred to as the hydration sheath and causes an increase in the activation energy for electron transfer which will hence influence the Faradaic impedance path. The total interfacial capacitance is thus the sum of the Helmholtz capacitance and the Gouy-Chapman capacitance:

$$\frac{1}{C_I} = \frac{1}{C_H} + \frac{1}{C_G} \quad \textbf{Eq. 5}$$

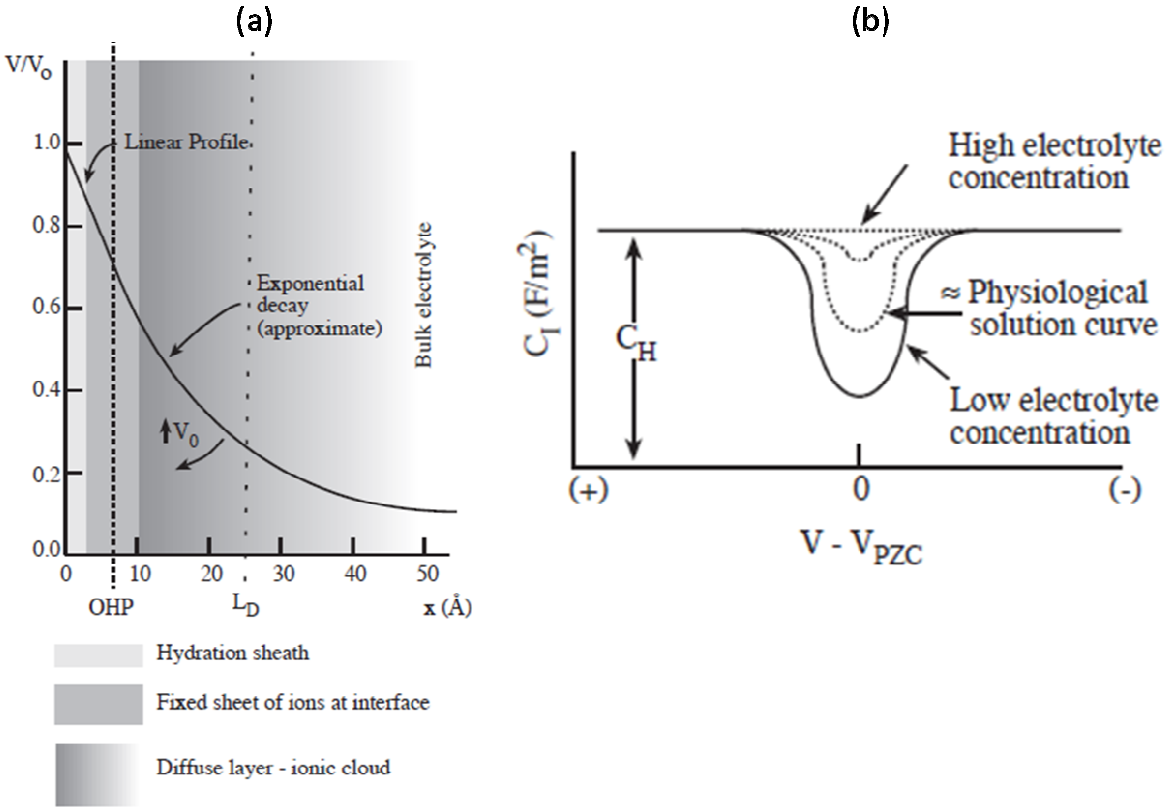

Figure 7: (a) Exponential decay of electric potential near the electrode against distance from the electrode (L_d). (b) Interfacial capacitance against electric potential varying with concentration of the electrolyte. V_{pzc} is the potential where charges are zero and C_H is the value for the Helmholtz capacitance which is dominant for high concentrations of electrolyte. Figures from Borkholder's thesis [79]).

L_D is dependant on the concentration of ions and the applied voltage. Increasing the potential causes the ions to move closer to the electrode causing C_G to increase and the interfacial capacitance is dominated by C_H. The affect of this on the value of C_I is shown in Figure 7 (b). Considering Figure 7 (b) and Table 2, we can see that increasing the concentration of ions in the electrolyte causes the interfacial capacitance to increase.

Molar Concentration (mMolar)	L_D (Å)
1000	3.0
100	9.6
10	30.4
1	96.2
0.1	304

Table 2: Values for L_D at 25℃ [76].

Neutral species can be adsorbed to the surface. They may partake in electron transfer however if they do not then they can block reaction sites. As the effective surface area of the electrode will also change, the double layer capacitance will also be reduced. [76, 77, 79-81]

2.2.2 *Charge Transfer Resistance*

There are Faradaic reactions and redox reactions taking place at the electrode interface. These reactions depend on Faraday's Law , that is the amount of electrons transfered are proportional to the amount of electricity passed). The electrodes are also called charge transfer electrodes due to this.

Charge transfer across the interface can also be limited by the need for external potential since some reactions will require extra energy for the charge to be transferred. The overall energy of the system and the required potential (and the polarity) for charge transfer depends on the reaction species, the electro-negativity, the equilibrium potential that is established across the interface, the concentrations of the redox species and non-Faradaic processes discussed earlier. At equilibrium the net current will be zero but if a DC voltage is applied, the electrode potential will deviate from its equilibrium value and a current will flow. The additional potential needed to drive the reaction at a certain rate is termed the *'over- potential'* $\boldsymbol{\eta}$ (difference between applied potential E and the equilibrium potential E_{eq}). This over potential is the sum of four potentials related to the processes discussed earlier:

$$\eta = \eta_t + \eta_d + \eta_r \qquad \textbf{Eq. 6}$$

Here $\boldsymbol{\eta_t}$ is the potential required for charge transfer, $\boldsymbol{\eta_d}$ is due to diffusion of reactant, $\boldsymbol{\eta_r}$ is potential required for chemical reactions to take place at the electrode and precedes charge transfer. In most cases η_t will dominate at low voltages and at higher voltages η_d will have a greater effect. For impedance spectroscopy the voltages are small and thus charge transfer potential is of most importance.

At equilibrium the net value of current across the interface will be zero. The absolute value of this current however is called the exchange current and is often measured as exchange current density $\boldsymbol{J_o}$. It is determined by measuring the charge transfer resistance around the equilibrium potential of the electrode. The Butler-Volmer equation states that for an applied potential the resulting current density is given by:

$$J = J_o \left[e^{\left(\frac{(1-\beta)\cdot z\cdot \eta_t}{V_t}\right)} - e^{\left(\frac{-\beta\cdot z\cdot \eta_t}{V_t}\right)} \right] \quad \textbf{Eq. 7}$$

Where $\boldsymbol{J}$ is the current density (usually in A/cm^2), $\boldsymbol{J_o}$ is the exchange current density, $\boldsymbol{\beta}$ is the symmetry factor (the energy barrier differences for the oxidation and reduction reactions) and $\boldsymbol{z}$ is the number of electrons transferred per molecule.[76, 79]

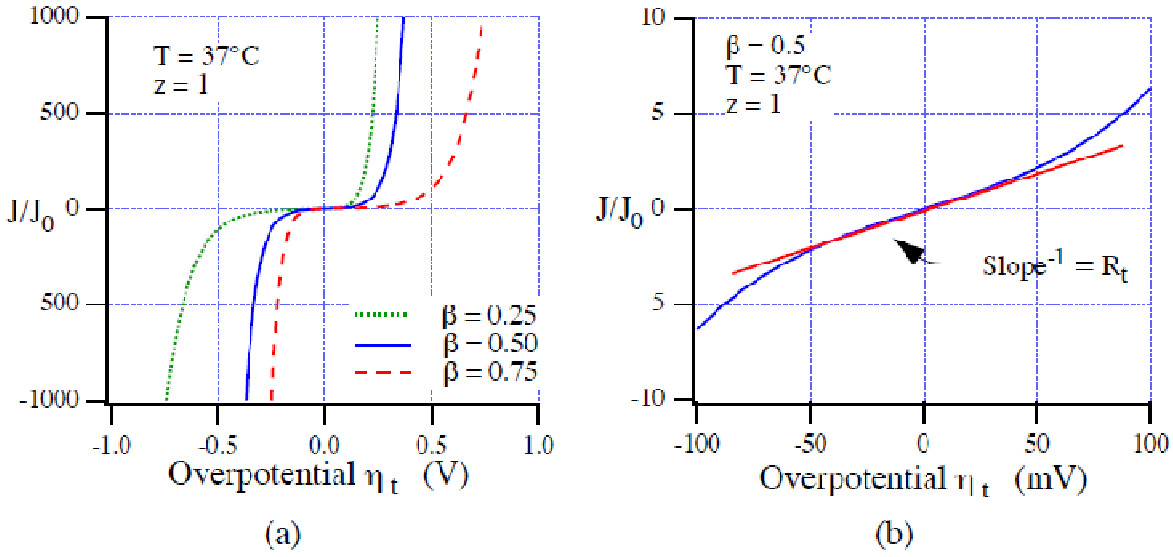

Figure 8: (a) Current density against overpotential. (b) Linear region for small signal analysis provides charge transfer resistance R_t. Figures from Borkhold's thesis [79].

By looking at the J and η_t relationship we can find a theoretical value for a resistance to represent this charge transfer. The exponential terms in the equation above show that the system behaves like two parallel ideal diodes in reverse directions. So it would be difficult to find a linear relationship. However if small signal analysis is applied, there is a linear region and the slope here can provide us with the *charge transfer resistance* $\boldsymbol{R_t}$. This can be proven mathematically using Eq. 7

$$for\ \beta = 0.5$$

$$J = J_o \left[e^{\left(\frac{0.5\cdot z\cdot \eta_t}{V_t}\right)} - e^{\left(\frac{-0.5\cdot z\cdot \eta_t}{V_t}\right)} \right]$$

From Taylor's Theorem we know that:

$$e^x = \sum_{n=1}^{\infty} \frac{x^n}{n!} = 1 + x + \frac{x^2}{2!} + \frac{x^3}{3!} + \frac{x^4}{4!} \cdots$$

$$thus\ if\ \alpha = \frac{0.5 \cdot z}{V_t}\ then$$

$$e^{\alpha\eta_t} = 1 + \alpha\eta_t + \frac{(\alpha\eta_t)^2}{2!} + \frac{(\alpha\eta_t)^3}{3!} + \frac{(\alpha\eta_t)^4}{4!}\cdots$$

$$e^{-\alpha\eta_t} = 1 - \alpha\eta_t + \frac{(\alpha\eta_t)^2}{2!} - \frac{(\alpha\eta_t)^3}{3!} + \frac{(\alpha\eta_t)^4}{4!}\cdots$$

$$Thus\ e^{\alpha\eta_t} - e^{-\alpha\eta_t} = 2\left(\alpha\eta_t + \frac{(\alpha\eta_t)^3}{3!} + \frac{(\alpha\eta_t)^5}{5!}\cdots\right)$$

However if we consider small signal analysis, $\eta_t \ll 1$ then the higher order terms become small enough that they can be ignored, thus:

$$J = J_o\left(\frac{z \cdot \eta_t}{V_t}\right)$$

$$We\ define\ charge\ transfer\ resistance\ as\ R_T = \frac{\eta_t}{J}\ hence$$

$$R_t(\Omega.cm^2) = \frac{V_t}{J_o \cdot z} \qquad \textbf{Eq. 8}$$

2.2.3 *Warburg Impedance*

In the charge transfer resistance section we considered mostly the effects due to kinetic processes (charge transfer) and ignored the issue of mass transport (ions will be moving in the solution and concentrations at the electrode varying). As a reaction is taking place at the electrode, the concentration of ions is changing. The products need to move away to the bulk and fresh ions need to move from the bulk to the interface. This creates a limit on the rate of reaction which is dependent on the rate of diffusion. As a sinusoidal potential is applied to the gradient of charged particles, they will move in response to the applied potential. It creates a sinusoidally varying concentration of ions. At higher frequencies the charges find it harder to follow the field. Warburg (1899) found that the concentration wave spreads out further at lower frequencies. He also found that the concentration and voltage at the electrode surface are 45° and -45° (respectively) out of phase from the current irrespective of the frequency (thus called a constant phase element). He defined a diffusion zone (*k*) as the distance from the electrode at which concentration is 1/e of the initial value.

$$k = \left(\frac{2D}{\omega}\right)^{\frac{1}{2}} \quad \textbf{Eq. 9}$$

Where D is the diffusion constant and ω is the frequency in radians/s. To measure this impedance with negligible phase distortion the length of the measurement cell (distance between both electrodes) should be several centimeters long. Finite length Warburg impedances will not have an exact 45° behavior which is usually the case for this research as the electrodes are spaced almost 2mm apart.

Warburg proposed a model for the impedance due to diffusion:

$$Z_w = \frac{A_w}{\sqrt{\omega}} - \frac{jA_w}{\sqrt{\omega}} \quad \textbf{Eq. 10}$$

Where A_w is the Warburg coefficient also represented as σ in texts and is calculated by:

$$A_w = \frac{RT}{z^2F^2A\sqrt{2}}\left(\frac{1}{D_o^{1/2}C_o^b} + \frac{1}{D_R^{1/2}C_R^b}\right) \quad \textbf{Eq. 11}$$

Where C_o^b and C_R^b are the bulk concentration of the oxidizing and reducing species, D_o and D_R are the diffusion coefficients of the two species, z is the number of electrons involved in the reaction, F is Faraday's constant, R the gas constant, T is the temperature and A is the area of the electrode. Derivations and details of the equations will not be discussed here and can be found in texts [76, 80, 81]. The Warburg impedance form shown above is only valid if the diffusion layer has an infinite thickness. In the case where is not infinite, the "Finite" Warburg impedance is given by:

$$Z_w = \left(\frac{A_w}{\sqrt{\omega}} - \frac{jA_w}{\sqrt{\omega}}\right)\tanh\left(\delta\sqrt{\left(\frac{j\omega}{D}\right)}\right) \quad \textbf{Eq. 12}$$

Where δ is the Nernst diffusion layer thickness. In the models and analysis later, I have used the assumption of an infinite diffusion layer thickness. This will keep the model less complicated yet sufficiently accurate for the analysis. [76, 79, 80]

2.2.4 *Spreading Resistance and Bulk Resistance*

As the dimensions of electrodes get smaller, geometrical effects need to be considered for the flow of current. The bulk resistance of an electrolyte solution is similar to that of a conductor, given by Eq. 13.

$$R = \frac{\rho L}{A} \qquad \textbf{Eq. 13}$$

Where ρ is the resistivity of the electrolyte, *A* is the cross sectional area and *L* is the length. Geometry of an electrode also plays an important role and small planar electrodes have a *"spreading resistance"*. This spreading resistance is caused due to constraints on the electric field not being able to spread in a hemispherical profile. For a circular electrode the spreading resistance would be found using [82].

$$R = \frac{\rho}{4r} \qquad \text{Eq. 14}$$

The reference electrodes in the devices used in my work are much larger than the measuring electrode (details in section 3.2). With such a large area, the impedance due to the electrode becomes negligible.

2.2.5 *Electrochemical and Impedance Analysis*

We have looked at the basic interface of an electrode from a physical and chemical point of view. The elements discussed up to now can be analyzed by different methods. The methods selected are based on the materials being measured and to what type of detail the overall chemical system needs to be understood. There are two methods that are relevant and will be discussed, "Cyclic Voltammetry" and "Electrochemical Impedance Spectroscopy" (EIS). Cyclic voltammetry is one of the most commonly used techniques to analyze electrochemical reactions. It provides an insight into the reaction/kinetic characteristics of a half cell. By understanding the energy required for a reaction and the rates we can determine the half cell redox reactions and by-products. Impedance spectroscopy will help us evaluate the physical elements in the form of an electrical circuit model. Doing so, we can understand the double layer and the Faradaic components of the system as well as the double layer. I will discuss both methods with impedance spectroscopy in further detail as it forms the basis of cell impedance spectroscopy and most of the results. Cyclic voltammetry results will also give some support to the impedance spectroscopy analysis for the material comparison.

The concept of impedance and its complex nature is important to understand CIS. Alternating current (AC) is current that is periodically changing its value. The *'signal'* wave is defined by a sinusoidal function. A sinusoid signal (current or voltage) has two important properties (Figure 9). The amplitude of the signal is the value

from the reference to the peak of the sinusoid. The phase is the relative angular position of the signal in comparison to a reference sinusoid. When an AC signal is passed through any material having an impedance, its amplitude and phase may change. These changes can be measured through impedance measurement instruments and used to calculate the impedance of that material or component. Thus impedance has two values as well, the absolute impedance (|Z|) that represents changes in the amplitude of the signal, and the phase (θ) that represents changes caused to the phase. These two polar values (absolute value and phase) can also be represented as the real (*a* or *Z'*) or imaginary (*b* or *Z''*) part of the impedance when represented as a complex value. [83]

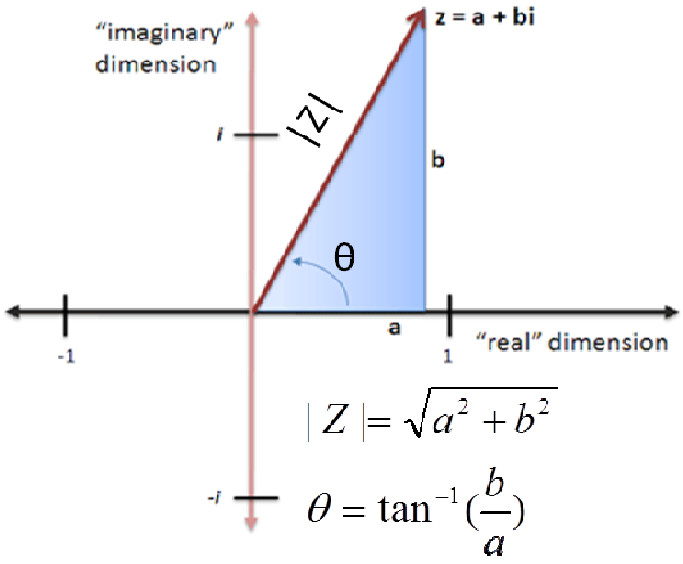

Figure 9: Complex and Polar representations are related mathematically as shown [84].

Impedance spectroscopy works by measuring changes to such a signal due to the impedance of the half cell. By measuring at various frequencies we can get an impedance spectrum. These measurements can then be analyzed by fitting to an equivalent electrical circuit model. Data from an impedance spectrum can be shown as either a Bode or a Nyquist plot. A Bode plot shows the absolute impedance (|Z|) and the phase (θ) against frequency on the x-axis. It can also be used to show the real impedance (Z') and the imaginary impedance (Z'') against frequency. Nyquist plots show that the results with Z' on the x-axis and Z'' on the y-axis of the plot. Both have their merits and will be used. An example of the two plots of a 1nF capacitor in parallel to a 10kOhm resistor is shown in Figure 10 and will be useful when understanding the different results.

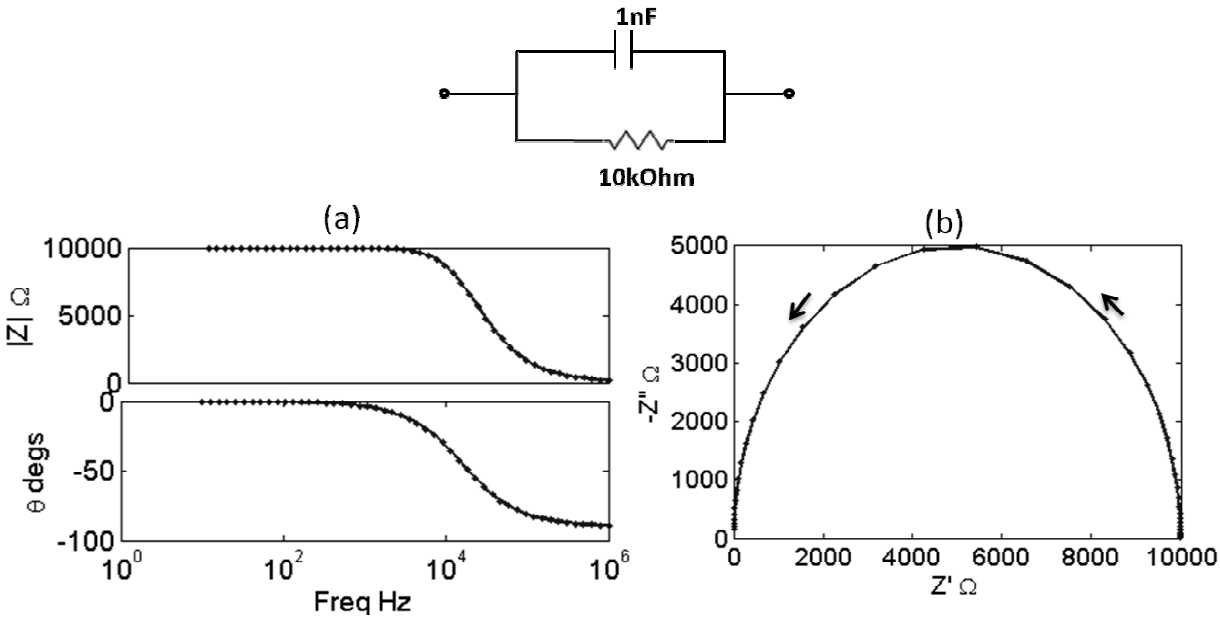

Figure 10: Impedance plots of a circuit with 1nF capacitor parallel to 10kOhms resistor. Bode plot (a) and Nyquist plot (b). The arrows on the Nyquist plot show increasing frequency.

2.2.6 *Randle's Cell Model*

Randle's model [54, 81] is one of the most common impedance models used for electrochemical cells. The model includes a solution resistance, the electrode spreading resistance, and the electrodes own Ohmic resistance which is significant in the case of PEDOT electrodes, all summed up as a series resistance called R_s. When dealing with microelectrodes, we also need to add the spreading resistance. Thus R_s, now termed as the 'total series resistance' is in series with a parallel double layer capacitance C_d and a charge transfer resistance R_t (also called polarization resistance in some texts). This circuit is considered a simplified Randle's circuit, shown in Figure 11 with the impedance equation given by:

$$Z = R_s + \frac{1}{\frac{1}{R_t} + \omega C_d} \qquad \textbf{Eq. 15}$$

The Bode plots and the Nyquist plots for a simplified Randle's circuit are shown in Figure 12. The Nyquist plot is a semicircle similar to that shown in Figure 10 but with a shift to the right on the x-axis due to the added series resistance which at higher frequencies is the only element contributing to the total impedance. This is because at higher frequencies the impedance of the capacitor will be extremely small, and R_t will be

bypassed. Thus the intersect (with the x-axis) of the semi circle provides us with the values of R_t and R_s as shown in Figure 12. The graphs also show how increasing values of the C_d changes the resonant frequencies as the minimum phase peaks are shifting. Increasing the R_t increases the maximum values of the impedance. Another thing to notice is that the phase falls and then rises again for a parallel RC circuit with a series resistance added but did not without it. Also this peak in the curve shifts with varying component values.

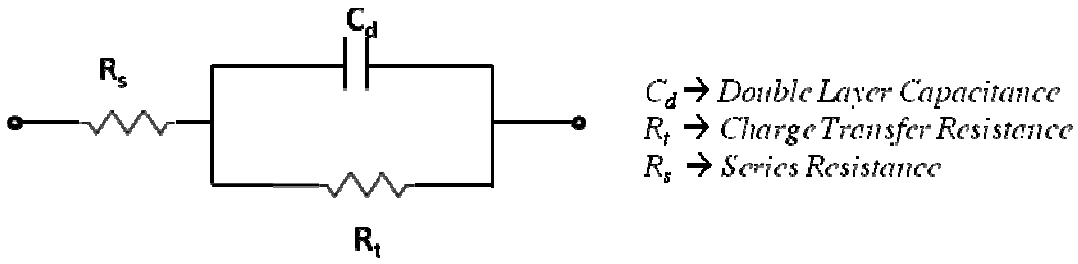

Figure 11: Simplified version of Randel's circuit.

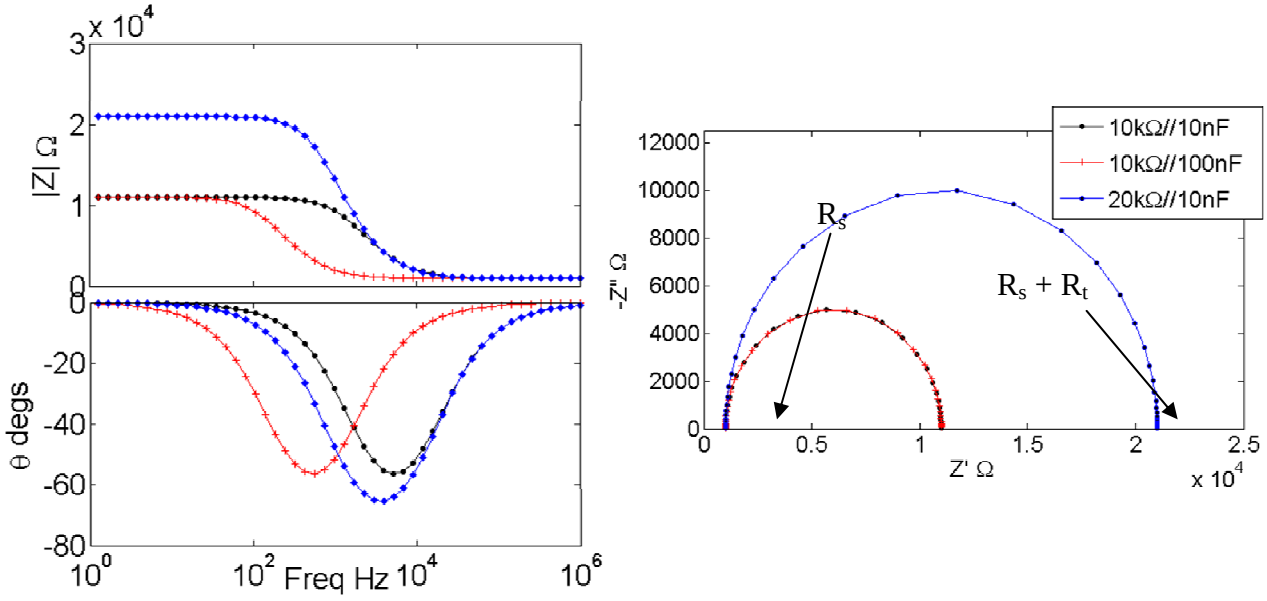

Figure 12: Bode and Nyquist plot for simplified Randle's circuit from 1 Hz-1 MHz. R_t and C_d values are shown in the legend as R_t // C_d. R_s is 1 kΩ in all cases.

Now let's consider the effects due to diffusion, the Warburg impedance. Figure 14 shows the impedance plots of a Randle's circuit with Warburg impedance (Eq. 16). The Faradaic path is dominant at lower frequencies, and the straight line shows that at lower frequencies the Warburg impedance dominates as shown by the 45° line that is the tail of the curve.

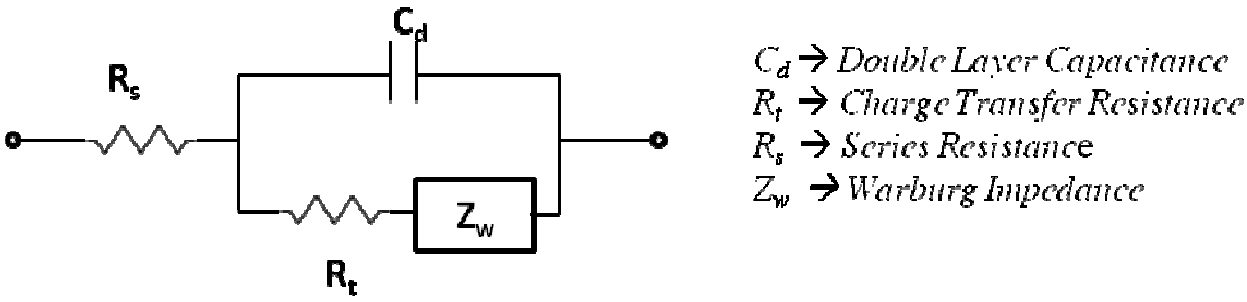

Figure 13: Randle's circuit with Warburg impedance [83].

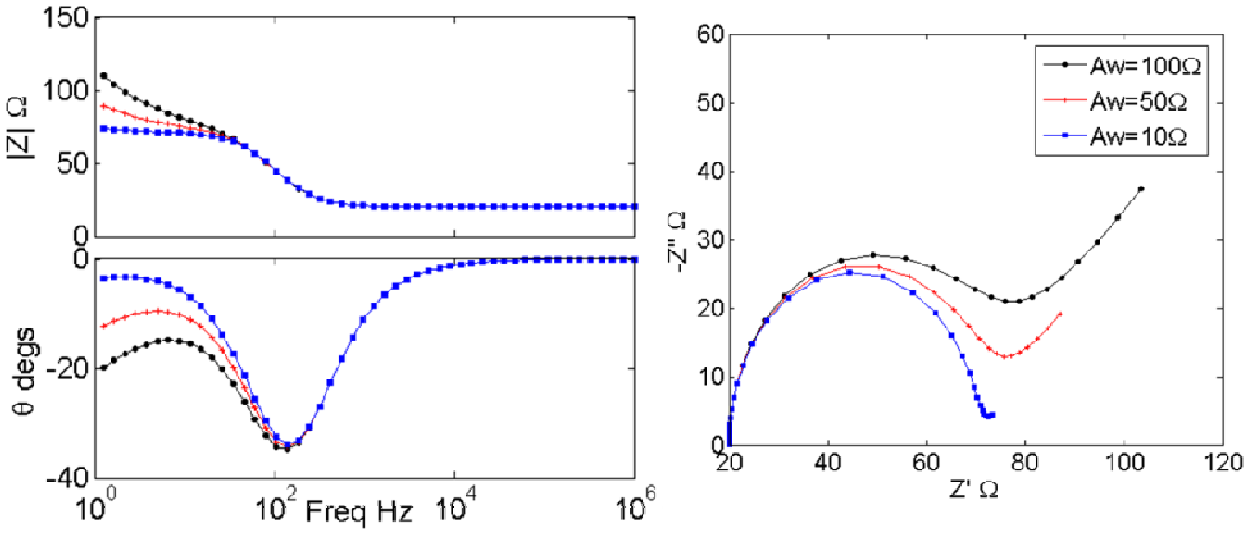

Figure 14: Bode and Nyquist plots of Randle's circuit from 1 Hz-1 MHz. R_t is 50 Ω, C_{dl} 40 µF, R_s is 20 Ω and the Warburg coefficient A_w is 100 Ω(black), 50 Ω(red) and 10 Ω(blue).

$$Z = R_s + \frac{1}{\frac{1}{R_t + \frac{A_w}{\sqrt{\omega}} - \frac{jA_w}{\sqrt{\omega}}} + \omega C_d} \qquad \text{Eq. 16}$$

Figure 15 shows how changing values of the Faradaic impedance components affects the impedance of the circuit. As the Warburg impedance becomes more dominant, the Nyquist plot straightens out more. In the bode plots of both Figure 14 and Figure 15, we can see that for a large Warburg and charge transfer resistance, the lower frequencies will change shape and increase in their impedance values. The plots also show that there is vital information in the frequencies below 100 Hz and even 20 Hz. The frequency spectrum shown in these plots is slightly wider (down to 1 Hz) than what was achievable with the instruments available to me (minimum 20 Hz). However the curve fitting techniques used in section 5.2 can be accurate enough for our analysis, especially given the vast differences between the two types of materials that will be discussed. We do not necessarily need to cover the frequencies where we can see the tail of the Warburg

impedance. Though it would provide more accurate results if the frequencies down to 1 Hz were covered as the lower end of spectrum contains more information. This would lead to the curve fitting having to fit with more data points with values that are dominated by the Warburg impedance.

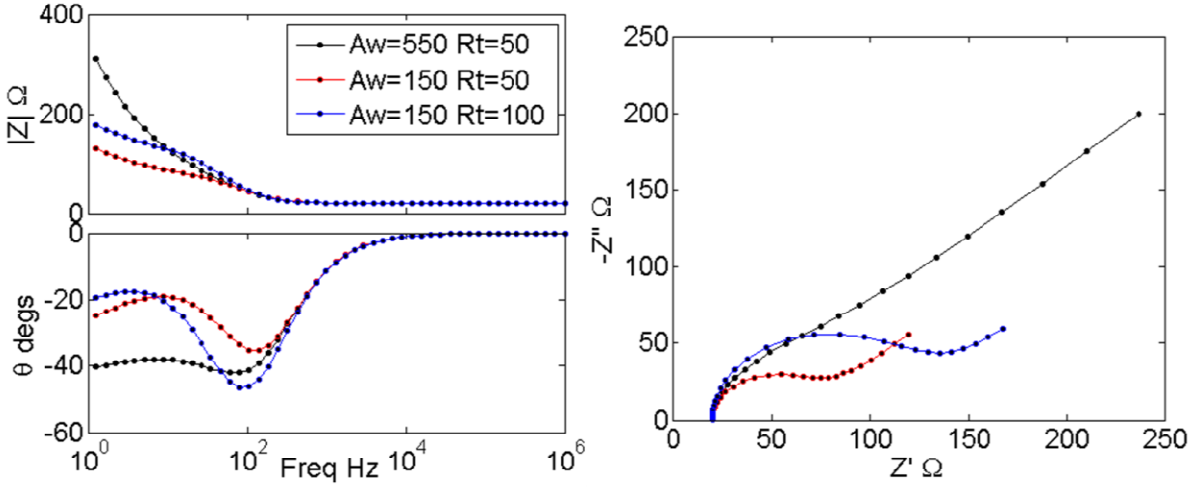

Figure 15: Bode and Nyquist plots from 1 Hz to 1 MHz while varying values of R_t and A_w. All values in the legend are in Ohms.

The characteristics in the plots will help justify the selection of the models that we consider for the electrochemical impedance analysis of the electrode materials, in HEPES saline.

2.2.7 *Constant Phase Element*

While it is useful to use electrical analogies and ideal electrical elements to model and analyze electrochemical junctions, we must realize that they may not always imitate the actual physics with perfect accuracy. One issue often found in electrochemical modeling is that the elements are frequency dependant. Capacitors in EIS show a particular kind of frequency dependence where the measured phase is independent of the frequency but not necessarily having a phase value of -90° like in ideal capacitors. These elements are called constant phase elements (CPE). The impedance of a CPE is given by:

$$Z_{cpe} = \frac{1}{(j\omega)^n Y_0} \qquad \textbf{Eq. 17}$$

The constant *n* is an empirical constant that accounts for the non-ideal behavior of the element. It has a value between 1 and 0. When *n* is 1 the equation represents an ideal capacitor. Y_0 is the capacitance of the element. Constant phase element behavior is a consequence of various surface conditions: surface roughness; non-uniform current

distribution; or multiple reaction rates at the surface. The double layer capacitance in Randle's circuit can be replaced by a CPE to provide a better model [76, 85-87].

2.3 **Cell Impedance Sensing**

Cell – substrate interactions are an important part of research in cell biology. Currently most assays utilize force (laminar flow etc) to separate cells which have or have not adhered to the substrate. They can then be counted which requires either manual counting, microscopy with image analysis software or colorimetric assays. The impedance measurement of cells cultured on a substrate was an idea that started in the 1990's by I. Giaever and C. Keese [2]. The technique was subsequently named by them as Electric Cell-substrate Impedance Sensing, or ECIS for short. It relies on the fundamentals of electric current flow in solutions and dielectrics. When a potential is applied between two electrodes, the value of the current will depend on the resistance of the path it crosses. In the case of an alternating current the resistance would be replaced by impedance, that is having a real (resistive) and an imaginary (reactive) component. As cells grow on top of this electrode the impedance of the path will change. Figure 16 shows how the current would have two paths. Higher frequencies will face lower impedance from the cell membrane and will mostly pass through the cell. Lower frequencies would pass from around the cell and through the cell – cell junctions as these will be the lowest impedance paths at those frequencies. This means that depending on the frequency, we can determine what the changes mean for the cell culture. We should be able to determine the behavior of cells, their adhesion to the substrate, and their cell – cell interactions [3, 4, 88-91]. Currently Coulter counter methods are available that use electrical means to detect the number of cells [92]. However they require the cells to flow through an aperture where they are detected and thus cause massive disturbance in the environment of the culture. This also makes it impossible to detect the cells while they are on the surface and spread out over the surface. By using the ECIS we can quantify the cell growth, its behavioral changes to drugs as well as detect cell motility.

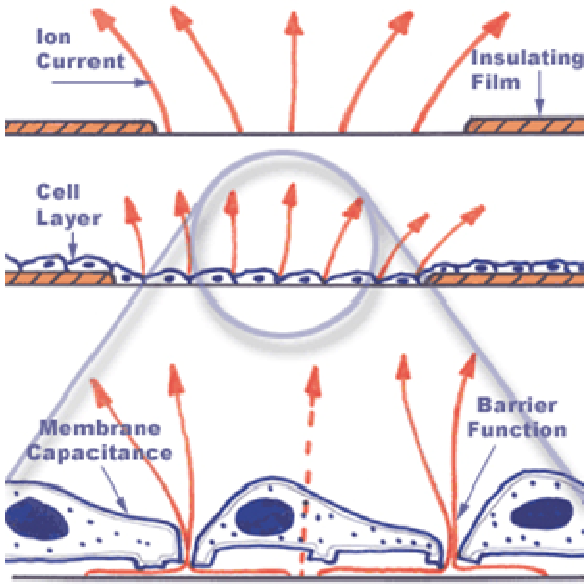

Figure 16: ECIS theory, how the growth of cells hinders the current path. Diagram from Applied Biophysics [93].

ECIS has also been adapted into research for drug testing and understanding of cell behavior. Products based on ECIS are already available and being used for drug testing. Altough the results are not always conclusive, they have however provided excellent quantitative data that reflects the cell growth or behavior to go alongside with other test methods. Recently the method has been advanced further in by varying the frequency of the signal over a certain range and taking measurements. Now considered as an Electrical Impedance Spectroscopy (EIS) it has provided further insight into the electrical equivalent circuit of the entire cell electrode system. Due to its non invasive methodology, it has been used to characterize growth of mesenchymal stem cells without the use of external markers [94]. Bouafsoun *et al* characterized adhesion onto different protein and gold electrodes using EIS [95]. Yiling Qui *et al* have used it to monitor cardiomyocyte adhesion and used the results to characterize and derive a circuit model of the system [10]. Lo *et al* have analyzed fibroblasts and done work to understand the impedance model of cells with a more elongated shape [96]. Another interesting piece of work is from Xiaoqiu *et al* is to develop FEM (finite element method) simulations of impedance changes due to cells on electrodes [97]. They have looked at simulations and results of impedance changes on electrodes partially covered with cells. Their modified equivalent model is more accurate for partially covered electrodes, but they did not find the phase part of the impedance very useful. Results in the later parts of this thesis are contradictory to this assumption. The current path can flow in various ways when a cell is on top of the electrode. It can travel through the cell layers (trans-cellular) or around the cell membrane (Para-cellular). The overall impedance would depend on these two paths, the cell-substrate distance, electrodes

and any coating on it (e.g. proteins) and the medium for the culture growth. The frequency and the type of path taken by the current will affect both the absolute and phase parts of the measurements.

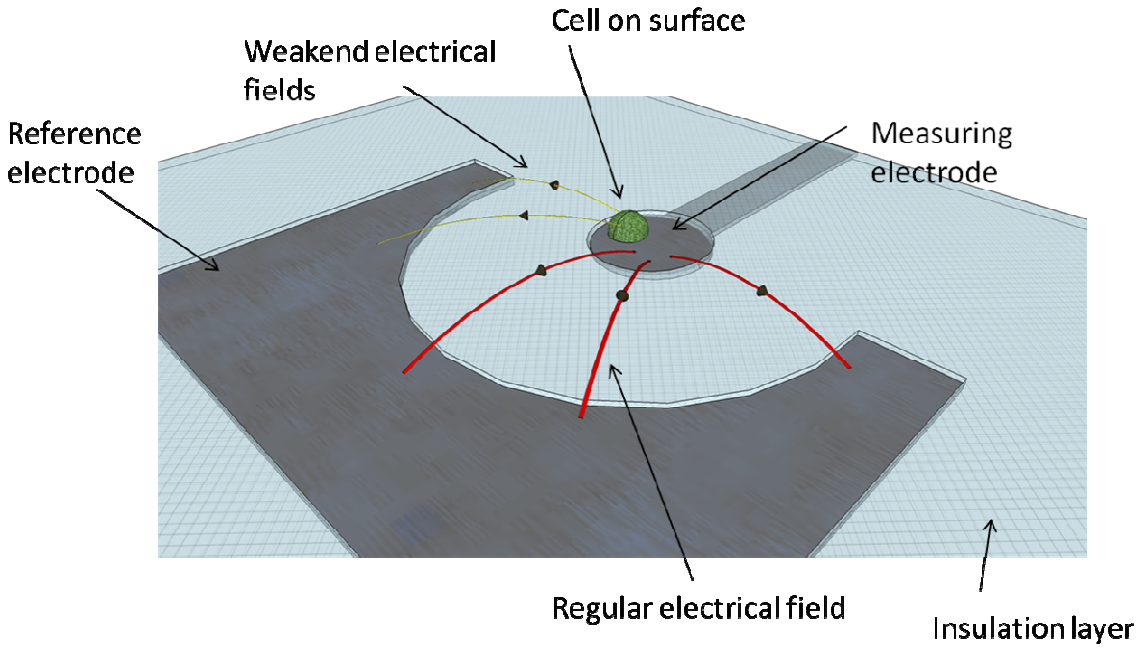

Figure 17: 3D sketch of a cell on the surface of an electrode and the effects due to it to the electric fields. The electrode design here is one used in my experiments described later.

While terms like ECIS and EIS are usually used for commercial products and electrochemical methods, I will use Cell Impedance Spectroscopy (CIS) throughout this thesis for clarity.

2.4 Relevant Cell Biology Background

2.4.1 *Eukaryotic Cells*

The animal eukaryotic cell is one of the most basic building block of a biological mammal. It consists of an outer plasma membrane that acts as the cell boundary which contains the cytosol, organelles, the nucleus, the cytoskeleton as well as proteins and molecules. The cytosol, or intercellular fluid, is a solution filled with many different forms of molecules and fills most of the volume of the cell. The nucleus of the cell is where the DNA is stored and is the control center for the cell. The organelles are little sub-units inside the cell that perform specific functions such as generating, transporting, sorting and storing proteins, along with many others such as generating ATP, the energy source for all

functions in a cell. The cytoskeleton is a set of three types of protein filaments that provide structural integrity to the cell as well as transport pathways.

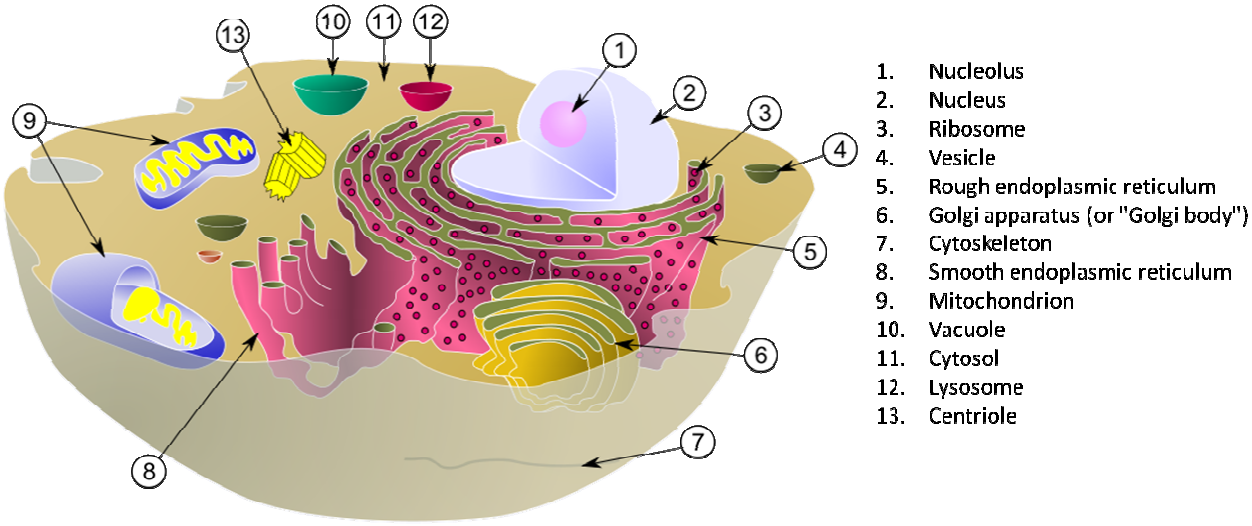

Figure 18: The eukaryotic cell. Image from [98]

Animal cells are very complex and a human body alone has over 230 different kinds of cells. They can be separated and grown in *cell cultures*. Detailed descriptions and in-depth discussion of cells is beyond the scope of this work but I will describe some of the important aspects of cells essential to cell impedance spectroscopy. These are the overall cell structure that is being measured through AC impedance measurements and the behavior that affects the measurements as well. [99]

2.4.2 *Plasma Membrane and Lipid Bilayer*

A cell is a composition of various organelles, nucleus, proteins and many chemical compounds all wrapped up inside a bubble like membrane. This outer shell is called the plasma membrane. The membrane is composed of different organic components, most important of which are the phospholipids that create the lipid bilayer. The phospholipids are long fatty chains (amphiphatic molecules)with a charged head group making one end water soluable and the other hydrophobic. Through self assembly, they create a bilayer where the hydrophilic ends are set outwards and the hydrophobic ends come together. This creates a membrane where by a wall is created with water regions on both sides. The plasma membrane also includes unique complex protein structures that act as gateways for chemical interactions (signaling) and transport of chemical substances when required. The membrane is also semi-permeable to certain gases and small molecules. This allows a

unique set up where the cell can exchange certain molecules and still keep its intercellular functionality separated from the outside. [99]

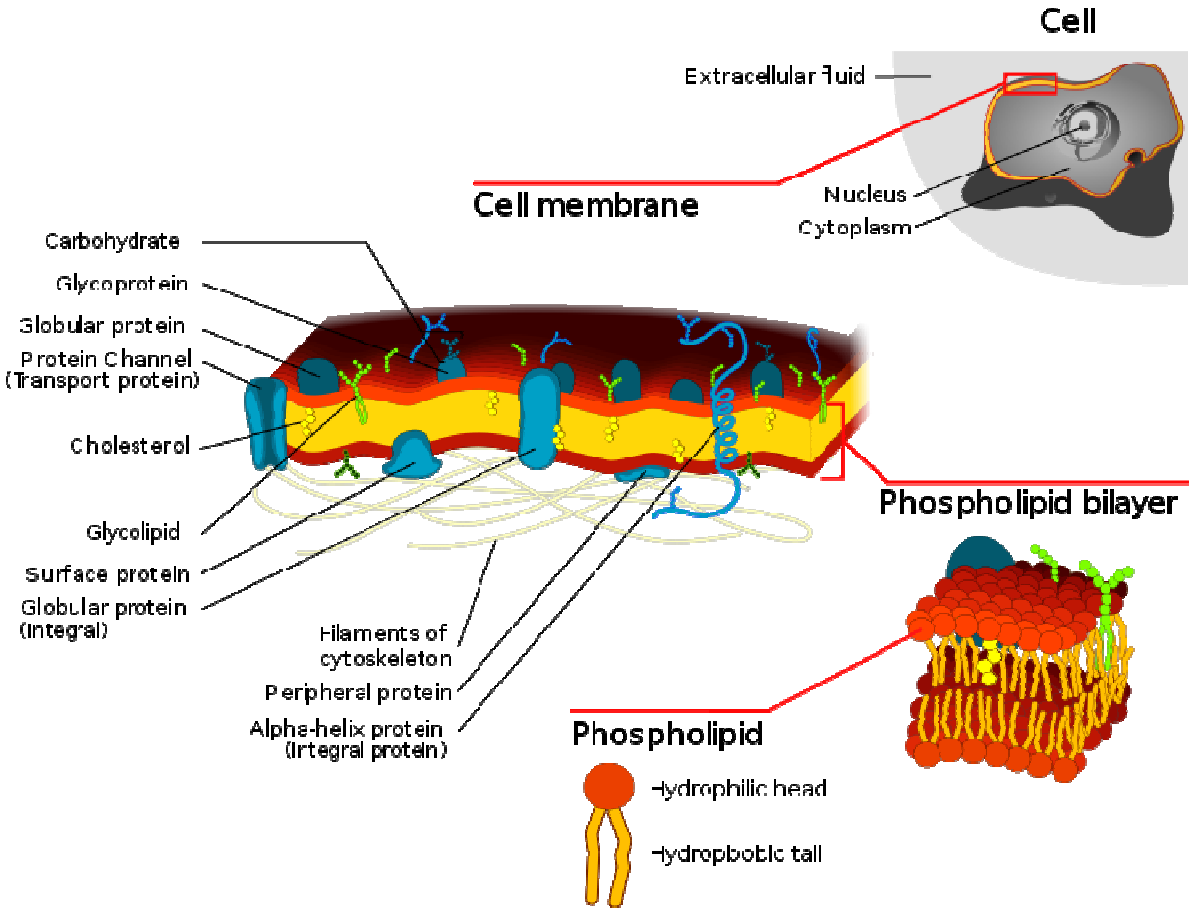

Figure 19: Plasma Membrane. Image from [100]

2.4.3 *Cytoskeleton*

The cytoskeleton is an intricate network of protein filaments that extends throughout the cytoplasm and gives the cell a structural integrity. The cytoskeleton is highly dynamic and is also responsible for transport pathways inside the cell as well as the movement of the cell itself. It is built on the framework of three types of protein filaments: the intermediate filaments; the microtubules; and the actin filaments. The intermediate filaments are composed of a large family of proteins. They are a rope like structure and are the most durable of the three types of filaments. Their main function is to provide tensile strength to the cell.

The microtubules provide organization in a cell. They are stiff hollow tubes that begin from a single location called the *centrosome* and extend out towards the cell periphery. They are built by tubulin molecules and can rapidly disassemble at one point and assemble at another. They allow organelles to anchor to them and are the tracks along which organelles, vesicles and other cell components can move.

Actin filaments are responsible for cell motility. They are formed by subunits of actin and are usually unstable but can form stable structures in cells when required. They perform different functions by working with different actin binding proteins. They can influence the shape of a cell and interact with myosin to perform a muscle like function for a cell. They also create a contractile ring that helps separate the cytoplasm during cell division. [99]

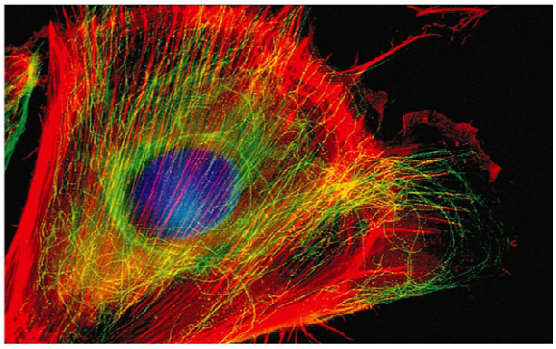

Figure 20: Fluroscent staining of the cytoskeleton of a cell. Actin is shown in red, the nucleus is shown in blue and the intermediate filaments in green. [101]

2.4.4 *Cell Cycle*

Eucryotic cells reproduce by replicating DNA and then performing cell division. They have a complete cell cycle which determines the timeline for what the cell must do and when it must do so. There are four phases in their cell cycle as shown in Figure 21. 1) M phase, where the splits and creates daughter cells. 2) S phase, where the cell replicates its DNA. 3) G_1 phase, which occurs between the M phase and S phase, where the cell grows and prepares itself (accumulates required molecules and materials) for DNA synthesis. 4) Finally the G_2 phase which occurs after the S phase. A cell measures its state and controls when to begin each phase by cyclically activating and inactivating key proteins and protein complexes that regulate DNA replication, mitosis, and cytokinesis. Each type of cell has a time approximation for their cell cycles to complete and multi cellular organisms must insure that this organization and timeline is strictly regulated else abnormalities can occur .

In the G1 phase, or the first gap phase, is where the cell manufactures all the necessary proteins which are required for DNA replication. This is the longest phase (10-12 hours from a 24 hour cell cycle). Once it is ready, the DNA replication takes place in the S phase. Then another gap phase, G2, takes place during which the synthesis of all the material required for the actual cell division takes place. Finally M phase occurs where the

cell nucleus divides (*mitosis*) and the cell splits in two (*cytokinesis*) daughter cells. In *mitosis* the cell must perform pairing, alignment and separation of duplicated chromosomes. In *cytokinesis* the cell performs the physical procedure of splitting into two new cells. At times cells may also go into a G0 phase where they enter a quiescent state and wait for a signal to re-enter their cell cycle. This can often be the case once confluence in a cell culture is achieved. [99, 102]

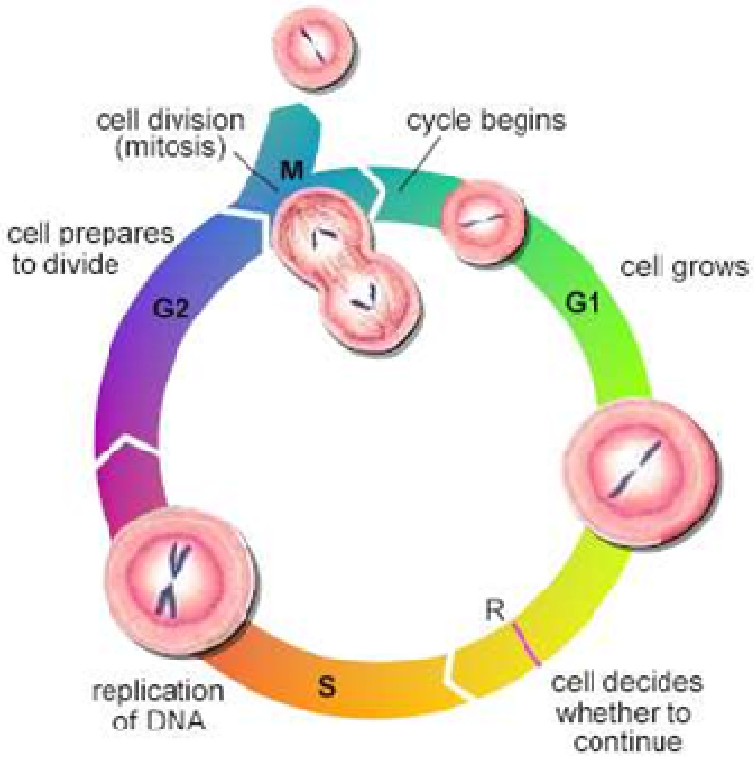

Figure 21: The Cell cycle. Phases G1 and G2 are the growth phase in between phase M (mitoses) and Phase S (DNA replication). The daughter cells then start the cycle once again. [103]

2.4.5 *Cell Adhesion*

The extra cellular matrix (ECM) is a collection of various proteins and carbohydrates which surround the cellular membrane in a cell culture. They are present in any culture media which is supplemented with serum. The ECM is essential for connections to form between cells and for cells to adhere to the substrate. Cells also generate ECM compounds themselves. The ECM must itself attach to the substrate surface and by controlling how the ECM attaches to the surface, we can control the behavior of cells on the surface. Fibronectin is an important plasma glycoprotein (a component of ECM) for cell adhesion

and is quite often used to coat the surface before cells are seeded. It is made by hepatocytes and fibroblasts and consists of two disulfide linked polypeptide chains which posses several structural domains which can react with cells and the ECM (example heparin and collogen). It binds itself to the surface and allows the cells to attach themselves to it. The regions where cells adhere are called *focal contacts* or *adhesion plaques.* Cells themselves detach and attach to the disulfide linked polypeptide sequence of fibronectin through transmembrane proteins called *integrins*. The integrins themselves are connected to the cell actin filament through a chain of other proteins and anchor the cells cytoskeleton to the surface.

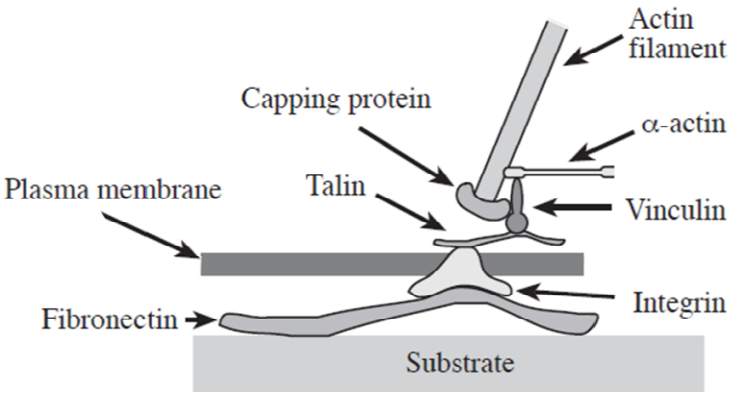

Figure 22: A schematic of the mechanism of cell adhesion to a substrate. Special proteins take part in the mechanism to help the integrin proteins to help anchor the cell to the fibronectin which is adsorbed to the substrate. From thesis by D. A. Borkholder [79].

Cells use the fibronectin and ECM components to anchor themselves to the surface and move over it. In order for a cell to move, three interrelated processes must occur and all three involve actin. The cell must 1) create a protrusion towards the front, 2) adhere to the surface at the front, 3) and drag the rest of the cell forward by traction. For the first process, the actin filaments grow in the direction of the movement, stretching the membrane forward. Once the membrane reaches a favorable patch of surface, a protein present in the plasma membrane, integrin, will help the cell stick to it. The integrin attaches internally to the actin filaments and after anchoring the cell, contractions take place at the back end of the cell. Thus the force helps release the adhesion at the back and pulls the entire cell forward. [79, 99, 102, 104].

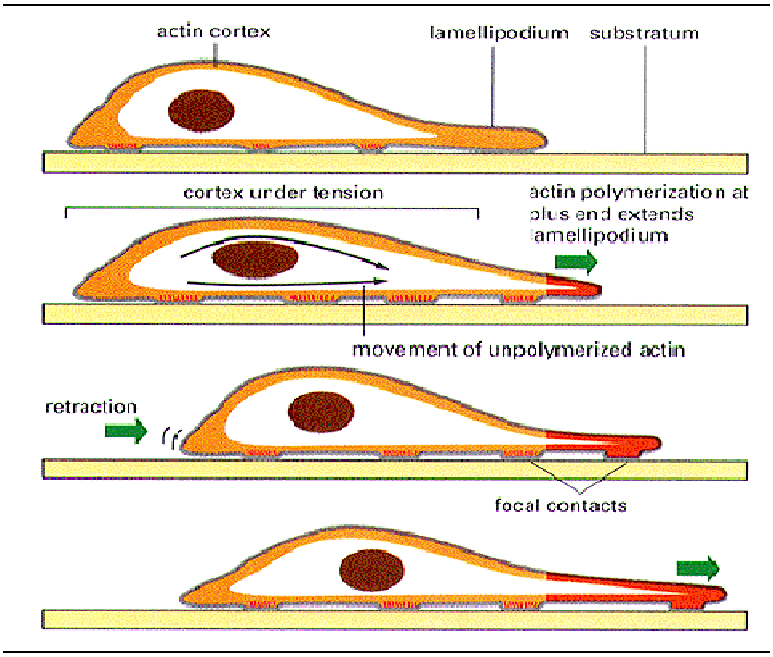

Figure 23: Cells use focal contacts to pull themselves forward. The actin filaments can rearrange themselves to roll the front end of the cell. When the cell creates a new focal contact, the actin filaments at the backend will be reorganized allowing the cell to release itself at the back and continue moving forward. Figure by Gwen Childs [105]

2.4.6 *Cell – Cell Junctions*

Many cells create tissues that perform specific functions inside the body. Once cells come closer and interact with each other (especially confluent cultures), they form junctions. These junctions can be of different types, classified according to their function. The *"Tight"* junction seals neighboring cells together to prevent passage of water soluble molecules easily. They are formed from proteins called *claudins* and *occludins*. *"Adheren"* junctions join actin bundles of neighboring cells to create mechanical attachments. *"Desmosome"* junctions join the intermediate filaments and both, adheren and desmosome junctions are built using proteins called *cadherins*. *"Hemidesmosome"* junctions anchor the filaments to the basal lamina (or fibronectin) using integrin proteins. Finally the "*Gap"* junctions are small passageways that allow molecules and ions to pass between cells. They are created by protein complexes called *connexons* (which are present in the membrane) protruding into the membrane of another cell and vice versa. In the case of endothelial cells, before they reach confluence, they have a shape similar to that of fibroblasts. They proliferate and show motility as well. Once cells contact each other and form junctions, they behave differently. Their cytoskeleton will change its shape and the cells move into a rest state where they stop growing and reproducing. They also stop responding to growth factors. This is essential as they can move to recover from wounds and then maintain their

layer once confluence is reached so that there is no breach in systems such as vessels [99, 106].

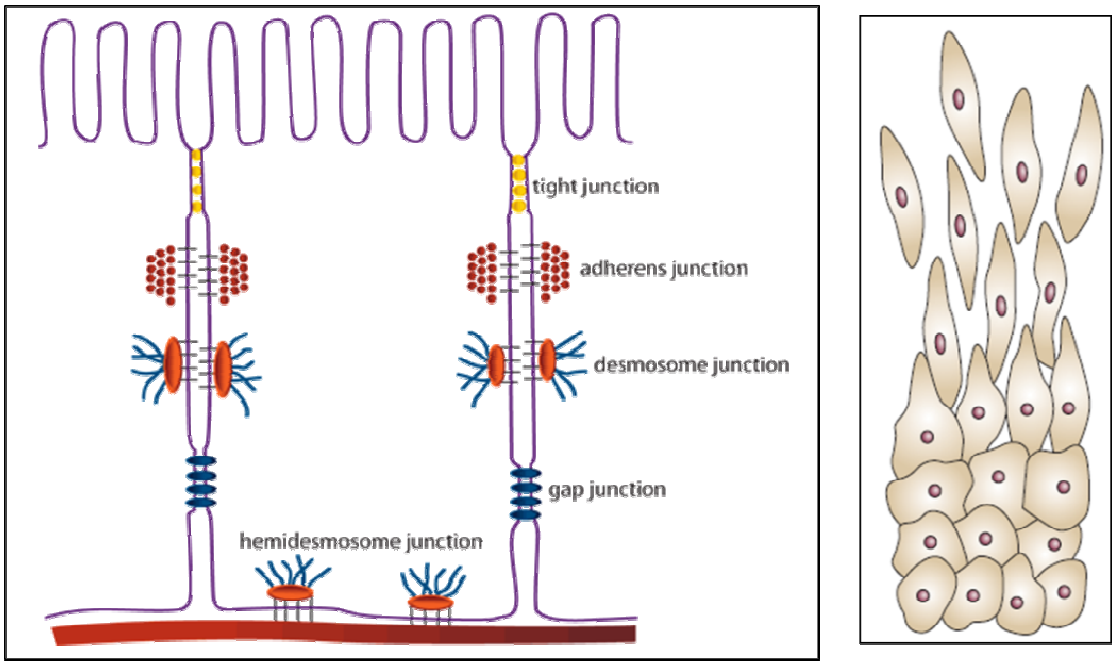

Figure 24: (Left) Cell - Cell junctions. Taken from "Essential Cell Biology" by B. Alberts [99]. (Right) Confluent cell layer (bottom) and sparse cell layer (top), taken from "Endothelial cell-cell junction" by E.Dejana [106].

2.4.7 *Embryonic Stem Cells*

Stem cells have the ability to differentiate into specialized cell types. They are important for replenishing adult tissues as well as the post fertilization development of an embryo. There are two types of stem cells, embryonic and adult stem cells. Embryonic stem cells are isolated from the inner cell mass of blastocysts and adult stem cells harvested /extracted from adult bodies. [55, 99]

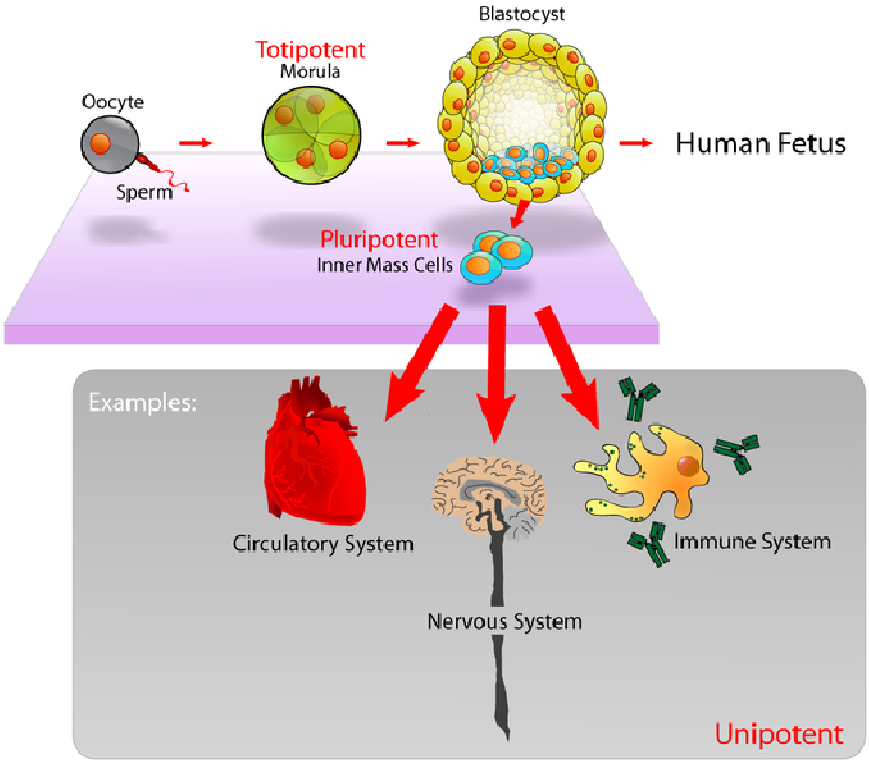

Figure 25: Stem cells differentiate into other cells that create the organs and the rest of the cells in the body. Diagram by M. Jones from Wikipedia [107].

Stem cells have the ability to self renew indefinitely unlike most common cells that have a limit to how many times they can divide before they reach the Hayflick limit [108-111]. Cell cultures of regular cells usually degrade after a certain number of passages. In the event that there is a need to generate a large number of cells, this property of stem cells can be really useful. For instance if there was a need to generate a litre of blood, we would require over a trillion cells. It would not be possible to do so by culturing blood cells alone. The ability of Stem cells to differentiate into blood cells without degradation would help in such large quantities of cell generation.

Chapter 3: **Materials and Methods**

When I started on this project in the beginning of 2010, I had no understanding of the complications involving interfacial capacitance, impedance measurement technology or cell biology. Initially I went on to create my own instrument using a National Instruments Data Acquisition Module, the PCI-6221. This worked well however lacked the accuracy and the bandwidth required. The connection method also limited the accuracy further (2-port connection). My initial devices were also created using inkjet printing which proved difficult to work with. After almost eight months I turned to using an Agilent Impedance Analyzer (A-4294) and a better designed device fabricated using standard photolithography steps. In time, the setup was improved with an automated LabView measurement program and a QuadTech 1920 LCR meter was used for a secondary setup as described under “Instrumentation” later.

3.1 **Materials**

Commercially available poly (3,4 ethylenedioxythiophene) poly(styrenesulfonate) (Orgacon S305 plus,AGFA) was used which is a 0.54% by weight aqueous solution of PEDOT:PSS. The S305 plus includes binders to help adhesion to substrates and stabilizers for improved environmental stability. SU8-3005 (Microchem, Newton, MA, USA) and Microposit S-1818 (Shipley, Coventry, UK) photo resists were used for fabrication. EC solvent (Ethyl Lactate, Microposit, Shipley, Coventry, UK) was used to develop SU-8, and MicroDev (Microposit, Shipley, Coventry, UK) was used for S-1818 development after a 1:1 dilution with RO water. The glass substrates used were 50mm x 75mm microscope slides (Corning, Amsterdam, The Netherlands). Acetone, methanol and iso-propanol (Sigma Aldrich, Dorset, UK) were used for cleaning the substrates and devices at various steps. Wells were created using µ-slide 8-well culture dishes (Ibidi, Munich, Germany).

3.2 **Device Design and Fabrication**

There were basically three phases of the development of the devices. The first device design was one inspired by Giaever's original works [112]. The original design was simply two or more lines of a metal / conducting material coming from their respective contact points inside a chamber capable of holding fluid. These were insulated with wax and exposed at the ends to create electrodes and contact points respectively. One electrode had large dimensions and this was the reference electrode. These were good for initial testing of the theory and for my own cell culture learning. They were also fabricated using inkjet printing which provided a fabrication method with flexibility in design changes and used material where required, reducing waste. However the fabrication output was rather inconsistent (Figure 28) and became terribly inconvenient not only to fabricate but also to analyze the results. The insulation layer was hand painted PMMA and the connections were carefully soldered wires to silver conducting paint on the PEDOT:PSS electrodes. This initial version was not good enough and a more evolved device was then developed based on lithographic techniques and with a proper electrical contact and cable design. My aim with the device fabrication was that they should be simple, should use all the materials that are commonly available and that those materials should be relatively cheap. So the second type of device used glass slides as substrates and the well size was made so that simple cut outs of Eppendorf 1.5 ml containers could be used as the wells. It used 5μm of SU-8 as the insulation layer and the electrode shape and sizes were designed by looking at products available from "Applied Biophysics". It had three wells (Figure 27) so that three experiments could be measured in parallel. The discussion of the instrumentation for this setup and its evolution is done under its own heading. The connector patterns were initially sized and placed so that the device could easily slot into PC connectors. However later I found it more convenient to use a customized connector with soldered pins which provided more reliability in the connections. The design of that connector was done according to the patterns already set for the PC connectors.

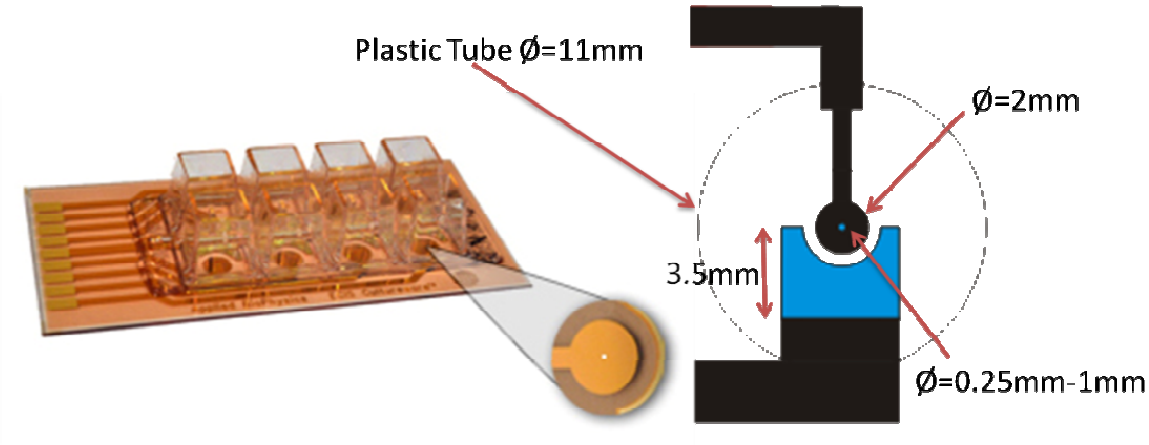

Figure 26: A culture dish available from Applied Biophysics. The device design was based around the design of these devices as shown in the schematic on the right. The blue parts are the exposed electrode surface and the black parts are the insulated ones. [93]

The third device was initiated due to the realization that three parallel experiments were not enough and biological cell experiments required measurement of more wells and cultures under similar conditions. Most of my time with the earlier version was wasted with constant failures in a single well due to cell deaths, measurement failures, or random issues such as loss in media volume due to evaporation etc. Another failure in the second device was that the Eppendorf tubes were hand cut and did not have proper covering that allowed easy handling and reliability. The mechanical design was flawed and time constantly wasted in device fabrication and restarting the experiments. So I designed a device with eight wells and used culture dishes that were acquired from Ibidi. The number of wells was limited by the dish design available and that the size of each well was roughly 1 cm x 1 cm . These culture dishes/wells were ideal to be applied on substrates which were microscope slides of dimensions that were easy to handle and easily available (50mm x75mm glass slides). The overall mechanical design was not flimsy like the three well design and all the electrodes had the same lengths which provided more similarity in the results. The Ibidi culture dishes also had properly designed covers that worked very well as would be expected.

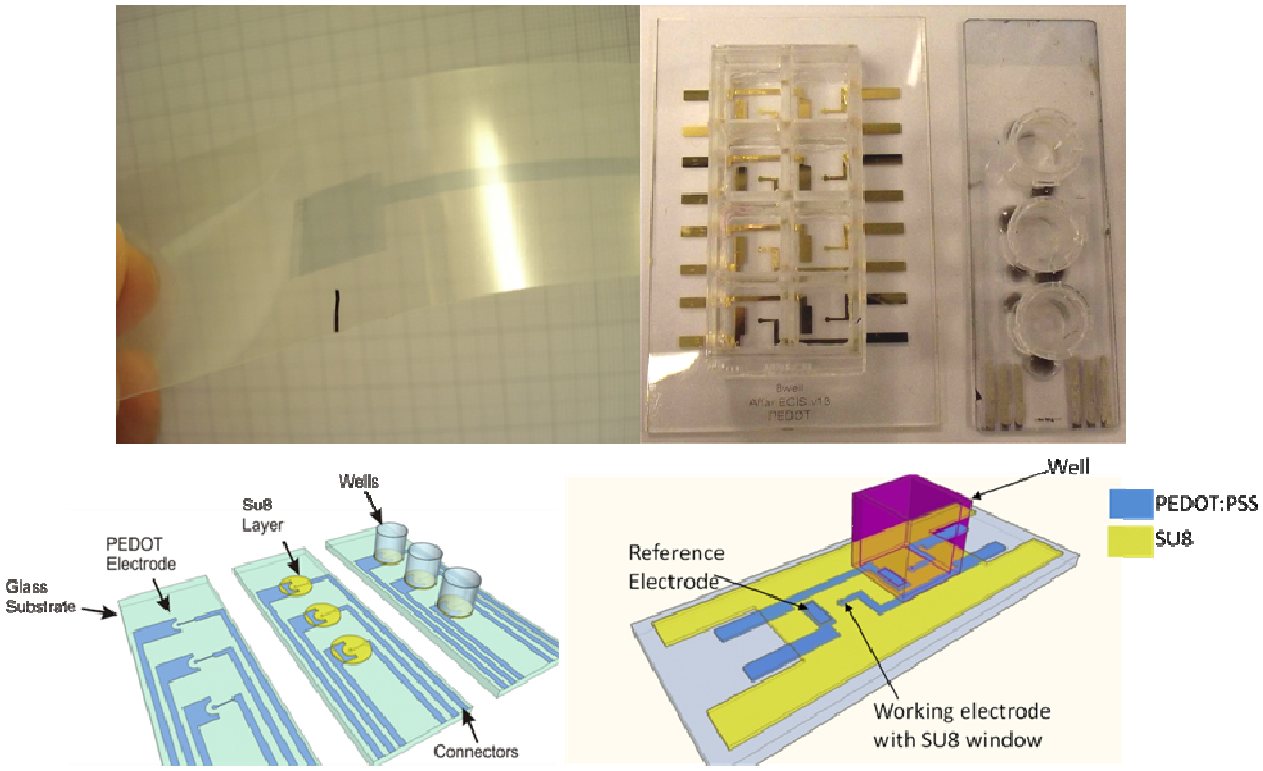

Figure 27: (Top left) Inkjet printed PEDOT:PSS on a plain transparency. (Top Right) Pictures of the 2nd and 3rd generation devices. (Bottom) Schematic diagrams of the two devices with only one row of the 3rd generation device shown.

The design and sizes of the electrodes were pretty much constant for the various device designs (apart from the first one which just had exposed front ends for electrodes). When considering the electrodes, the working electrode should be much smaller than its respective reference electrode. By doing so, changes on the reference electrode (due to cell growth etc) will be minimized in comparison to the measuring electrode. The impedance of the reference electrode will also be minimized due to its large area. For the second design, based on an assumption that the average cell diameter is 20 µm, I felt that a 250 µm diameter would be a good estimate for the measuring electrode for initial testing as this would give enough space for approximately 150 cells. For the reference electrode, I choose the geometry of a 3x5 mm rectangle. The reference electrode was designed in a shape similar to devices available from “Applied BioPhysics”, encompassing the microelectrode and being much larger than the measuring electrode ensures that it has minimal impact on the impedance measurements as the area covered by a single cell is much smaller. By the third design I started using 500 µm diameter measuring electrodes as I felt them more appropriate for cell coverage and provided better results. After getting good results and impedance values that were in acceptable ranges (not too low and not too high based on the measurement capabilities of the instruments) I decided to stay with these values. During

the course of my work, I also explored using inter digitated electrodes but these covered such a large area over the device that the sensitivity to changes in the cell culture was reduced and it was not possible to analyze the culture through microscopy at all the locations in a suitable manner. I deemed it simpler to be able to look closely at a single point (the center) of the culture and relate them to changes in the measurements.

Patterning PEDOT:PSS reliably, at resolutions below 20 μm , is difficult using the chemical oxidation process described in section 3.2.3. Therefore I have used a larger PEDOT:PSS microelectrode pattern (2mm diameter) and then created a 250 μm window in the insulation layer instead. This way the microelectrode area is far more accurate. The device needed to have more than one well as this would allow me to have a control well, and more experiments running at the same time under the same conditions. Given the space of the slide and the requirements, I set the total number of wells to three. Later this was increased to eight wells. Figure 29 and Figure 30 shows the final device design.

3.2.1 *Evolution of the Device Fabrication*

The device fabrication is fundamentally based on exploiting the solution processing capability of conducting polymers (especially PEDOT:PSS). PEDOT:PSS can be patterned by many methods. These include inkjet printing, gravure printing and lithographic procedures. Gravure printing is good for mass producing and requires proper stamps, not something easily done in our lab and it is difficult to create new designs quickly with this process. Inkjet printing is good for quick design implementations and prototyping but lacks reliability unless one can control the drops much better than I was able to. The technique is very sensitive to the surface energy (wetting) which may not necessarily remain constant over the entire duration of the printing. Humidity of the surrounding can also affect the results and can be difficult to control unless the printer is modified to do so. The final inkjet printed pattern is also bound to have a rough surface and non-vertical edges. This can make the dimensions of the electrodes and patterns unreliable. Figure 28 shows some good and bad printed patterns using a Dimatix DMP-2800 inkjet printer from Fujifilm (USA).

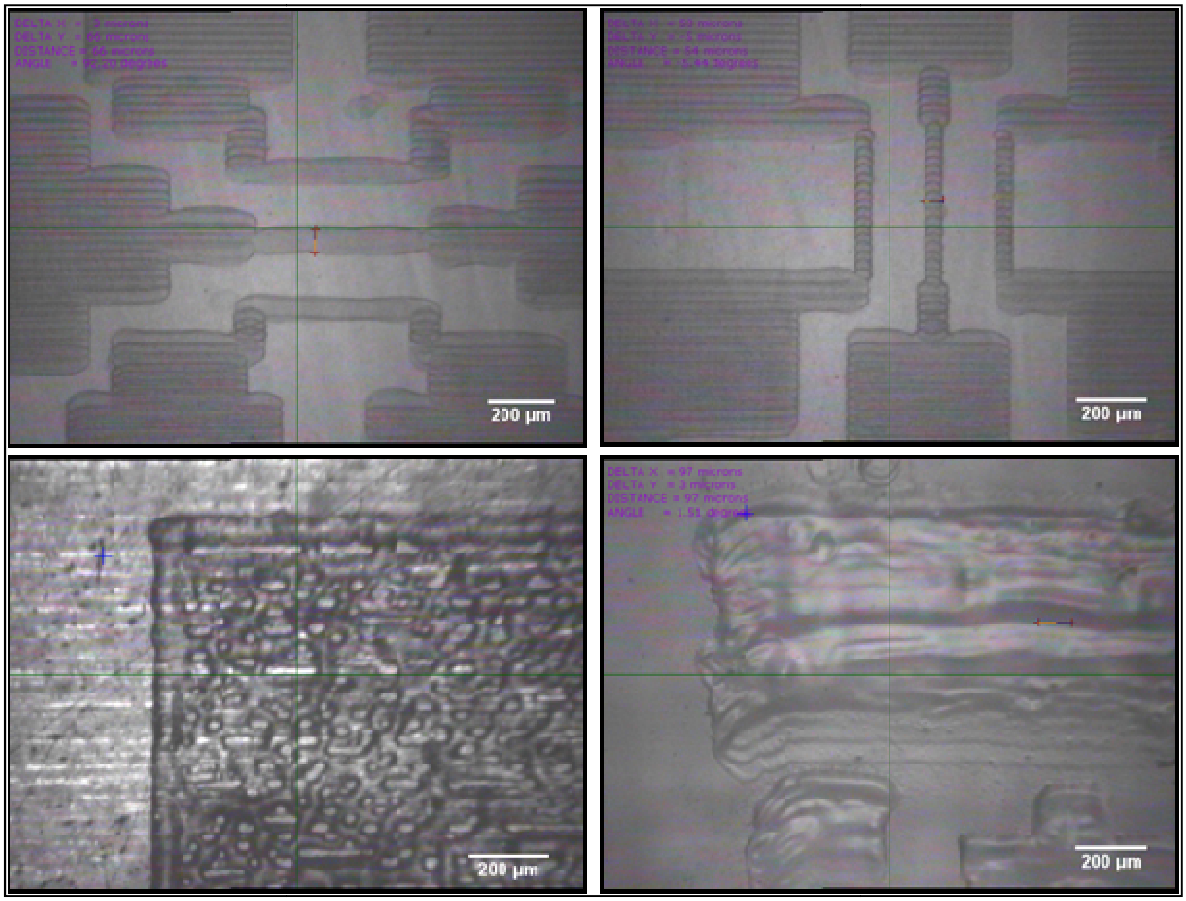

Figure 28:(Top) Inkjet printed patterns of the minimum possible resolution with the praticular cartridge type that was used. Lower resolutions should be possible but it is much harder to achieve. Note how there are vertical line patterns. This is because the printer prints in a raster format from left to right. Vertically adjacent drops do not join together as the time duration between them is long enough for the first drop to dry out before the second line is reached. (Bottom) Pictures of prints gone wrong. The white scale bars are marked as 200 microns.

Liquid flow (and hence the spot covered by a drop,) is highly dependant on the surface tension of the ink and the surface energy of the surface. If the surface tension of a liquid is higher than the surface energy of the surface than the drop will not spread out onto the surface to form a film. Furthermore the liquid will move to the adjacent spot where a new drop is falls (or vice versa), to create larger spots leaving gaps and creating inconsistency in the pattern. As the surface energy is increased, the drop begins to spread out more but will have poor adhesion once dry. A much higher surface energy would allow the drop to spread but then this spreading means the dimensions of the wetted region by the drop increases, limiting the resolution of the print. One way of controlling these factors is to alter the properties of the ink by adding surfactants, however in the case of the Orgacon ink used, it already has such additives. Heating the surface can also help create smaller spots (with the same drop) but then a dried up portion will not flow to join new drops

causing the formation of a rough inhomogeneous surface. Getting the ink formulation correct, along with printing process and parameters is not trivial and often a trial and error method is used to find them. The biggest problem I faced was that these parameters would vary from day to day (most possible due to atmospheric conditions). Keeping the substrate surface characteristics consistent was difficult as well since the effects of a oxygen plasma clean (to increase the contact angle) can wear down within a few hours if not minutes. [113-115]. I thought of various other methods in which I could control the shape of drops on the surface of the substrate. One of these ideas was to use surface micro patterns but due to time constraints I was not able to pursue it. Inkjet printed patterns suffered from poor adhesion in cell culture media and the cost of the inkjet cartridges which were difficult to be reused since the pores would clog quite often, made it prohibitive. It just did not seem reliable nor feasible as the fabrication method for this project. I felt that inkjet printing and improving my process would be too time consuming and was a project on its own right. I thus opted to use photolithography. Photolithography was an excellent choice given the facilities available and the insulation used in the final step fit well into this scheme as I was able to use SU8 photo resist. It is a material already used quite often with biology. Its thickness and resistive properties fit well with the criteria and it is highly transparent. It can also be hardened and made chemically un-reactive after development by heating at 180ºC. Photolithography masks for our features can also be produced relatively cheaply by using plastic (acetate) laser printed sheets temporarily stuck on a quartz slide. This is a good alternative (given that feature sizes are larger than 10 µm) to the chrome and ferric masks used traditionally but which are far more expensive and time consuming to produce. It also encouraged me to explore various designs without worrying about cost or perfecting my designs before I had masks made.

The scheme of the device fabrication is listed below and is followed by a detail description of each step:

1. Substrate cleaning and alignment layer
2. PEDOT:PSS layer and patterning
3. SU8 insulation layer and patterning
4. Attaching wells and preparing connections

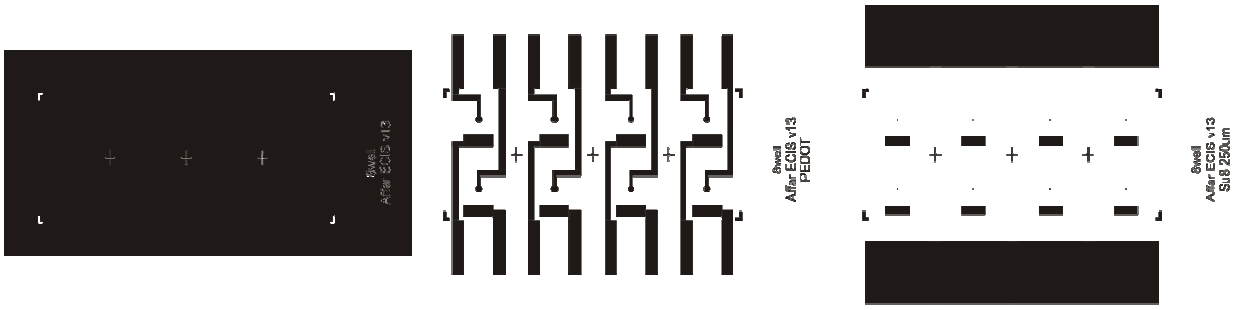

Figure 29: Mask patterns used for photolithography. (left) for the Alignment layer, (middle) for the PEDOT:PSS layer, (right) for the SU-8 layer.

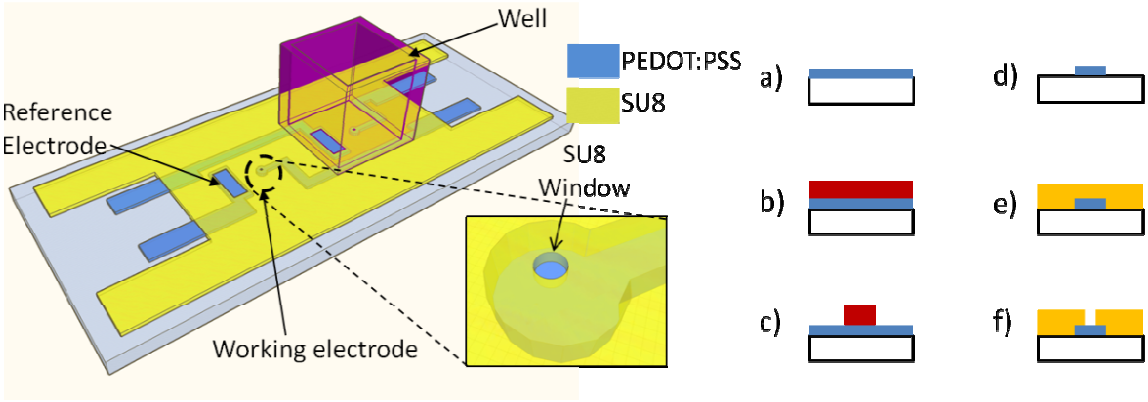

Figure 30: Diagram showing a single row of the device (left) with the insert showing the SU-8 window that defines the working electrode geometry. The fabrication steps are shown on the right, a)PEDOT:PSS is spin coated onto the surface, b) S1818 photoresist (red) is spin coated onto the surface, c) the photoresist is exposed and developed, d) the exposed PEDOT:PSS is oxidized using bleach and the photoresist removed using acetone, e) SU-8 (yellow) photoresisit is spin coated onto the patterned polymer and substrate, f) the photoresist is exposed and developed to give windows that create the electrodes and contacts for the device.

3.2.2 *Substrate Cleaning and Alignment Layer*

The glass slide is rinsed (ultrasonic bath) in acetone, methanol, and iso-propanol for 3 min each. S1818 photo resist is spun at 3000 RPM for 30 s and dried for 2 min at 90ºC on a hot plate. Exposure of the pattern is performed using an MA6 mask aligner for 10 s and a power density of 7.1 mW/cm^2. Note that the exposure duration for glass substrates will be higher than for silicon substrates since the reflections from the substrate are reduced. Development is done in a developer solution (1:1 RO water to microposit developer) for 70 s, rinsed in RO water and dried. The alignment layer is a 30 nm layer of Al (aluminum) patterned as shown in Figure 29, and it is done by evaporating Al in Plassys

II and followed with a liftoff procedure (15 min in acetone in a 50ºC hot bath and then an ultrasonic bath for 5 min).

3.2.3 *PEDOT:PSS Layer and Patterning*

The glass slide with an aligment layer is again rinsed in acetone and IPA, then it is cleaned in an oxygen plasma asher for 3 min at 180 W. Orgacon S305 is spin coated at 1000 RPM for 30 s and then baked on a 95 ºC hot plate for 1 min. This is then repeated one more time as each layer is approximately 50-60 nm thick and it is important to have above 100 nm thickness of PEDOT:PSS. This provides reliability of the device's electrical connections and a more appropriate conductivity for our work. Thinner layers often have high series resistance in the measurements and have breaks in the patterns causing frequent device failure, however additional layers do not always adhere well to previously deposited PEDOT:PSS layers and peel off during experiments as shown in Figure 31 . The device is then baked for an extra 5 min on a 95 °C hotplate and another 5 min in a 120 ºC oven. It is important to bake the device on a 95 ºC hotplate to dry the wet layers before placing in an oven since otherwise small craters form in the layer as shown in Figure 32 (a), using differential interference microscopy (Normaski microscopy) on a Leica INM20 microscope. This is most probably since in an oven the top part of the spin coated layer gets dried first with vapors being released by the lower part of it at the same time. This leads to holes being generated and deformations as those vapors try to escape.

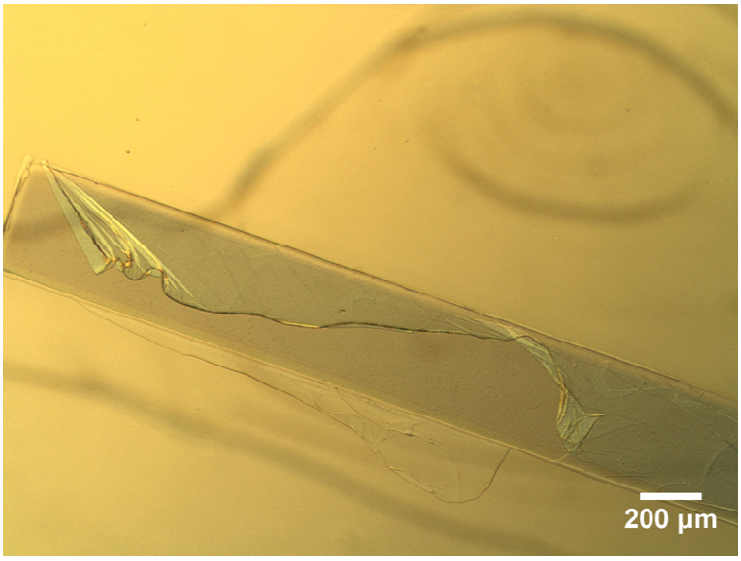

Figure 31: PEDOT:PSS second layer peeling off of the first.

Immediately after the PEDOT:PSS layer is dried off, it is spin coated with an S1818 layer and baked on a 95ºC hot plate for 2-5 min. It is then patterned by

photolithography similar to that done in the alignment layer for the S1818 patterning. When creating PEDOT:PSS patterns of less than 50 µm I found that the S1818 patterns would lose adhesion and break off during this development process. I tried using some primer to help with the adhesion but to no avail. There is also a slight color change from grayish blue to a slight brown shade of the PEDOT:PSS that is exposed when S1818 is being developed. I had looked at the variations in conductivity of PEDOT:PSS (and thus any sign of oxidation) when exposed to the microposit developer but it did not cause any problems. This leads me to believe that the byproducts of the development process causes oxidation of the PEDOT:PSS layer which possibly in turn leads to adhesion loss. However I was not able to explore the problem due to time constraints, especially given I could escape the problem by using larger dimensions for the PEDOT:PSS pattern.

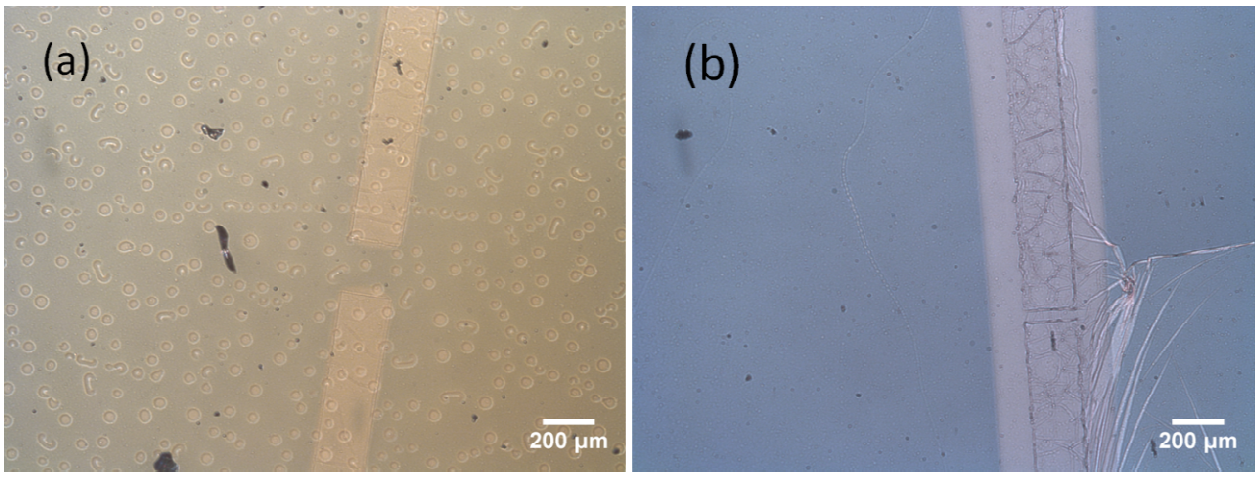

Figure 32: Pictures taken during fabrication (Normasky micrscopy). (a) Shows a well defined line and (b) shows an overexposed pattern. The first figure also shows the crevices that form when baked in an oven at high temperatures.

After development, the device is placed in a 1.6% bleach solution (20 mL NaClO 10% with 100 ml RO water) for 6 s and immediately rinsed under an RO water tap[116]. This step will etch the exposed PEDOT:PSS by first oxidizing it and then physically stripping the weakened layer by the flowing water. If the oxidized layer is left, it should theoretically be passive and should not conduct. However I found that in most cases there is residual conductivity in the layer and even though it is highly resistive, given that it covers such a large area, this conductivity significantly hinders our measurements. It is possible that the total number of ions that react with the PEDOT:PSS chains are of the right amount required to etch the exposed area and not seep into the required conducting pattern. Once the majority of ions are used up, the speed of the reaction reduces significantly due to lower concentration of ions and allows flexibility on the processing times (which is quite fast, 5 s, and difficult to manually process in exactly the same way on

each occasion). However bleach often degrades over time and its true concentration keeps changing in storage. Due to this reason the bleach was usually simply diluted in a 2:1 water to bleach solution ratio instead of using the accurate values mentioned above. This would possibly cause over oxidation due to the anisotropic nature of the process, but given the large dimensions of the electrodes it should not matter. This was one of the limiting factors when I tried to create PEDOT:PSS inter digitated electrodes of widths less than 50 µm. Some SEM images are shown in Figure 33. It was possible to create 10 µm interdigitated electrodes, but there were far too many errors and while the picture shows a good set of them, the entire device may not have a good yield. Another problem was that for such thin lines, I was not able to over expose and completely etch the exposed PEDOT:PSS. This meant that there was a resistive contact between lines, which was large in its resistance but detrimental to our impedance measurement experiments. More work on the oxidation and patterning process done by J. Zaveri is available in his dissertation [117].

There are other methods of creating PEDOT patterns, such as synthesizing the polymer directly onto the substrate. Long *et al* also managed to create nano wires using the same method, but this makes the total fabrication more complicated and expensive. Patterning of PEDOT:PSS has also been done using reactive ion etching.[118] I did try this however the time taken using O_2 plasma was over 20 mins for a 120 nm layer, thus making it an expensive process and therefore I stuck to using chemical oxidation instead. [119] Agrose stamps and gravure printing can make use of chemical oxidation to mass produce such devices as well.[119]

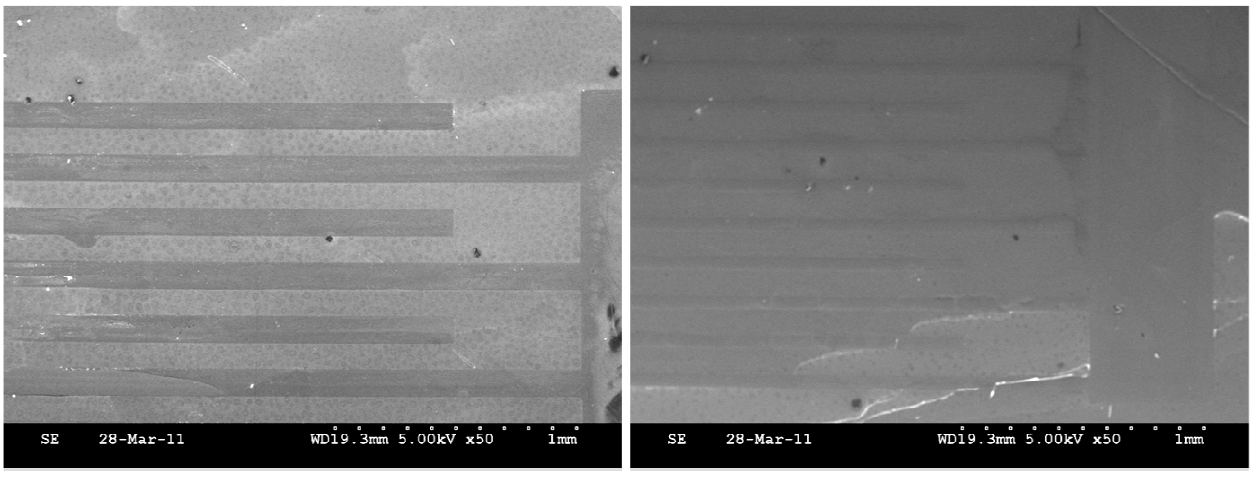

Figure 33: SEM images of interdigitated electrodes. The image contrast is created due to the different conductivities between exposed and unexposed patterns. (left) Well defined 100 µm lines, (right) overexposed 50 µm lines.

Finally the S1818 resist was removed by rinsing in acetone and IPA. The device was then dried out on a 95 ºC hotplate for 5 min and 120 ºC oven for 2 min as PEDOT:PSS absorbs some solvents during the processes. Then the device was cleaned for 20-24 s in the oxygen plasma asher for the next step. This last plasma clean can be quite important and one of the possible reasons why Su-8 peels off during cell cultures. The other possibility is that thinner layers of PEDOT:PSS will absorb water which (since the absorption follows a diffusion pattern [120]) will reach the bottom, losing its own adhesion as well as allowing water under the SU-8 layer. This usually ends in the cell culture failing as well.

3.2.4 *SU8 Insulation Layer and Patterning*

SU-8 3005 (5 µm thickness) is used for the insulation layer as it is thick enough for a reliable and decent insulation layer while not creating an entire wall for cells to climb in and out off. Its processing is far easier as well when compared to the SU-8 3050 (50 µm thickness), which takes far longer baking times and exposure times. Immediately after the plasma ash step in the last process, the device was spin coated with SU-8 3005 at 3000RPM for 30 s and baked on a 95 ºC hotplate for up to 15-20 min. This ensures all bubbles and deformations are removed as unexposed (not yet cross-linked) SU8 has a glass transition temperature around 50ºC [121]. After this, it is exposed in the MA6 with the appropriate mask for 28 s. Post exposure bake is highly important and was done on a 95 ºC hotplate for 1-3 min (The pattern edges should be visible after cooling). Development was done in EC solvent for 1 min, rinsed in IPA and dried out. Finally a bake at 170 ºC-180 °C for 5-10 min on a hot-plate was performed to harden the SU-8 layer else it can be prone to adhesion problems when the device is rinsed with 70% Ethanol. SU-8 is commonly hardened at 180°C in an oven. The oven is not used for any baking as the PEDOT:PSS releases vapors that will form bubbles in the SU-8 layer above. Perhaps a longer bake before the SU-8 layer is spun would be a good option, but I did not wish to bake the PEDOT:PSS too often as I need to consider each extra bake can also degrade the polymer. A final plasma clean in the oxygen asher was done (60 W for 2 min) as I found that it reduced failures due to cells not adhering to the SU-8 surface, or not looking very healthy in many experiments. As mentioned earlier, a problem I faced was delaminating of the SU-8 during cell culturing (after a day or two). One explanation to this is that as the PEDOT:PSS absorbs water it expands slightly. The water also penetrates between the SU-8 and the PEDOT:PSS layers. This causes the SU-8 to lose adhesion and the experiment can fail as water creeps in and the actual surface area of the electrode varies. Also in the

case of stem cells, they would usually die around the area, possibly due to release of chemicals under the SU-8 (IPA etc). Perhaps the SU-8 needs a longer exposure time by a slight amount. The very bottom of the SU-8 is not cross linking properly and would delaminate over longer exposure to the solvents. I however found that baking at 180 °C for 15-20 min really improves this issue which could further explain the need for longer exposure for cross linking. The extra exposure would worsen the resolution for the lithography though. In the final set of devices I used 35 s exposures and this improved the situation. There could be other causes as well. When the devices were scratched at various areas, the SU-8 showed that it is a thin crusty layer. Online resources talk about this problem. It is related to stress in the SU-8 due to cross-linking and subsequent baking. Some people have also considered that the UV exposure over long periods of time (more than 20 s) causes stress and needs to be done in steps. It could also be due to poor adhesion to the glass substrate which could be improved by adhesion promoters (such as AP300). There are techniques of varying SU-8 characteristics by lowering or increasing temp and time during prebake. This is due to the solvent retention being manipulated [122, 123]. Another possible cause for these failures could be that the SU-8 was old. When I used fresh SU-8 at the end of research, I found the layers to be smoother and had no failure in adhesion. However I had only two devices with the new SU-8 and not enough experiments with those devices, along with the fact that I did bake them at 180°C as well, and feel that there may not be enough evidence to completely discard the other possibilities discussed. The final baking can cause PEDOT:PSS to create small pockets of air/solvent that create little bubbles in the SU-8 (Figure 34). These are not holes, just semi spherical bubbles and do not really cause any known adverse effects to the devices. This can be prevented by baking before spin coating SU-8 and baking on a hotplate before any baking in a convection oven. Thus the final baking was a more elaborate process and is described in the device fabrication summary.

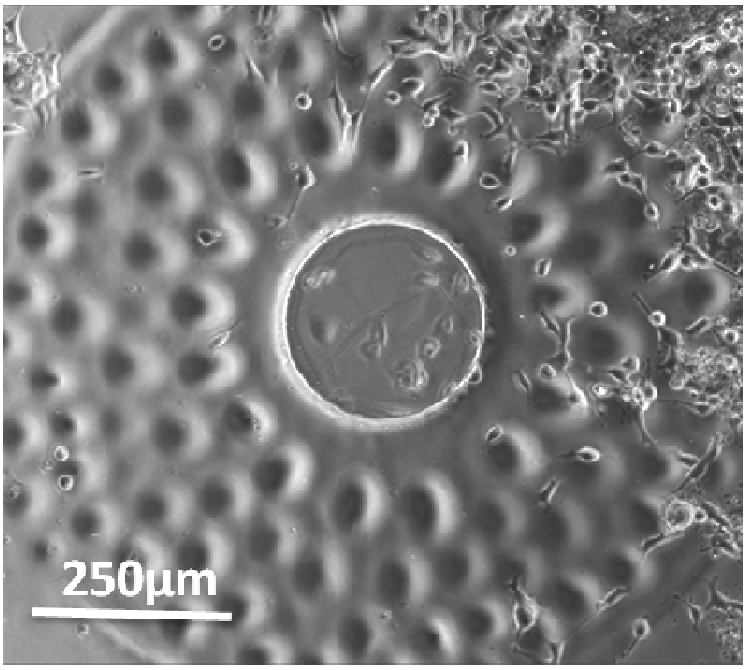

Figure 34: PEDOT:PSS electrode with deformation due to bubble formations, between the PEDOT:PSS and the Su-8 layers, being used in experiment with MDCK cells.

I also fabricated devices that had micropillar structures on the working electrode for the experiments in Chapter 8: . The fabrication of these devices was the same as for the regular devices. The only difference is the mask used for the lithography of the SU-8 must include the pattern for the pillars. I used two masks in a single lithography step but two separate exposures. One mask had the original electrode pattern and the second one exposed only the square pillars on top of the electrode.

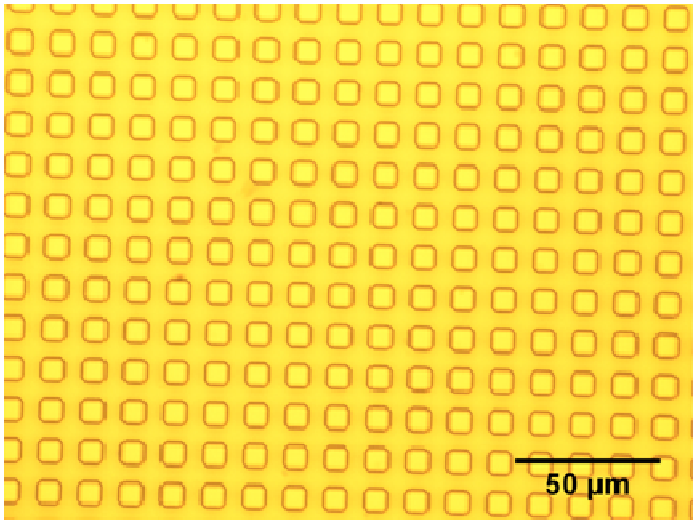

Figure 35: Micrograph showing 7 µm x 7 µm SU-8 micro pillars placed 7 µm apart fabricated on Au electrodes.

Au electrode devices were made using a lift-off process. First a glass substrate was cleaned thoroughly using acetone, methanol and iso-propanol. It was then cleaned using a oxygen plasma for 3 min at 180 W. The substrate was then coated with S-1818 at 3000 RPM for 60 s and baked for 1-2 min on a 95°C hotplate. The resist was then exposed under the appropriate electrode mask for 10 s in the MA-6. It was then developed in a 1:1 microposit developer and RO water solution for 60 s and thoroughly rinsed with RO water. First 2 nm of Ti are evaporated onto the surface followed by 60 nm of Au (using Plassys MEB) and then the device was left in acetone for 30 – 60 min, with the beaker in a 50°C water bath. The beaker was removed and sonicated in a ultrasonic bath for 3 min. The device was then removed and rinsed with acetone and iso-propanol. After a oxygen plasma clean (180 W, 3 min) the device was coated with SU-8 3005 at 3000 RPM for 30 s and baked for 20 min on a 90 °C hotplate. The SU-8 resist was patterned using photolithography in the MA-6 (35 s exposure, developed in EC solvent for 1 min and rinsed in iso-propanol) to define the electrode windows, contacts of the device and the micropillars if required.

3.2.5 *Attaching Wells and Preparing Connections*

The PEDOT:PSS connection ends were coated with silver conducting paint to help the contact with the device connector pins. This needs to be baked on a hotplate at 50-80ºC. Later this coating was also not required once I began using *"ZEBRA"* elastomeric connectors on the PCB. The wells were attached to the devices using silicone glue which was non-toxic to the cells. An epoxy resin was initially used in some of the second generation devices on the outside to give mechanical strength but due to its toxic properties was not used in the third generation of the devices. Finally the devices need to be rinsed with 70% ethanol to sterilize them. This was done by simply adding the solution to the wells using a pipette and leaving it for 10 s, then removing it using a pipette and leaving the device to dry. Just before any cell experiment, the devices were exposed to oxygen plasma (120 W, 1 – 2 min) in the asher. This was followed by any protein coating if needed and then cells were seeded.

3.2.6 *PEDOT:PSS Device Fabrication Summary*

This is the final fabrication procedure used at the end of my work:

Substrate Cleaning

1. Clean the substrate using acetone, methanol and iso-propanol for 3 min each.
2. Clean the substrate using oxygen plasma at 180 W for 3 min.

Alignment Layer and Lift Off

3. Spin coat S-1818 photo resist at 3000 RPM for 60 s.
4. Expose the resist in the MA-6 with the alignment mask for 10 s (7.1mW/cm^2).
5. Develop the resist in Microposit developer (diluted 1:1 with RO water) or MF 319 developer for 60 s followed by rinsing in RO water and drying.
6. Evaporate 30 nm of Al onto the sample surface using Plassys MEB
7. Leave the sample in a beaker of acetone. Place the beaker in a 50 °C water bath for 30 min.
8. Place the beaker in a ultrasonicator for 3 min till all the excess metal has lifted off the surface.

PEDOT:PSS Layer

9. Clean the substrate in fresh acetone and iso-propanol.
10. Clean the substrate using oxygen plasma at 180 W for 3 min.
11. Spin coat PEDOT:PSS (Orgacon S305) at 1000 RPM for 30 s
12. Bake for 30 s on a 95 °C hotplate
13. Spin coat a second layer of PEDOT:PSS at 1000 RPM for 30 s
14. Bake for 5 min on a 95 °C hotplate
15. Spin coat S-1818 photo resist at 3000 RPM for 60 s. Use a primer coating if adhesion is poor.
16. Bake for 1 min on a 95 °C hotplate
17. Expose the resist in the MA-6 with the electrode pattern mask for 10 s
18. Develop using only Microposit developer (diluted 1:1) for 60 s, rinse in RO water and dry. DO NOT USE MF319 as the byproducts will oxidize the PEDOT:PSS and cause the required pattern to lose adhesion and ruins the quality
19. Expose to a 5% bleach solution for 10 s and then rinse under flowing RO water till all the exposed PEDOT:PSS is stripped away.
20. Rinse in acetone to remove the S-1818.
21. Bake on a 95 °C hot plate for 5 min to help remove any solvent that may have been absorbed by the polymer during fabrication. Follow up with 5 min baking in a 120 °C oven.

SU-8 Layer

22. Clean in oxygen plasma for 30 s at 80 W.
23. Spin coat SU-8 3005 at 3000 RPM for 30 s.

24. Bake on a hot plate at 95 °C for 20 min
25. Expose the resist using the MA-6 with the contacts and electrode pattern mask, for 35 s.
26. Perform a post exposure bake for 1 min on a 95 °C hotplate.
27. Develop using EC solvent for 1 min. Rinse using iso-propanol.
28. Bake the finished device on a 95 °C hotplate for 5 min, followed by a bake in the 120 °C oven for 5 min and a 2 min bake in the 180 °C oven.

3.3 **Instrumentation: Design and Development**

The impedance measurement kit was designed and developed by myself and was an important part of the project. It went through many changes and alterations over the course of my work. The final setup used a commercial impedance measurement instrument along with self made software and hardware and is summarized at the end of this chapter. Initially I tried to develop a system for impedance measurement using a NI data acquisition (DAQ) device PCI 6221. A PCB was designed to connect the devices and also provided a high pass filter, attenuator and an amplifier for the receiving end. By applying a signal which was the sum of sinusoids at different frequencies, and performing a fast Fourier transform on the received signal, it was possible to measure multiple frequencies at very fast rates, without having to generate them separately. A Labview program was made to perform all the tasks for generation, measurement, timing and display. This setup however suffered from the fact that the DAQ could not be used for frequencies higher than 25 kHz as its maximum sampling rate was 250 kS/s and if lesser samples were taken per period, the accuracy of FFT was reduced as well as the overall measurements. I felt that I needed to look at a larger bandwidth. The lower frequency spectrum is important for the electrochemical analysis of the interfacial impedance where the Warburg impedance and impedance of the interfacial capacitance are highest. Higher frequencies (up to 500 kHz) are useful for cell impedance measurements. A two wire connection was inappropriate for the accuracy required for the experiments as it suffers from cable parasitic and contact resistance. Thus I started to use a proper Impedance Analyzer (Agilent 4294A) with proper 4 wire sensing (Kelvin connections) which removes the cable parasitic and contact resistance. It also allows us to place a multiplexer circuit in the connection path to the device under test without too much adverse effects to the results.

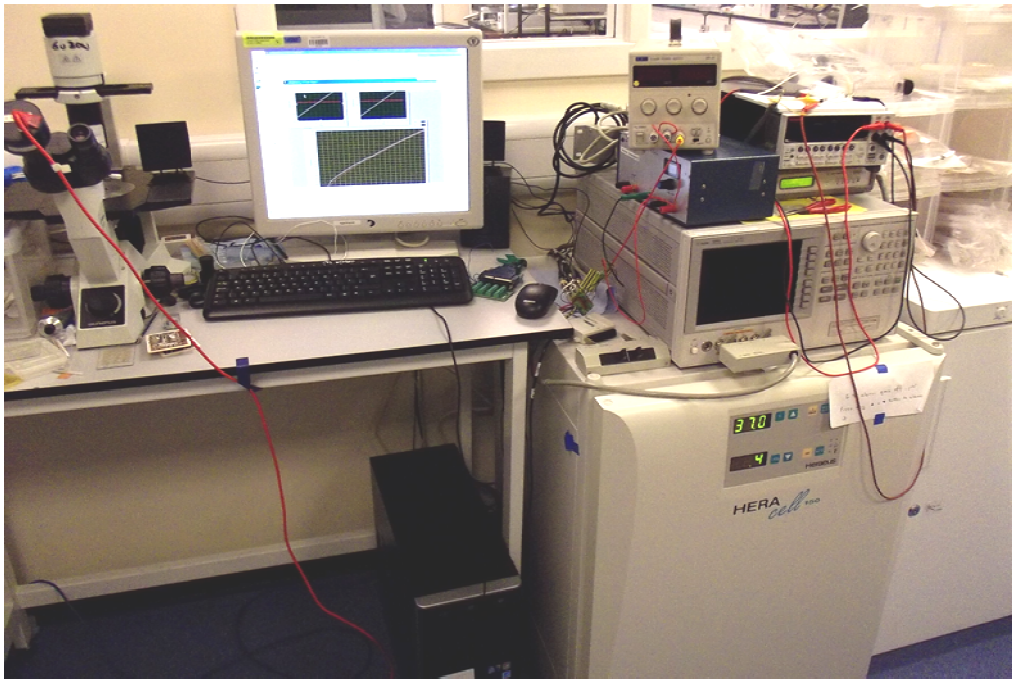

Figure 36: The setup with the Agilent 4294A in the lab.

In time I also used a Quadtech 1920 LCR meter to measure from 20 Hz to 1 MHz as the Agilent analyzer's minimum frequency was 40 Hz (maximum of 110 MHz). It allowed me to have two setups as I was looking at measuring human embryonic stem cell differentiation while continuing my MDCK experiments.

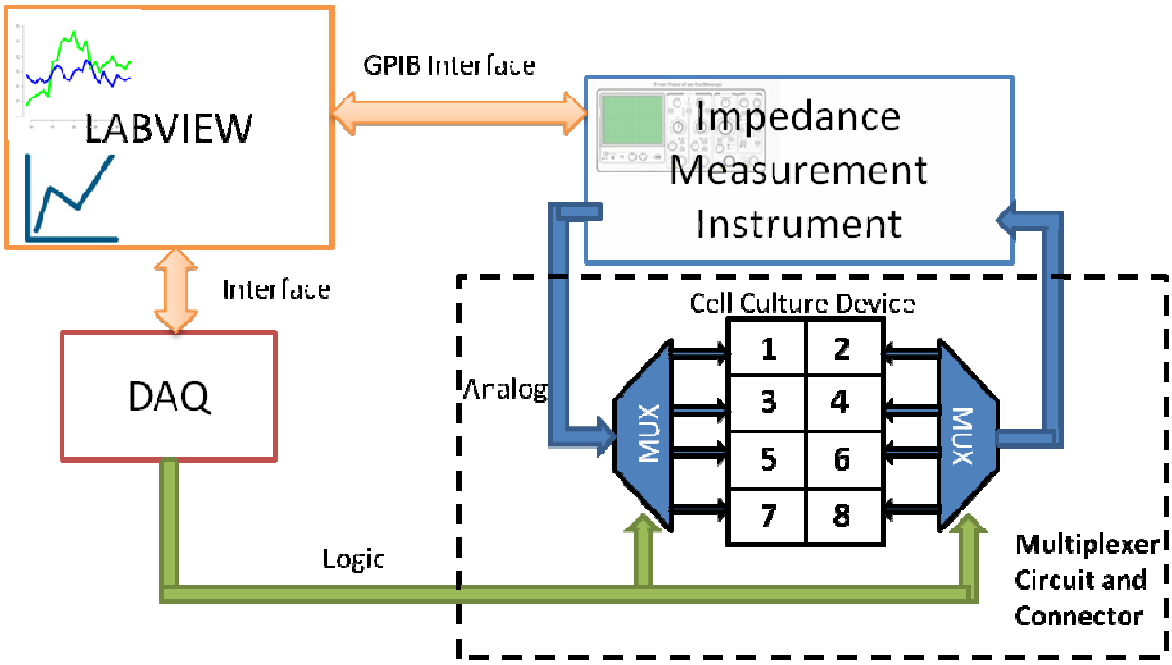

Figure 37: Measurement Setup

The measurement setup has four components as shown in Figure 37. The first is the LABVIEW program created and run from desktop PC. This program controls all of the equipment, records the measurements and stores them in files and folders named according

to the experiment and the well measured. It allows configuration of the hardware and the experimental parameters such as measurement time periods, voltages of the signals, bandwidths of measurements etc. The program will be described in detail after the hardware which constitutes the rest of the set-up has been described.

The second component is the national instruments data acquisition (NI-DAQ) unit which provides an interface between the hardware and the LabView program. Multiple ones were used (PCI 6221, NI-USB 6211 and NI-USB 6008) throughout my work depending on where I was working and with which set of equipment. It does not make much of a difference as they simply provide logic ouput and ADC conversion if the sensor data was utilized.

The third component of Figure 37 is the impedance measurement instrument which is either the Agilent 4294A or Quadtech 1920 LCR meter. Both instruments work using an auto-balancing bridge (Figure 38). The auto-balancing bridge techniques allow us to measure impedance with frequencies up to 110 MHz with a 4 terminal connection. The 4 terminal connections are based on the Kelvin connection method whereby separating the current and voltage measurement cables we reduce the effects of stray parasitic and cable impedances (the voltage cables carry very little current reducing the effects of series resistance etc). The signal source will generate current that will pass through the DUT (Ix) from the Hc (high current) terminal. The Hp (high potential) terminal is isolated so that accurate measurements of the voltage (Vx) can be performed. The current Ix flows into the Lc (low current) terminal. If there is any potential generated at Lc this can cause stray capacitance to be formed between it and the ground leading to errors. The null detector creates a feedback loop that has a virtual ground at the Lc terminal. This null detector can be a differential amplifier in a voltage follower configuration but for accurate measurements above 100 kHz the circuit is more complicated and not discussed here. The current Ir will flow through the Rr (range resistor) and balances Ix. By measuring the voltage drop across Rr we can measure the current and find the impedance of the DUT.

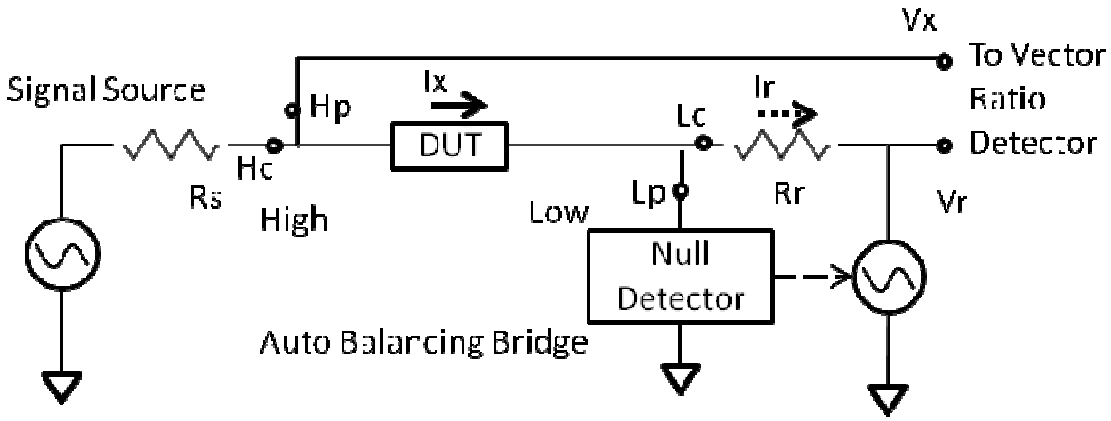

Figure 38: Auto-balance bridge

Measuring impedance can be complicated and depending on the actual impedance value of the device under test (DUT) and the frequency, the problems vary as does the method of connection for the 4 terminals also. The cable connection configuration can be extremely important for the accuracy and precision of the measurements over the entire frequency range. The configurations will affect the accuracy of the measurements either for the range of the impedance or the bandwidth of the test signal. It can be pretty complicated to find the right kind of configuration and in many cases, where my theoretical convention failed me I resorted to trial and error by measuring a self designed calibration PCB. The PCB was a replica of the electrode patterns for the devices with discrete components (SMD component package type used was 1206).

The type of configuration I aimed for was the four terminal pair which also uses the cable shielding to form a loop for the return current. This allows us to cancel mutual inductance between the cable as the signal current flowing through the cores is opposite in direction but same in magnitude to the return current flowing in the shield. The configuration is supposed to cover a wide range of impedance values (1 mΩ to 10MΩ) and in the required bandwidth (20 Hz – 1 MHz). Eventually I also found that connecting the ground of the multiplexer to the cable shields helps with noise reduction. The cables themselves have a finite length along with internal resistance and inductance that also affect the cabling. In the case of the Quadtech LCR meter, it has internal settings that compensate for 1m length coaxial cable inaccuracies. In the case of the Agilent impedance analyzer the cables were longer (extensions attached) due to the instruments size and shape requiring it to be placed in a manner further from the cable port of the incubator. This had some adverse effects and Figure 39 demonstrates the large error above 125 kHz. In some experiments I have done the analysis with a bandwidth from 40 Hz to 100 kHz (Matlab scripting) without any adverse effects as the information above 100 kHz is not essential. I

was able to reduce the error to a satisfactory level later using calibration procedures in the impedance analyzer. However calibrations to a certain standard did not necessarily remove all measurement problems over the entire bandwidth. The cable configuration (even with calibration) is dependant over the impedance values being measured and the bandwidth. Certain cable configurations work best for large impedance values at lower frequencies but are inaccurate for impedances at higher frequencies. Figure 39 shows measurements plots of a 51 kΩ surface mount resistor on the calibration PCB using the Agilent impedance analyzer. The blue plot shows the PCB directly connected to the instrument (no 1 m cables or multiplexer). The measurement is accurate and for frequencies above approximately 500 kHz it shows a small change (negative) in the phase. This is likely due to the parasitic capacitance of PCB pads that the resistor is soldered on. The red plot shows the measurement of the same resistor but with the cabling applied and the multiplexer as well. After approximately 100 kHz the impedance measurement shows inaccuracies. I found that calibrations would improve the higher frequency measurements but at a loss of accuracy at lower frequencies or with some noise being observed. At this point we can consider that our measurements are of parallel resistor and capacitor circuit. That means higher impedance at the lower frequencies and lower impedance at the higher end of the bandwidth.

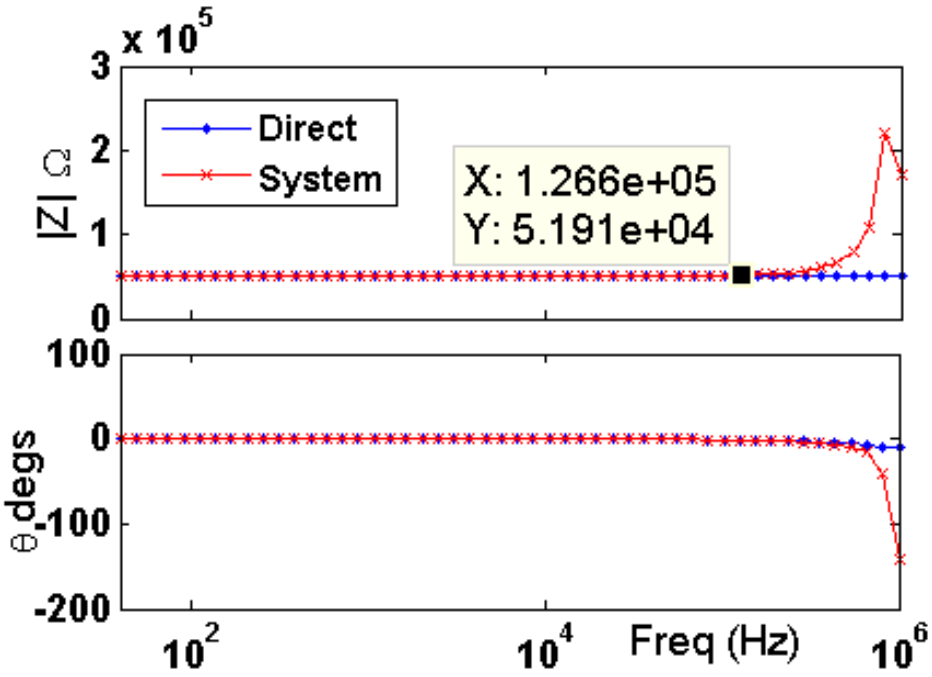

Figure 39: 51 kOhm measurement results with the calibration PCB inside the incubator and connected through the system (System) and the PCB connected directly to the measurement instrument using a adaptor close to the ports (Direct).

Thus I measured the impedance of a 51 kOhm resistor in parallel with a 1 nF capacitor (SMD) on the calibration PCB. Figure 40 shows the results of the measured values of this circuit and the impedance results calculated from a mathematically modeled circuit with the same values. The results show an excellent fit and prove that the accuracy of the system over such impedance conditions is good.

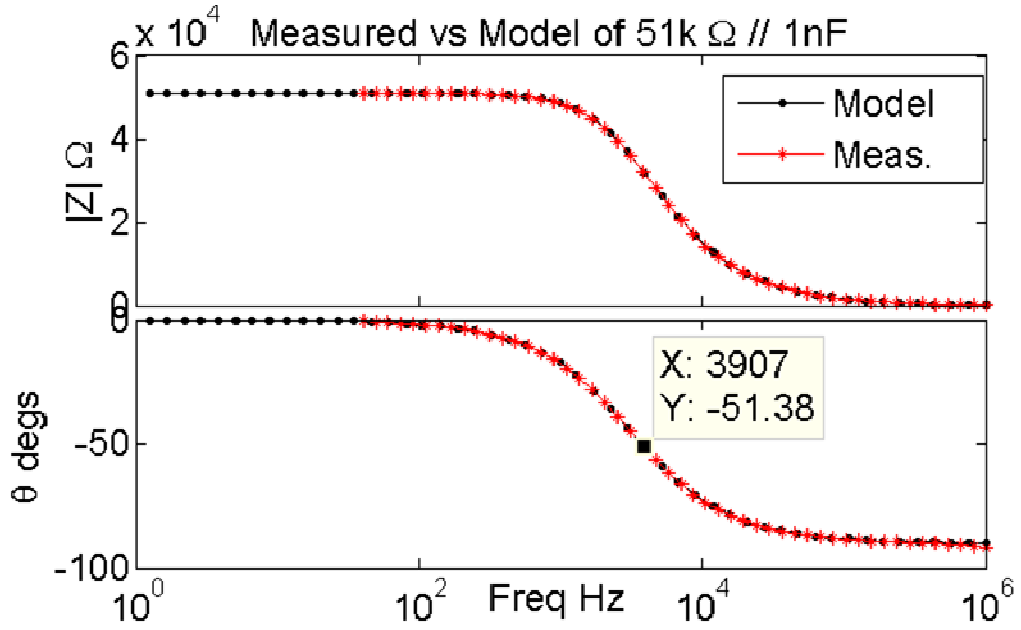

Figure 40: Plots of the measured and modeled impedance values of a circuit with a 51kOhm resistor in parallel with 1nF capacitor.

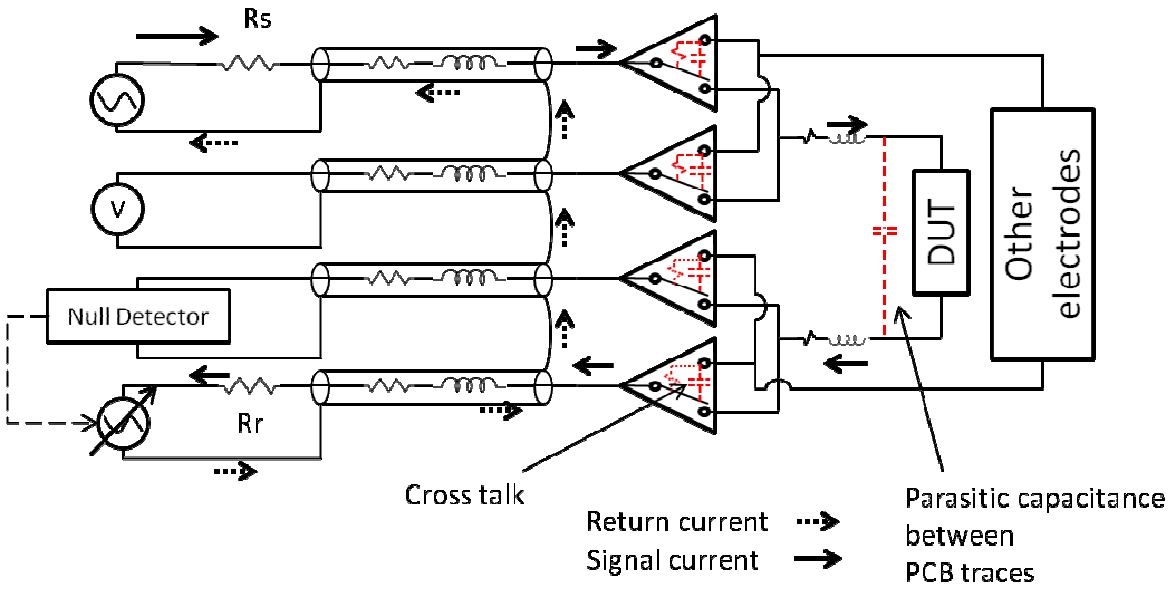

Figure 41: Measurement configuration and parasitic elements.

The overall system configuration is shown in Figure 41 along with the possible parasitic coupling and cross talk paths expected to be present in the multiplexer PCB. The cross talk between channels of the ADG726 would be minute in comparison to the

inductance and resistance of the PCB traces and the coupling between electrodes etc. These values may not be measured as easily as I would have liked but by measuring known elements (calibration PCB) I felt confident in the results. When considering the PEDOT:PSS electrodes own resistivity and the fact that the material would not behave like some ideal metal, the errors were small, and can be ignored. What is important is that the measurement system should be able to measure reasonably well in the mega Ohm range for frequencies below 1 kHz and below 100 kOhms at higher frequencies (conforming to the impedance spectrum of a typical capacitor and resistance in parallel, which is what corresponds to anticipated values in the cell measurement).

Finally the fourth component in Figure 37 is the multiplexer (MUX) circuit (Figure 42) which allows measurement of multiple wells one at a time. This circuit utilizes ADG726 integrated circuits (IC's) to connect a set of electrodes to the measurement equipment. Initially I used the ADG904 (4:1) multiplexer IC's which provided very low 'ON' resistance and bandwidth up to 1 GHz. This however limited the number of experiments I could perform at a time and was alright till the second generation devices. After I realized that I required more wells, I switched to the ADG726 which has a good bandwidth (-3dB @ 34 MHz) for our requirements and a decently low 'ON' resistance (4 Ohms). The ADG726 is dual 16 channel analog multiplexer thus allowing four 16 channel multiplexing using only 2 IC's (for a 4 probe Kelvin connection). The current and voltage paths are joined right after the multiplexer so that errors due to the IC's are reduced in the path. This is another reason why using the four probe method is essential as it negates effects of the impedance due to the IC's in the path similar to what happens to cable parasitics. The IC's are powered with a 2.5V and a -2.5V supply. The circuit is connected to the main power supply and NI-DAQ units via a DB25 connector. The main power supply is a DC power supply that provides 12V, -12V and a ground. The circuit has its own power supply regulation (using Low drop out regulators LDO's) so that it can provide 5V,-5V, 2.5V and -2.5V supplies to IC's and sensor board. The NI-DAQ provides all the logic for the multiplexing and all the IC's are connected to the same 4 bit data connection. This way each MUX is configured for the same input/output for each measurement. This can limit the device design but provides a simpler PCB layout and reduces the chances of creating errors due to logic and programming. The PCB was made on a double sided board, meaning it was not possible to shield the tracks. However the paths from the point where the high and low contact would join (after passing through the IC) to the contacts of the device were not very long. Ideally it would be good to have some form of four layer PCB with ground planes above and below the tracks and separate contacts for each voltage

and current wire. Results shown in Figure 40 show good accuracy over the required frequencies and around the expected impedance values. Therefore I did not spend more time improving the PCB.

The circuit board also has a sensor board which has a temperature and humidity sensor, outputs of which are sent through the DB25 connector to the ADC's of the NI-DAQ unit. This was used initially to understand the effects of temperature and the surroundings especially when the incubator door was opened frequently by other users. Later once I started using a container to cover the device (and ended up using an incubator exclusively for my project) and the circuit, it did not matter much. The power supply and the sensors were on separate PCB's which could be slotted easily using board edge connectors. This allowed me to play around with my multiplexing switch PCB design without having to constantly redo the power supplies and sensor circuitry. The MUX board is also the connector for the device. For the second generation devices this was a horizontal board edge connector and the device was simply slotted into it. Later with the 8-well devices, I changed to something more different as I had many mechanical failures due to scratching of the device connections (PEDOT:PSS and the silver paint). I designed the PCB such that it could host pins that were bent (allowing for a mechanical spring action) that would connect to the device and were tightened by force applied with screws on the PCB. Later the pins were changed to gold "ZEBRA" elastomeric connectors that then allowed direct connection to the PEDOT:PSS layer without the need for silver conducting paint.

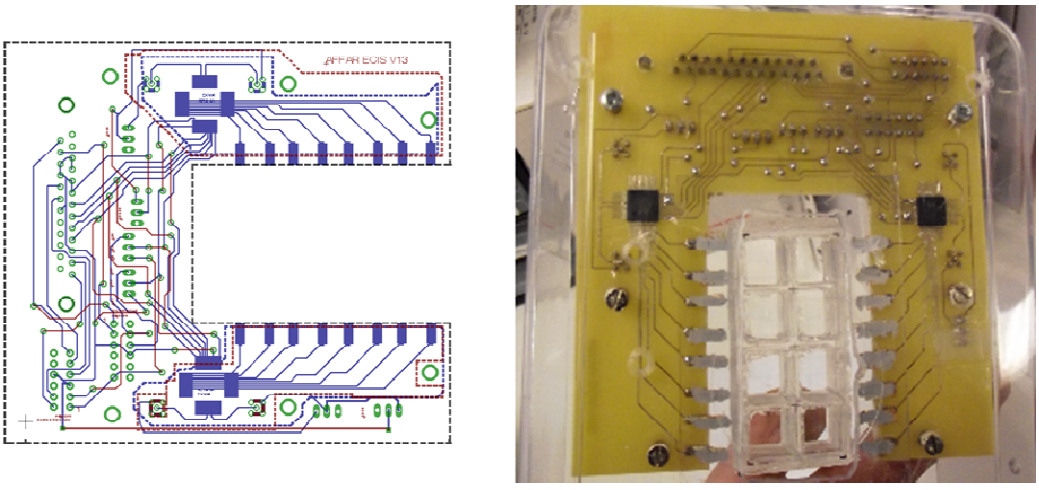

Figure 42: Multiplexer circuit board, layout (left) and holding a device inside the plastic container.

The LABVIEW program differs for the two impedance measurement systems in how it collects the data, but overall is the same in terms of storing that data and how it

displays it. Initially it will configure the instrument and save all the configuration details in a file (“expparam.txt”). The program creates a folder with the experiment name (set by the user) and saves the configuration data file in that folder. All the files for the particular experiment will be saved in the same folder. This is extremely important for all the MATLAB scripts that are used to generate different graphs and analyze data (results section) as all the scripts have a general method of loading the data into memory before processing it. It will then move into a while loop that will have its iterations separated by a time gap which is set by the user. This time gap is the delay between each measurement and must be larger than the overall time taken by the instrument to complete measurements of all 8 wells. The total time taken depends on the total number of frequency points that are measured and at which kind of accuracy setting (Quadtech 1920 has different modes of accuracy that affect its measurement time per frequency point). In most experiments the number of frequency points was set to 50 and a safe bet for the minimum delay was 5 minutes. The program will end once the user stops the entire program from running. The configurations cannot be changed once the program has started.

Inside the while loop we have sequences which occur one after the other. Each sequence will first set the logic for the multiplexer to connect the appropriate electrodes to the instrument. Then the instrument is called upon to measure the data and pass it on to the program which will then arrange the data to be sent for graph display and file storage. Each while loop iteration will also save the data files to a network location specified. This allows me to monitor my experiments from any location. The length of each experiment can be long and the program needs to be paused or stopped when media is being changed or pictures taken of the cells. I found that if the program is paused and run over the entire duration of more than 2 days, the PC can run out of memory and the program crashes. This is a problem (possibly due to the graphs being displayed) as memory is not being used in a efficient manner. Perhaps there is a need to specify memory release however this would not be possible if that data was being used to display graphs. It was not an essential requirement and I proceeded by simply stopping instead of the pausing the program. The folders were separated by numbers at the end of the experiment name and the data was later put together using a MATLAB script.

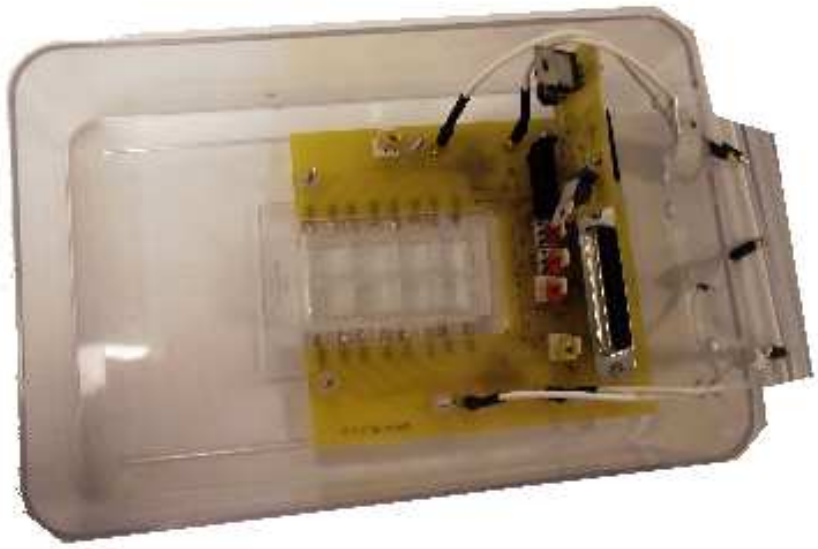

Figure 43: MUX PCB holding the device inside the container. This is the final result of all the fabrication and system design work which sits inside the incubator.

3.4 **LABVIEW Software Design:**

I used Labview to create a control program for the measurement devices and experimental setup. There were two different instruments used, the Quadtech 1920 LCR meter, and the Agilent 4294A Impedance analyzer. This required two different programs as the LCR meter did not do frequency sweeps, thus the program had to cater for this. For the impedance analyzer, it only needed to be provided with the input parameters and triggered for each frequency sweep. Then the data can be extracted and the iteration repeats once all the wells have been measured.

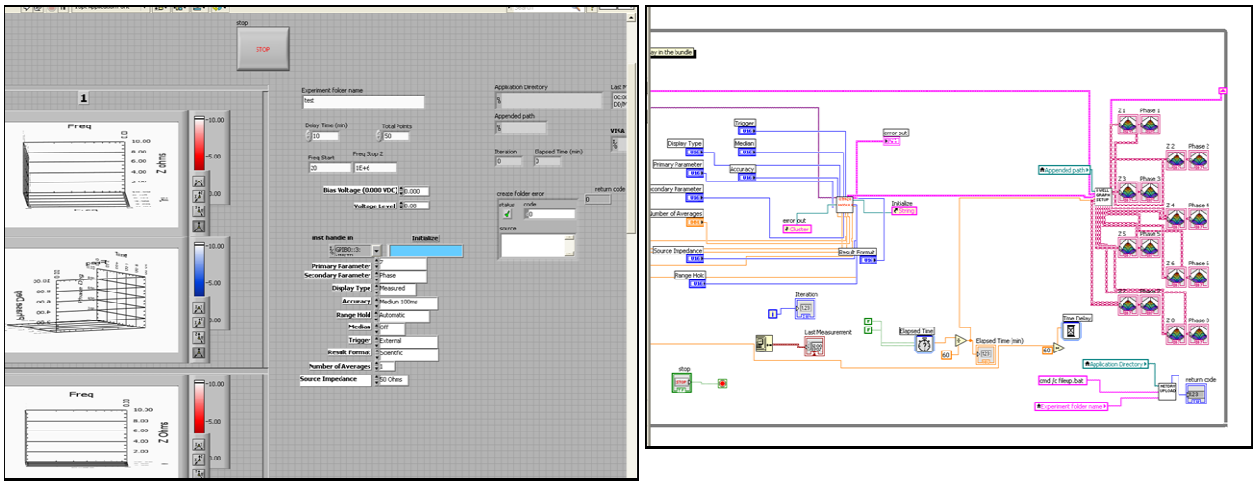

Figure 44: Screen shots of the Labview program. (Left) Front panel, (Right) block diagram window.

Figure 44 shows the screen shots of the main program. The front panel contains the user input controls and the graphs to display the data while the experiment is being run. The block diagram contains all the VIs (virtual instrument). The VIs for the interface between the PC and the instruments were taken from the National Instruments database. These were then used to create my own VIs that were part of the main program. The program starts by storing all the user input information (voltage, time started, folder name, total number of frequency points etc) and stores them in a file (“expparasetup.txt”) which is essential for the MATLAB scripts to generate the graphs. The program will then enter a loop (this one will continue till the user presses stop) where the measurement, graph generation and data storage VIs will perform their functions. The measurement VI has the VIs that communicate with the instrument via GPIB protocol and also provide the logic for the multiplexer via a NI-DAQ (National Instrument Data Acquisition) hardware device. These are run in a loop until the final well is also measured and the data is stored in arrays that are passed to the main program once the iterations are completed. In the case of the LCR meter, a single frequency is measured, the frequency is changed and the measurement started again until the final frequency is measured before the multiplexer switches to another well. Once all the measurements are done, the data will be passed to the graphs and data storage VIs which will display them in the front control panel and store the data in the respective files and folders. The network upload VI will store all these files onto a network storage drive so that the data can be monitored from anywhere. Once this is all finished, the main program will wait till the delay period between each measurement iteration for the experiment has elapsed before beginning another one. The whole program will stop only once the user requests it. The graphs can be generated using the data files and

MATLAB scripts. The curve fitting algorithms and scripts also use the same files for analysis.

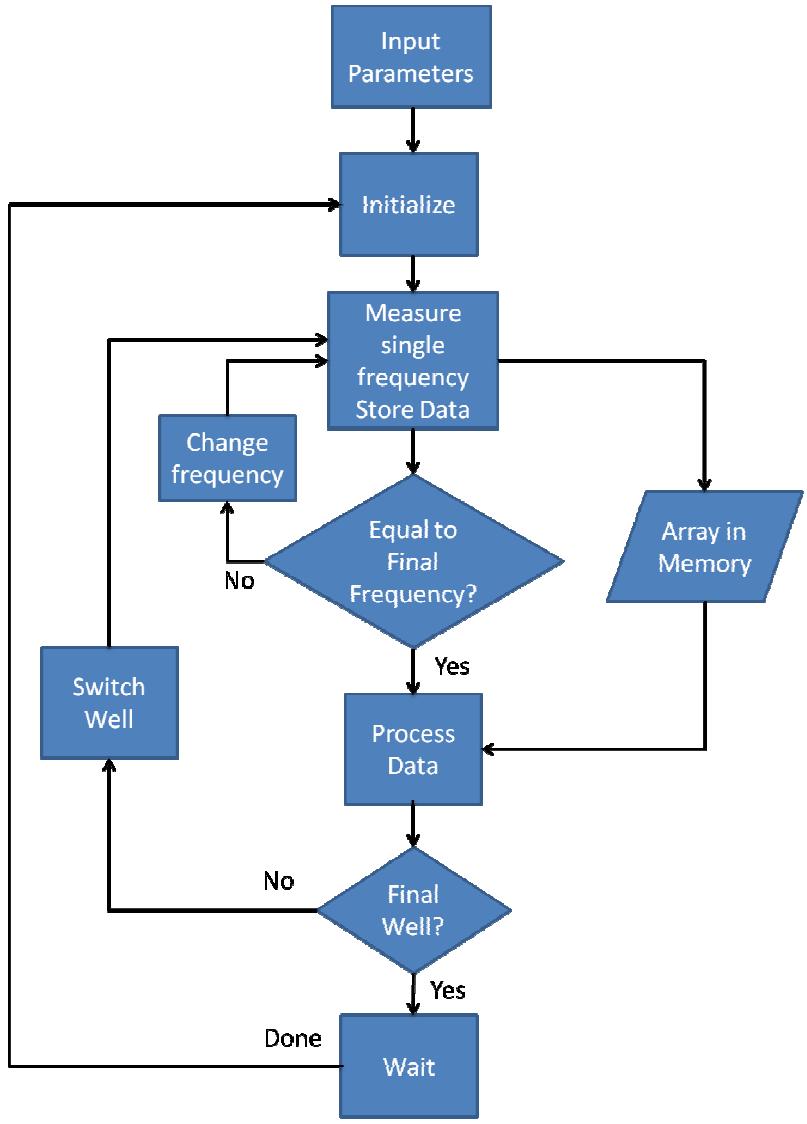

Figure 45: Flow diagram for the Labview program to control the 1920 Quadtech LCR meter.

3.5 Curve Fitting Using Complex Nonlinear Least Square Method:

Regression analysis helps to understand the change in a dependant variable to a independent variable by keeping other independent variables constant. A Regression model will relate the dependant variable Y to the independent variable X as shown in equation in Eq. 18, where β are the unknown parameters.

$$Y \approx f(X, \beta) \qquad \textbf{Eq. 18}$$

Non-linear least square method is a type of regression analysis that tries to minimize the sum of the squares of the residuals (Eq. 19).

$$S(\beta) = \sum_{i=1}^{m} [y_i - f(x_i, \beta)]^2 \quad \textbf{Eq. 19}$$

The Levenberg-Marquardt algorithm most commonly used to solve the problem of minimizing the function. The method is iterative and will vary each parameter separately till it finds the minimum residual. In complex non-linear least square (CNLS) complex data is used to find parameters of a complex function. Its implementation in MATLAB is not so straight forward and the real and imaginary parts are split into two parts but form the same array. The real parts are placed first (assume *n* number of elements) and the imaginary parts of each of the k^{th} real part is placed at $n+k$ in the array. This is then used as a single set of data for the *lsqcurvefit* function of MATLAB and the complex results of the function being fitted are placed in a similar manner in its own function file. It is important to make sense of the results of the curve fitting as one must realize that the numbers could be simply providing a good curve fit but not necessarily realistic values. Some of the unknowns can be calculated (such as R_s and R_t) and be used as initial conditions for the curve fit with some limits applied.

3.6 **Summary Of Instrumentation Setup**

The final kit was based on around a Quadtech LCR meter that connected to the fabricated device via a multiplexer circuit. The multiplexer circuit allowed 4 probe connections (Kelvin connections) by having four multiplexer for each current and voltage line. The connections would join just before the metal connector that would touch the connector pattern on the fabricated device (the silver paint coated ends). This was not ideal as there would be contact resistance, however it removed impedance due to cabling and the multiplexer IC's sitting in between. It was limited as such due to PCB design constraints and can be improved in the future by simply adding more contacts and separating the metal traces at the contacts. The setup could measure high impedance values (approximately up

to 3 MΩ) below a frequency of 100 kHz and low impedance (approximately under 50 kΩ) above that frequency.

The multiplexer circuit board also acted as a mechanical housing for the device and had its own power regulation, requiring only positive and negative 12 voltage inputs (along with a reference ground) and digital logic (from a National Instrument data acquisition device). The multiplexer circuit was the only component from the setup that required to be placed inside an incubator during an experiment.

A software program (made using Labview) ran the entire kit, measuring each well of the fabricated device. The software provided variation in voltages, biasing, and timing of the data acquisition. It also allowed the data to be stored continuously onto a network drive for external access. The data was analyzed using Matlab scripts which could generate graphs and perform curve fitting to custom mathematical models.

Chapter 4: **Early Experiments**

During the course of my work, I performed quite a few experiments that would help me gain confidence in each step as I went along. Since the fabrication, the electrochemical impedance, and the cell culturing are all related, it is important to alleviate ourselves of any conflicting thoughts else it could affect the other analyses as well. These experiments are presented here.

4.1 **Fabrication Chemical Tests**

In order to insure that the chemicals involved in the fabrication process did not degrade the polymer, I performed a few tests to see what happens to the polymer impedance when exposed to them. The experimental setup (Figure 46) was simple and not the most accurate but helps provide enough information about the effects of the chemicals, whether they totally degrade the polymer or have negligible effect on it. The experiment was done using strips of glass substrates coated with PEDOT:PSS. The ends were coated with silver conducting paint and soldered with wires that were connected to an impedance analyzer. A cut off from a tube was glued onto the center of the strip fully covering the two edges. Measurements were started and the chemical was poured just enough to cover the PEDOT:PSS layer. The end values shown in Table 3 are the measurements after approximately 1 min.

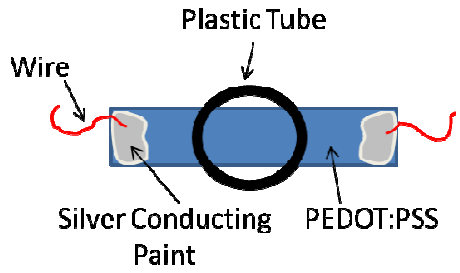

Figure 46: Chemical test experimental setup.

Chemical	|Z| Ω @ 20Hz, Start	|Z|Ω @20Hz, End (after 1 min)
Acetone	1269	1296
Bleach	1667	349140
Microposit Developer	1000	1309
RO water	1558	1645

Table 3: |Z| measurements of conducting polymer strip exposed to chemicals.

There is the possibility that current will travel through the solvent as well, especially in the event the PEDOT:PSS strip looses its conductivity (bleach). Nevertheless the results can be indicative of chemical behavior. RO water and Acetone do not do anything significant but the Microposit developer does increase the resistivity slightly, and the bleach shows expected results due to its oxidative behavior. Observations during fabrication tell me that the byproduct produced while developing S1818 (using Microposit developer) cause serious oxidation of the PEDOT:PSS. I have not performed any tests or experiments to prove this however I have seen the PEDOT:PSS layer exposed to the developed S1818 become brownish and shows loss of adhesion. It does not matter for my fabrication step as the mask is positive.

4.2 Tests with Saline Solutions and Temperature Dependance

In order to be certain out about our controls during the experiments, I measured the characteristics of the different media that would be used over 24 hrs. Interestingly all types of media used showed a constant change in |Z|. This change would be reset (in all the wells) when media was changed during cell experiments. This behavior could be related to: changes in pH (should not really happen with control wells); absorption of CO_2 (should probably be a logarithmic change with time as it would be a diffusion process [124]); interactions on the electrode-electrolyte interface (should not happen over such long time periods); or could be related to changes in concentration due to evaporation of solvent once placed in the incubator. In the case of PEDOT:PSS it can also be due to the polymer changing its chemical characteristics by absorbing water or ions travelling into and out of it, its redox state or slow dissolution.

I did some tests using a 0.154 molar NaCl solution and a Au electrode device to understand the effects due to possible evaporation of solvent leaving behind an increase in ionic concentration, or what happens if I add more media to the wells. The first one (Figure

47) shows the impedance of different volumes of the same salt solution. A higher volume has larger impedance at the lower frequency showing higher impedance in the Faradaic path. If we look at the earlier modeling shown in Figure 15 we can see that the increasing lower frequency impedance with a flattening of the phase (and straightening of the Nyquist plot) shows that the majority of the increment here is in the Warburg impedance. If we consider the finite length Warburg impedance model, and assume that the Nernst diffusion layer is larger than the height of the liquid in the well, then this increase in the Warburg impedance can be related to an increase in the length of the solution. Electric fields will not only travel a path parallel to the surface but will span out into the solution. Since the solution is now higher, the path length for the electric field has increased hence increasing the value of the Warburg impedance.

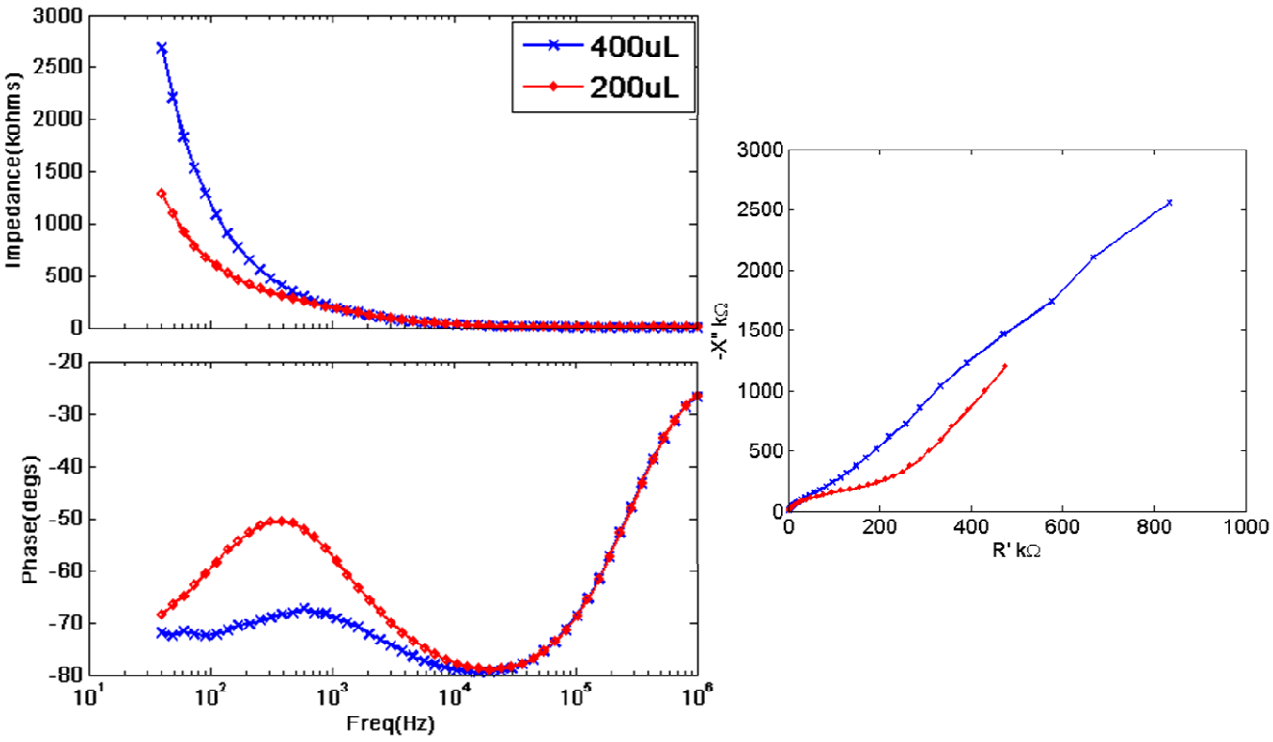

Figure 47: Impedance of a 200mmolar NaCl solution, 400µL and 200µL.

Second test I did was to use same volume (400 µL) of solutions with different concentrations of NaCl. Figure 48 shows the measured impedances with an insert showing the lines at 100 kHz. The insert shows there is substantial change in series resistance as well. At both of the frequency ends we can see that lower concentrations lead to higher impedance. In the case of the lower frequencies we would usually analyze the Faradaic path. However the impedance due to the capacitance of the double layer is in parallel and will also contribute if it changes. As explained in 2.2.1 and shown by Figure 7, the capacitance will increase for higher concentrations of ions. By increasing the concentration

of the solution, we have thus reduced the impedance. The Warburg impedance is also inversely proportional to the concentration however looking at the results of the volume experiment above, we can observe that the difference due to concentration is mostly due to changes to the interfacial capacitance. The charge transfer resistance is not dependant on the concentration of the solution, though neutral species and a lesser access to ions could increase it. At higher frequencies it is simply a case of lower concentrations having less conductivity.

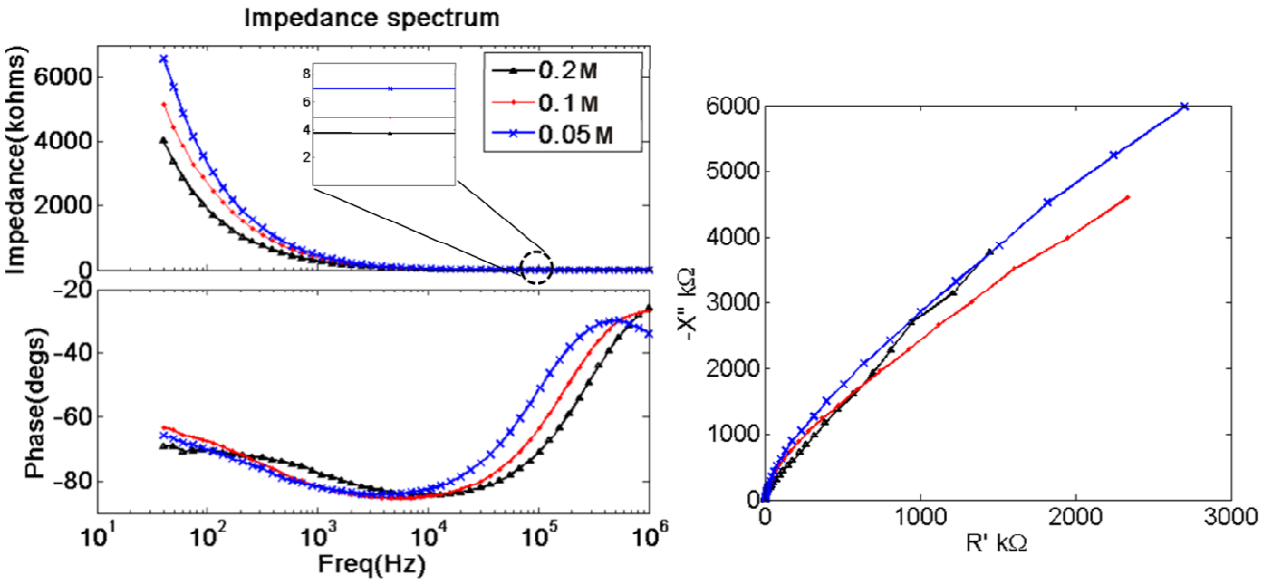

Figure 48: Changing the solutions salt concentration, results of two wells. The concentrations in the legend show Molar (Mol/dm^3) values.

Another thing to consider is the temperature. During my MDCK experiments, I found that the setup was susceptible to temperature changes even if the incubator door was opened for a short duration (5 seconds or less). This is highlighted in Figure 49. The temperature shown in the plot is lower by 11°C due to an offset error in my setup. Even a change of 2°C can cause the impedance to change by a large amount especially in the case of Au electrodes. The resistance of a 0.1 M NaCl solution for 3mm (distance between electrodes) at 37 °C is 22.8 Ω and at 35 °C is 23.5 Ω (calculation shown in Appendix). Figure 49 shows the change in |Z| to be of almost 15 kΩ at 100 Hz. That is too large to be due to simply a change in the resistivity of the electrolyte. Figure 49 also shows that the change is dependent on the frequency and larger for lower frequencies. Hence this may have to do with R_t, A_w and the interfacial capacitance, C_d as all three are dependent on the thermal voltage and hence the temperature. It is therefore expected that the variation in temperature will play an important role in the impedance measurements, especially at lower frequencies.

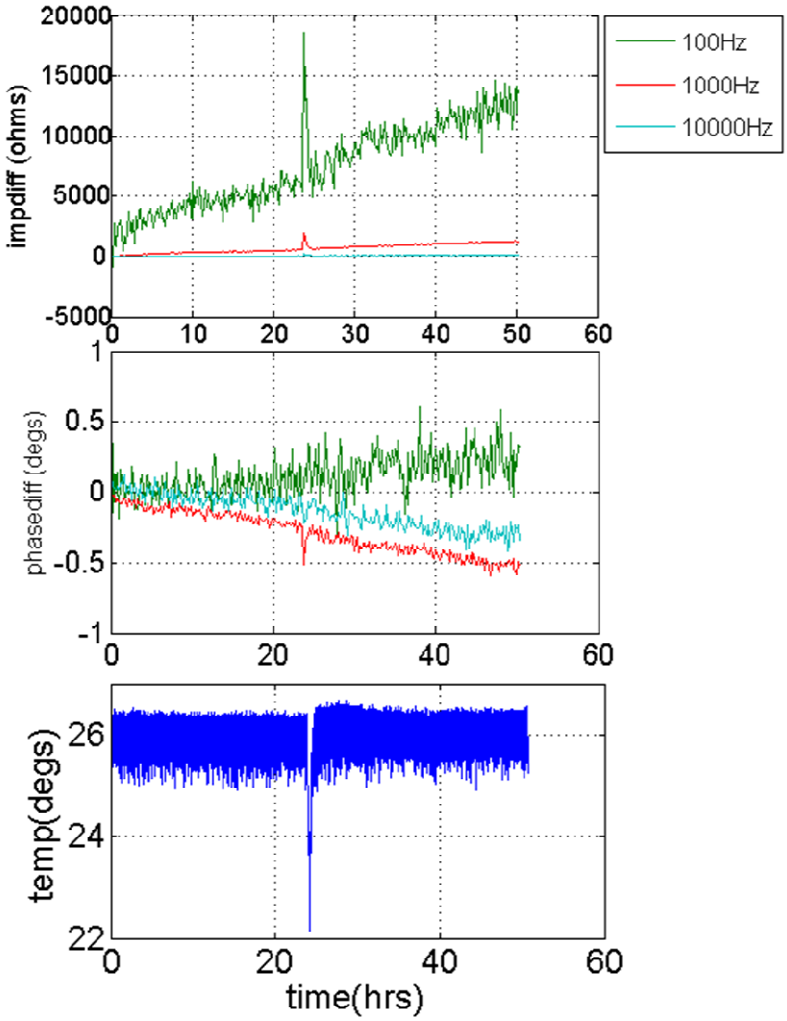

Figure 49: Changes due to temperature variations. The temperature measurements had an offset. The temperature was actually 37℃ when it shows as 26 °C. The legend shows frequency values of the plots shown.

Chapter 5: **“Gold vs Pedot”: A Comparison Study**

Cell impedance measurement sensitivity is dependent on the characteristics of the electrode-electrolyte interface. The interfacial capacitance and charge transfer resistance are the most crucial in this respect. Higher impedance values due to the two can result in the noise obscuring the impedance changes due to the cells. It also means any measurements of current/potential at the electrodes (example the action potential for electrodes used in neural implants) will have high impedance in its path that is undesirable. (These characteristics are related to the material used, electrode geometry, applied potential and the media being used. The media we are using is chosen in regards to the cell being used and cannot be altered else it could affect cell growth and behavior. The electrode geometry can be altered; however we would like to keep it as small as possible if we want to focus on single or handful of cells. The changes due to fewer cells being would have a larger effect on the measurements and would help in understanding the experiments. If we prefer to look closer at the cells through a microscope then to see the entire well plate and having a small electrode helps to insure that the results are related to only the area being monitored. The electrode surface area can also be increased using methods such as platinization to create platinum black, but this leaves us with a question about what affect does the surface morphology have and what actually is the exact surface area. The material choice for electrodes is crucial and having different available options is very useful.

We investigated the differences between using PEDOT:PSS and Au as electrode materials for CIS. The basic differences between the two in their physical characteristics is common knowledge, but the electrical behavior of the two electrode materials under cell culture conditions needed to be studied further. Earlier research had shown the benefits of PEDOT:PSS for its charge injection capabilities and its electrochemical behavior. Here we would like to assimilate those studies and use them to compare the electrochemical characteristics of the two materials. The materials are compared by analyzing results of a cyclic voltammetry experiment and looking at the impedance models of the electrode

interface. By using complex non-linear least square (CNLS) curve fit techniques we can find values for our electrical models of the electrode interface that match the impedance measurements from experiments.

5.1 Cyclic Voltammetry

The cyclic voltammetry was done with a Keithly 2400 series source meter. The electrolyte used was HEPES saline (HS solution) and a silver wire with silver chloride coating (Ag\AgCl) was used as a reference electrode. The instrument was controlled using Labview and the voltage sweep rate was 0.1V/sec, ranged from -0.5V to 0.5V.

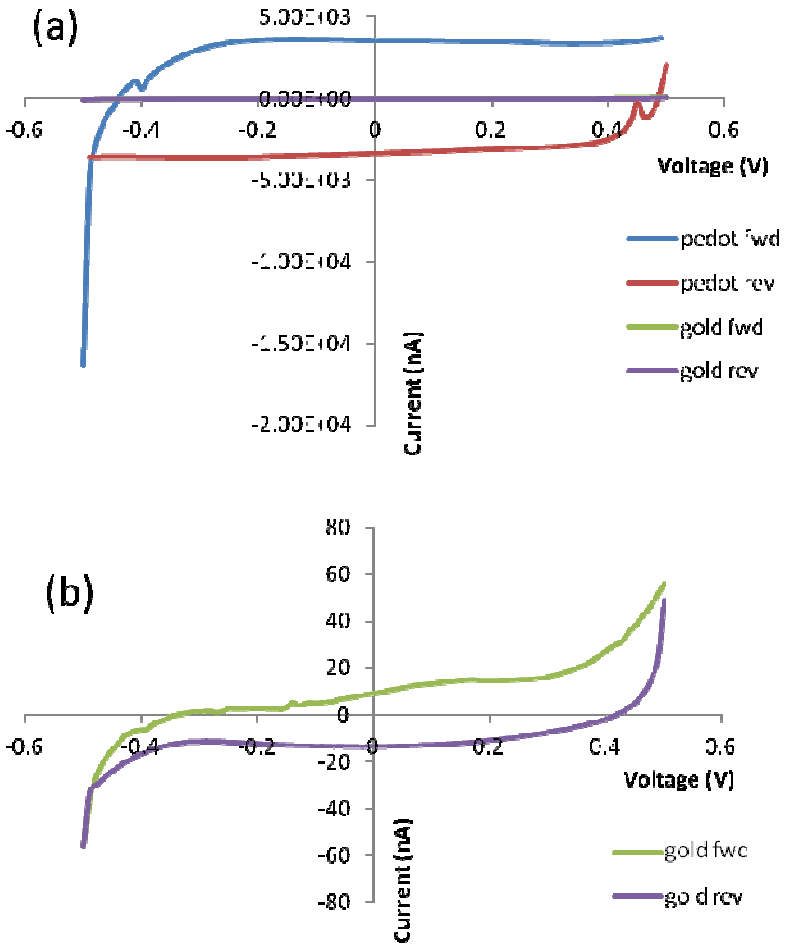

Figure 50: Voltammetry results of (a) PEDOT:PSS electrodes (and Au electrodes) and (b) only Au electrode, with HS solution.

The PEDOT:PSS results (Figure 50 (a)) show an error as the start of the forward and the end of the reverse current are far apart. This was most probably due to some form of delay and setup of the instrument as it would reduce if measurements were started constantly at quick rates one after another. The second error is the discontinuity between the forward

and reverse paths which can be seen in both graphs. This is because the setup was not designed to start again from the same positive voltage for the reverse sweep but just continues on from the forward sweep and doesn’t measure the first voltage for the reverse sweep in the manner it should. These features do not negate the validity of the results and are accurate enough to support this discussion. The first graph (a) shows results from PEDOT:PSS electrodes and Au electrodes both. The difference in current is so vast (almost by a factor of 300) that the gold curve looks like a flat line. The current and rate of voltage change relationship is given by Eq. 20

$$I = C \cdot \frac{dV}{dt} \qquad \textbf{Eq. 20}$$

This indicates that for the same rate of change of voltage, the current is proportional to the capacitance of the electrodes. Thus PEDOT:PSS has a higher interfacial capacitance that requires a larger charging current. This is further proven with electrochemical impedance analysis of the electrodes.

5.2 **Electrochemical Impedance Spectroscopy:**

Impedance spectroscopy results of Au and PEDOT:PSS electrodes were used to find the model parameters that will characterize the electrodes. The electrodes were of the same dimensions, with a working electrode area of 4.15×10^{-4} cm^2 (230 µm in diameter) and the reference electrode area being 6×10^{-2} cm^2, which is sufficiently large enough to have minimal contribution on the impedance values measured. The amplitude of the signals used for the electrochemical comparison was 20mV, which is low enough to work in the linear region of the current-over potential relationship [76, 79]. The amplitude for CIS measurements was kept higher (80mV) which was set after it was observed to be free of any noise when measured using both types of electrodes. It is small enough to be free of harmonic distortion and neither caused any adverse effect to the cell culture. I have used complex non-linear least square (CNLS) curve fitting to find the values for the theoretical electrical equivalent model. I have also applied weights to the curve fit to better evaluate the results. Initially the model used was a simple capacitor (the double layer capacitance ‘C_{dl}’) in parallel with a resistor (charge transfer resistance ‘R_t’) and both in series with another resistor (solution plus any other series resistance ‘R_s’).

$$Z_{electrode} = R_s + \frac{1}{j\omega C_d + \frac{1}{R_t}} \qquad \textbf{Eq. 21}$$

Figure 51 shows the results of the curve fit to this model. While the model does show significantly close behavior in the real part (R) and the imaginary part (X) of the impedances, the fit is not perfect. The points marked 1 and 2 show large deviations (the values are with a factor of 10^5). At point 1 the measured R is lower than the calculated one. At point 2 in the plot for R, we can see how the actual measurements have higher impedance in the middle region of the spectrum. The phase shows similarity in shape but are positioned differently over the frequency spectrum. It can be judged that there is a further frequency dependency element required in the model.

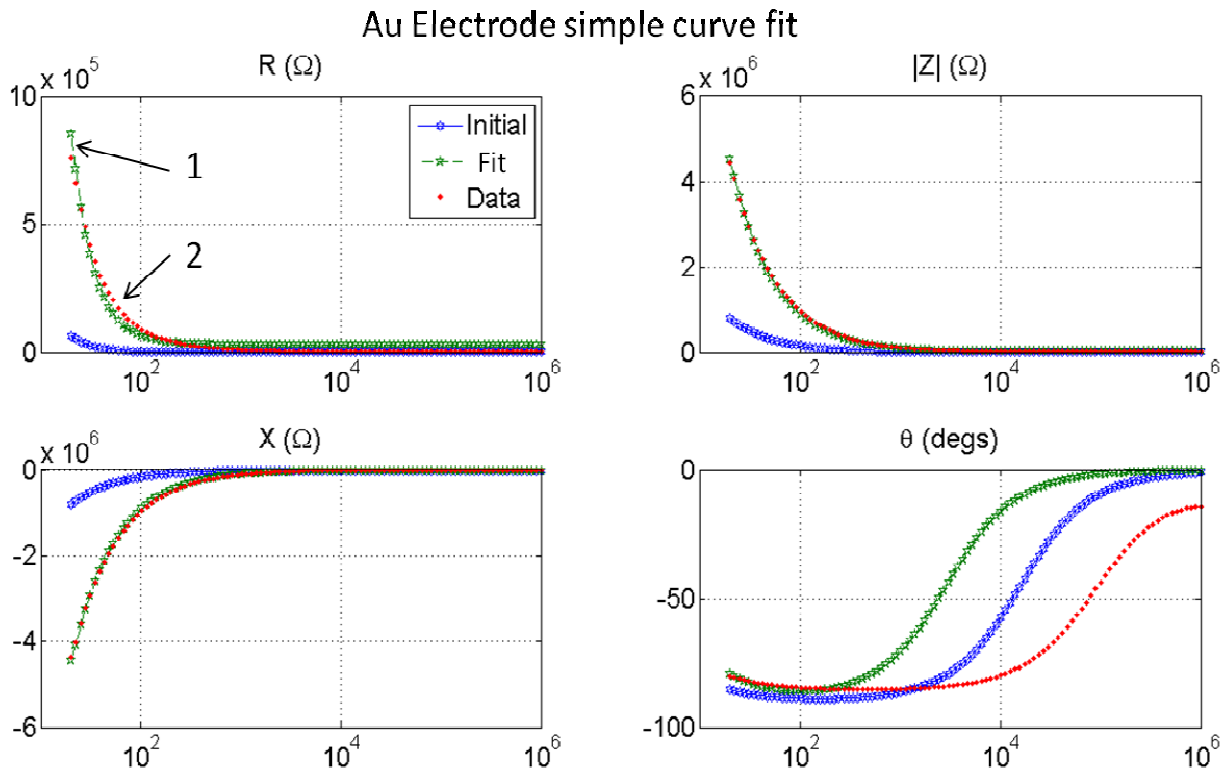

Figure 51: Curve fitting results for Au electrodes with HEPES saline solution using a simple model. Blue line (circle marker) is the results of using the initial parameters, the red line shows the real measurements, and the green (star marked) line shows the final curve fit results.

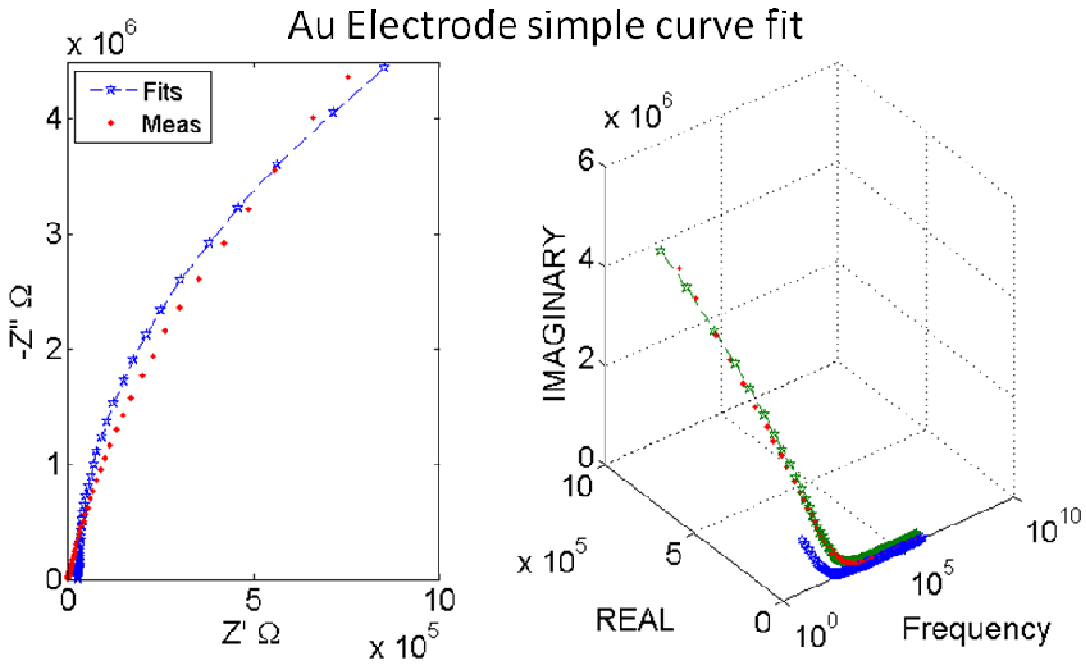

Figure 52: Nyquist and 3D plots of the curve fit results. In the left figure the blue line is the fitted result and the red dots are measured data. In the right plot, the blue line shows results using initial values and the green plot shows the final curve fit results.

Parameter	Value
Rt (Ohms)	1.73×10^{7}
C_I (Farad)	2.48×10^{-9}
Rs (Ohms)	31.44×10^{3}
Avg. Residual	44193

Table 4: Values of parameters used to fit the simple model to the measured data.

This then required me to look into more advanced models and further in electrochemical methods and modeling. The Warburg element is quite important as discussed in section 2.2.3. I then focused on the Randles’ circuit (with a Warburg element) which is considered to be the simplest model that provides a good interpretation of an electrochemical cell catering for both the double layer capacitance and the Faradaic components [54]. I have used a Warburg element model that assumes an infinite Nernst diffusion layer thickness. For far more accurate modeling we would require to consider the diffusion model in even more detail and consider even lower frequencies in our measurements. This was not possible with the time constraints and the equipment available to me at the time. As a figure of merit for the curve fit, I have taken the mean of the absolute value of the residuals at each point of frequency (with the weighting removed) and called this value ‘*Avg. Residual*’. The *Avg. Residual* of the new model for the gold electrode reduces by more than a factor of 25 when compared to the simple Randle’s

circuit used initially. The largest impedance value is 4.436×10^6 Ohms for the gold electrode (at 20 Hz) and the *Avg. Residual* using the new model is less than 0.04 percent of this impedance value. This allows me to assume that the new model used is sufficiently accurate for this analysis. The model used varied slightly from the original Randle's circuit as it had a frequency dependant double layer capacitance that is modeled mathematically as a constant phase element [86] as discussed in section 2.2.7 . It also provided the best curve fits as shown in Figure 53 and the Nyquist plot in Figure 54. This constant phase element behavior could rise due to surface roughness (more likely in PEDOT:PSS), distribution of reaction rates with the many chemical compounds present in HEPES saline, and non uniform current distribution paths as the electrodes are not directly facing each other [76, 85]. Thus once again, using CNLS curve fitting I found the values for the double layer capacitance 'Q' and 'n' (modeled as a constant phase element, where $C_{dl}=Q(j\omega)^{n-1}$ and $Z_{cpe} = 1/Q(j\omega)^n$), charge transfer resistance 'R_t', series resistance of the bulk solution and electrodes 'R_s' and the Warburg impedance coefficient 'A_w'. Eq. 22 shows the total impedance for the electrode, where ω is the angular frequency.

$$Z_{electrode} = R_s + \frac{1}{Q(j\omega)^n + \frac{1}{R_t + \frac{A_w}{\sqrt{\omega}} + \frac{A_w}{j\sqrt{\omega}}}} \qquad \textbf{Eq. 22}$$

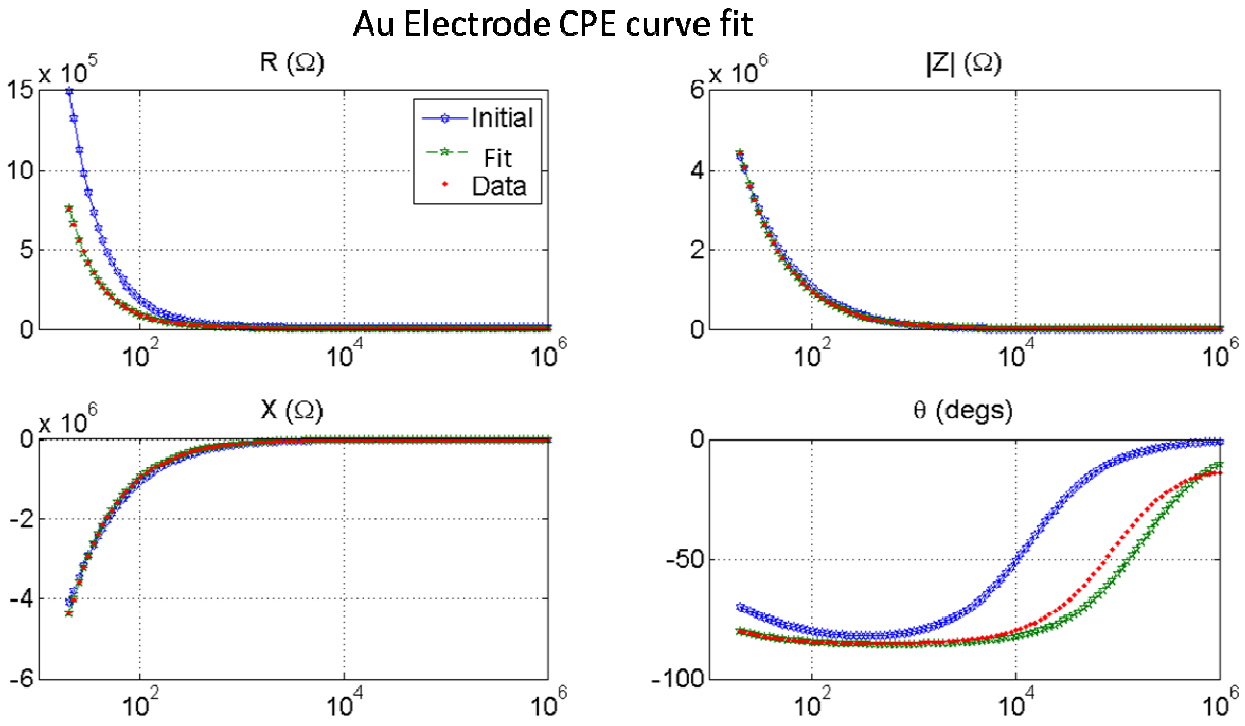

Figure 53: Plots of curve fitting results (Au electrode) using the Randle's circuit model with CPE to model the double layer behavior. The blue lines are the results using the initial parameters and the green plot in the final curve fit results to the data points (red dots).

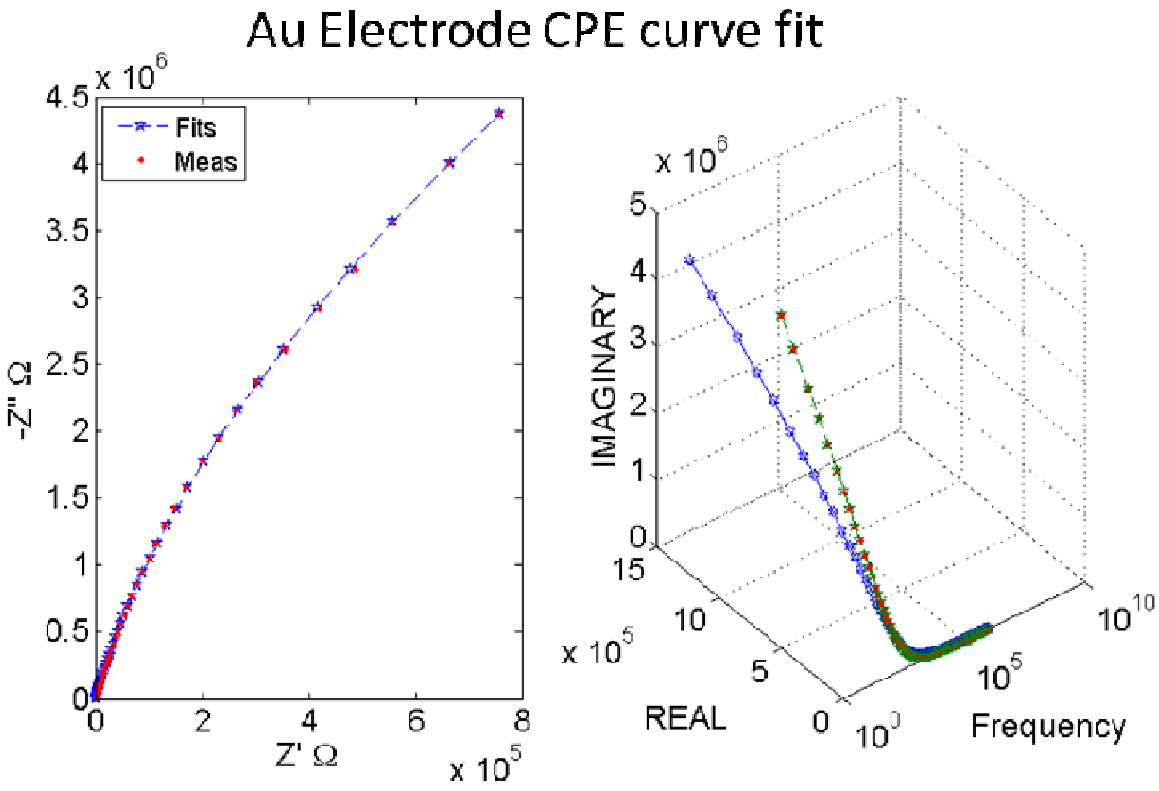

Figure 54: Nyquist and 3D plot of curve fit results (Au electrode) using Randle's circuit model with CPE. In the left figure the blue line is the fitted result and the red dots are measured data. In the right plot, the blue line shows results using initial values and the green plot shows the final curve fit results

Parameter	Value
Aw (Ohms)	9.41×10^{7}
Rt (Ohms)	3.16×10^{7}
Rs (Ohms)	0.78×10^{3}
Q ($S.s^n$)	2.12×10^{-9}
n	0.95
Avg. Residual	1737.6

Table 5: Values of parameters used to curve fit (Au electrode) using Randle's circuit with CPE.

The values (Table 5) of the curve fit to this model are quite interesting. The value of the charge transfer resistance is quite high. This shows relatively inert behavior of the noble metal in the particular electrolyte. The Warburg impedance coefficient is quite high as well. It may simply be reflecting high impedance in the Faradaic path. We must not forget that curve fitting is a mathematical process that can be erroneous and highly influences our interpretation of the results. From the Nyquist plots in Figure 54, we can see one red marker (data point of measured impedance) in between the 6×10^5 and 4×10^5 values

of Z` as a slight bend in the curve. This maybe a small error or beginning of the tail due to the Warburg impedance. It may require further analysis using different electrode dimensions and lower frequency measurements to elaborate the Warburg effect in order to precisely measure it. Considering these results to be within acceptable accuracy standards, we can however be confident that the Warburg impedance plays little part as there is very little charge transfer in any case. This kind of Nyquist plot and behavior is typical of noble metals [85, 125], even with larger electrodes.

The series resistance is quite low. The Au is roughly 50 nm thick and thus will show some resistivity (resistance of the electrodes calculated to approximately 15 Ohms, with resistivity assumed to $\rho=2.4x10^{-8}$ Ohms·m) and the rest can be attributed to the solution and geometrical spreading resistance. Another interesting value is that of *n* which is near 1. This shows a highly polarizable surface and behavior very close to that of an ideal capacitor. Again this is not unexpected for noble metals and the results give confidence in the model and the electrochemical analysis. Figure 55 shows the results of the curve fit to measured data for PEDOT:PSS electrodes with HEPES saline. Apart from the slight deviation at the higher frequency end, the majority of the fit is quite good. The high frequency bend in the measured impedance could be due to errors in the measurement or shows a behavior of PEDOT:PSS (such as inductive behavior due to length or low mobility of charges or even related to the flow of charges in the solution) that is not yet fully understood by me. This can be ignored as the important part of the curve fitting for electrochemical analysis is the lower frequency spectrum. Table 6 shows the values of the parameters found from the curve.

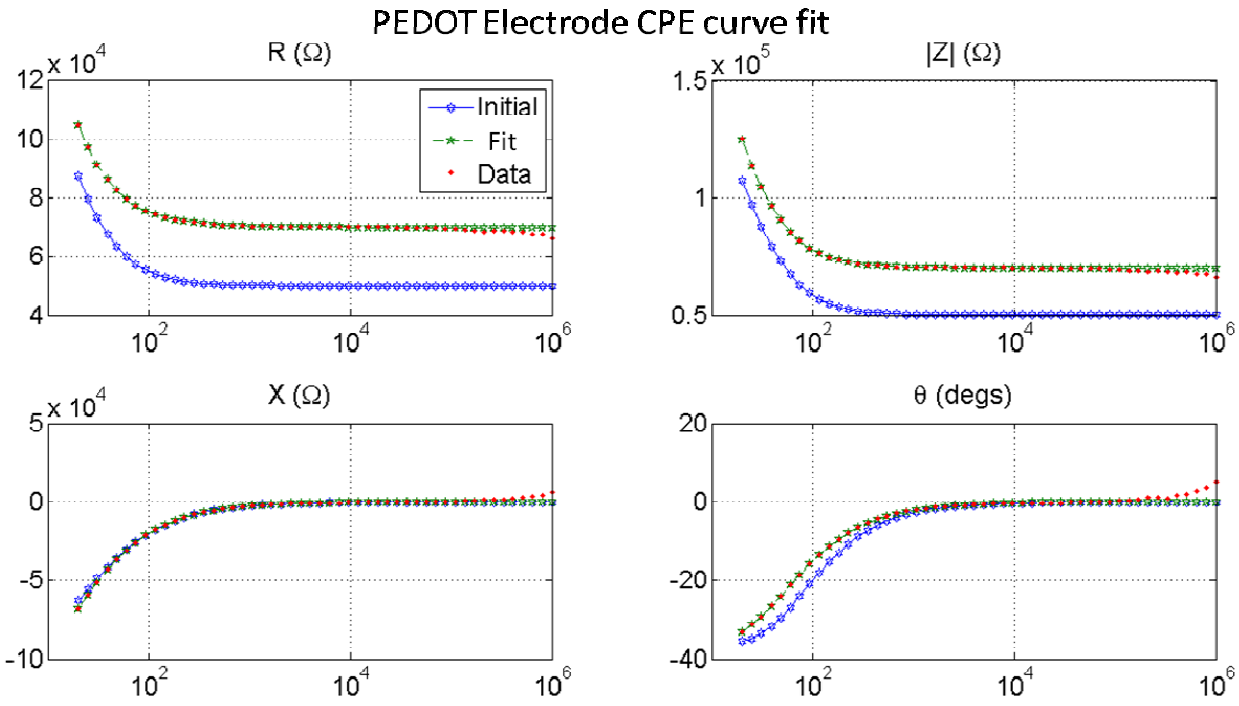

Figure 55: Curve fit results of PEDOT:PSS electrodes in HEPES saline. The blue lines are the results using the initial parameters and the green plot in the final curve fit results to the data points (red dots).

Parameter	Value
Aw (Ohms)	0.057×10^{7}
Rt (Ohms)	0.016×10^{7}
Rs (Ohms)	69.9×10^{3}
Q ($S.s^n$)	133.2×10^{-9}
n	0.907
Avg. Residual	934.8

Table 6: Values of parameters from the curve fitting results for PEDOT:PSS electrodes using Randle's circuit with CPE.

Figure 56 shows the comparison between absolute impedance |Z| values measured with HEPES saline using Au and PEDOT:PSS electrodes respectively. The table in Figure 57 shows the results per unit area of curve fit to the model shown in Figure 56. Two values for R_s are shown, one that is per unit area and the other which is the actual value. This is because in the case of PEDOT:PSS, the majority of the series resistance will be due to the electrode to connector length and not necessarily relevant to the understanding of the impedance model of the electrode or bulk of the solution. It can also be argued that due to the added resistivity of the PEDOT:PSS, the actual potential drop across the electrode-electrolyte interface is not the same anymore. However, given the fact that we are already in the linear region of the current and over-potential relationship, the charge transfer

resistance value will hold true even for smaller voltages. Also, given that the series resistance in the case of PEDOT:PSS is less than half the value of R_t, the potential drop across the interfacial impedance will still be larger than 10 mV and the difference between the two materials is still significantly large. Figure 56 shows the comparison between absolute impedance |Z| values measured with HEPES saline using Au and PEDOT:PSS electrodes respectively. The table in Figure 57 shows the results of curve fit to the model [85, 87] shown in Figure 56(mathematically represented in Eq. 22). The blue lines in the plots represent impedance predicted by the theoretical model using the results of the fit. Each frequency point is marked and the graphs show a tight fit to the measured impedance values (the red dots).The results show that the Au electrodes are more polarizable and have high values for the Faradaic impedance components of the circuit. PEDOT:PSS electrodes show low Faradaic impedance and a larger double layer capacitance with lower value of ‘*n*’, meaning that its characteristics are further from that of an ideal capacitor.

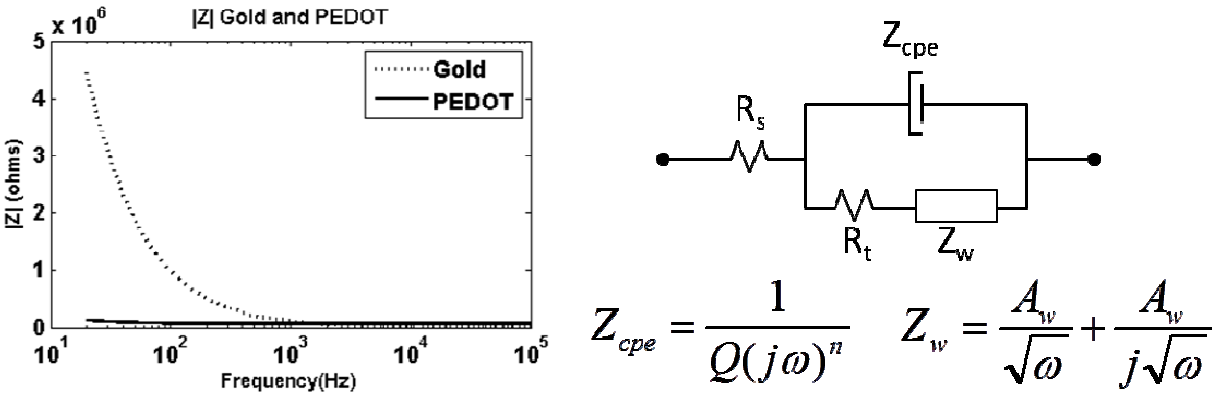

Figure 56: Absolute impedance (|Z|) results of PEDOT:PSS and Au electrodes (230 µm diameter) with HEPES saline solution and the interfacial impedance equivalent circuit model. Z_{cpe} is the impedance of the frequency dependant double layer capacitance (a constant phase element). Z_w is the Warburg impedance.

Bobacka *et al*. have shown that PEDOT:PSS has fast charge transport from electrode to the electrolyte and that the polymer has an excess of supporting electrolyte which provides good charge transfer capability. Hernandez-Labrado *et al*. have discussed diffusion of ions into the polymer layer due to its porous nature causing a frequency dependant Warburg behavior [120, 126]. The results here are in close agreement to those cases, however we must consider that the PEDOT:PSS layer here, since it has been spin coated, is not as porous or thick as what they have polymerized electrochemically in their experiments. The possibility of excess solvent in the PEDOT:PSS electrodes is also supported by the signs of adhesion loss after prolonged exposure to aqueous solvents

during our experiments. The requirements of CIS however, do not necessitate any further inquiry into this electrochemical research.

Element	Gold	PEDOT:PSS
|Z| @20Hz (MΩ)	4.436	0.125
Q (μS.s^n/cm^2)	5.1	320.8
n (dimensionless)	0.96	0.90
R_s (Ω.cm^2)	0.32	29.0
Actual R_s (kΩ)	0.7	70
R_t (kΩ.cm^2)	13.1	0.068
Aw (kΩ.s$^{-0.5}$.cm2)	39.1	0.239

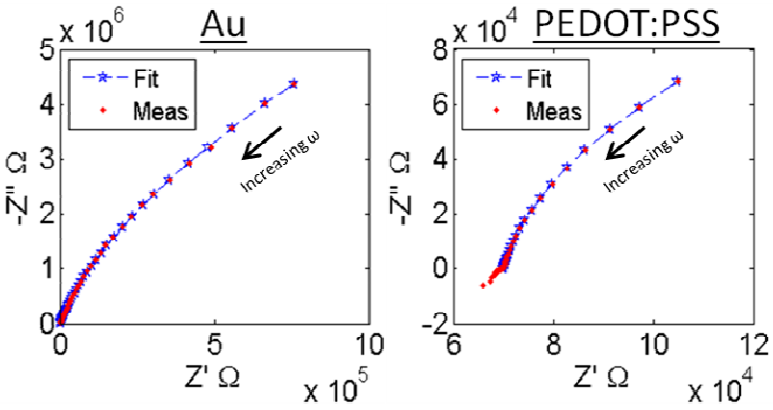

Figure 57: (Left) Table and (Right) Nyquist plots of curve fit results using the model shown in Figure 2 for the impedance of both types of electrodes. Z’ is the real value and Z’’ is the imaginary value of impedance (Z) measured from 20 Hz to 1 MHz.

Table 7 shows results collected from three different theses. The work D. Borkhold provide some calculated values and those from R. Tang are a range of maximum to minimum values measured for his Flex MEA device electrodes made using platinum. We can see how the results for the FlexMEA’s vary so much. One thing to mention here is that the models used are similar but not the same. While most have used the basic Randle’s circuit, the results from my work consider CPE’s for the interfacial electrodes which provide better curve fits if compared to those in R. Tang’s work, once again emphasizing the importance of the element itself. While values can be calculated they may not be as accurate as one may think. As discussed earlier the models for electrodes are by no means a complete description for what occurs at the electrode interface. It is also hard to create similarities amongst electrodes and their values when the design and experimental parameters such as quality of the metal deposition, distance from reference and shape etc can change the overall results. The table however does show that vast difference between all those metal based electrodes and the PEDOT:PSS electrodes.

Element	Gold Measured	PEDOT Measured	Pt-bare Calculated (Borkhold)	R. Tang Measured FlexMEAs Pt-bare
Ci (nF)	2.12	133.3	--	2-0.5
Ci ($pF/\mu m^2$)	0.05	3.2	0.7	--
Rt ($M\Omega$)	31.6	0.16	--	254- 0.97
Rt ($G\Omega \cdot \mu m^2$)	1.313	0.006	3.3	--

Table 7: Results comparison with those from Theses by D. A. Borhold [79] (both for 154mMolar NaCl solution) and R. Tang [127] (100mMolar NaCl solution). The values of C_I for my results shown in Gold measured and PEDOT measured are taken from Q assuming it can be considered as the interfacial capacitance. R. Tang’s results show large variations even for a similar design but separate electrodes.

5.3 Effects Due To Over Heating PEDOT:PSS

If the PEDOT:PSS based devices were baked at high temperatures in order to better cure the SU-8, they were prone to degradation and showed anomalous behavior over the frequency spectrum. Hence results from control wells of three different experiments were looked at. The devices in each case had a different final bake during their fabrication. These baking temperatures were 120 °C, 150 °C and 170 °C. Figure 58 shows the results of an MDCK experiment done using a device that was baked at 170°C for almost an hour before processing for cell seeding. In this experiment wells 1 and 2 were the control wells and the rest had similar number of MDCK cells seeded in them. The impedance spectrum of the control well (well1) shows how the impedance at higher frequencies has increased above that of the lower frequencies making it behave unlike a parallel RC circuit or a Randle’s circuit. The impedance measurements over time show how the impedance is constantly increasing for all wells over time and there are large fluctuations at the points of media change and even when just removed for microscopy, meaning temperature variation is just as significant. The overall absolute impedance values of the electrodes have also increased for a typical PEDOT:PSS device with a window diameter of 500 µm.

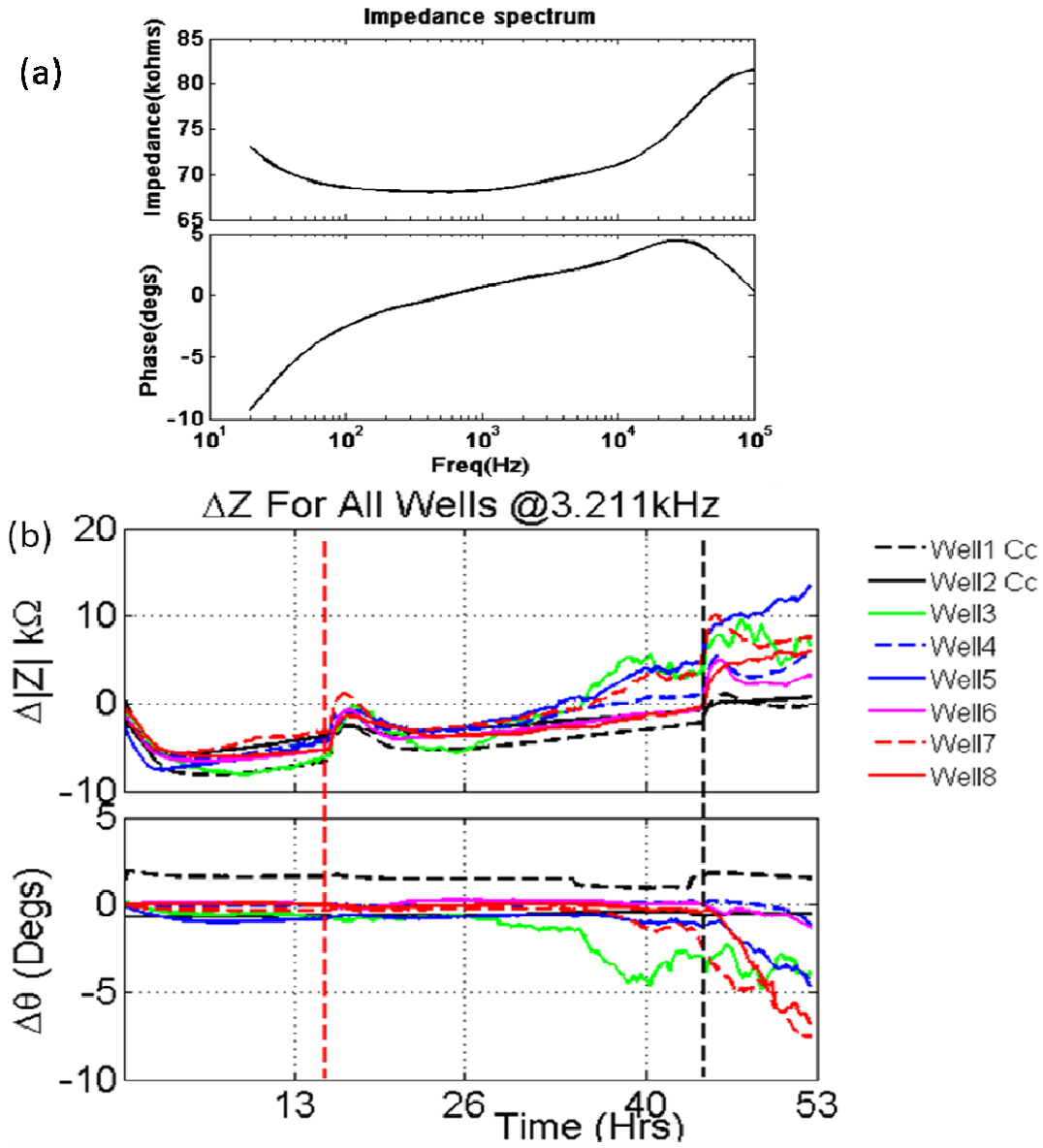

Figure 58: PEDOT:PSS device heated to 170deg for 1 hour to bake SU-8. (a) Impedance Spectrum of the control well1 at 0 hrs. (b)The results of the MDCK experiment shows how impedance instability increases. Red vertical lines shows media change, black vertical line shows device removed only for microscopy (hence variation in temperature, time delay and disturbance of the solution all affect the measurements at this point).

These results were some of the last few experiments done and it is possible that are affected by the PEDOT:PSS solution passing its expiry date (12 months as specified by the manufacturer). Figure 59 shows plots of changes in the control wells (no cells). The plots were taken from four experiments of different types of devices. Three of the devices were PEDOT:PSS electrode devices and one was from a Au electrode device. Since the time points where media is changed is not consistent, the large spikes occur at different time points. One of the devices was a Au electrode device, the others were using PEDOT:PSS electrodes with different final baking recipes. Measurements from two frequencies are

shown. The Au electrode shows large but consistent variation at 40 Hz but almost no observable change at 4 kHz. The PEDOT:PSS device with a final bake for 10 min at 120°C shows very little change and settles down very fast when there is a change in the media. The device baked at 150°C has more variation in comparison to the 120°C baked device, with spikes of roughly 2.5 kΩ. The last device which was baked for much longer and at a higher temperature shows spikes as large as those shown by the Au devices and at both low and high frequencies. It also shows constantly increasing impedance after the first initial drop, which is opposite to the Au behavior.

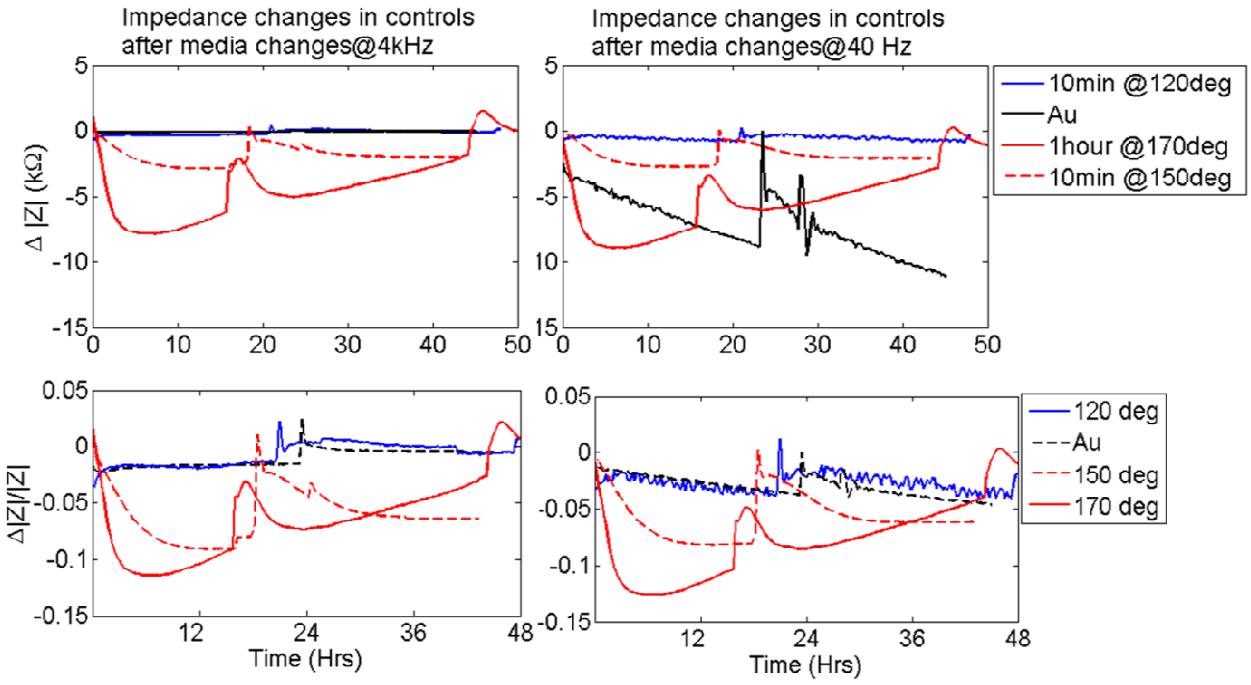

Figure 59: |Z| changing when media is changed. The data was collected from the control wells of different experiments of known devices, thus the time points of media changes varies for each device, but the sudden (almost vertical) changes in the values are the points where the media was changed for the specific device. Bottom two graphs show the normalized graphs (with reference to the first measurement at 0hrs).

There is a clear relationship with this instability and the fabrication process. Table 8 provides values of the absolute impedance (|Z|) at the two frequencies. The instability as seen in Figure 59, increases for the device (at that frequency) which has a higher |Z|. This holds for the Au electrode device as well. Figure 60 shows the impedance spectrum of the three PEDOT:PSS devices. We can see that the device baked at higher temperatures have higher impedance over all frequencies. The device baked at 170°C for 1hr (used in Figure 58) shows far higher impedance than the other two devices and also abnormality in the curve shape at higher frequencies. This may be due to degradation of the conducting polymer backbone, or the morphology of the film layer changing (PSS moving to the top

of the film, hole formation in the polymer layer etc). In all cases, we can see that the change is a shift up of the curve, showing an increment in the series resistance (R_s). Another thing is that the changes during impedance measurement over time are larger for the devices with higher base impedance (that is the initial impedance at that frequency). Now Au electrode also show larger variation at frequencies where the base impedance is higher. It could be that this behavior is more to do with the base impedance then the chemical structure of the PEDOT:PSS devices itself.

Device	|Z| kΩ @ 40Hz	|Z| kΩ @ 4kHz
PEDOT:PSS 10min@120°C	23.65	21.29
PEDOT 10min@150°C	33.79	31.56
PEDOT 1hr@170°C	70.48	68.45
Au	237.5	4.786

Table 8: |Z| values for the devices at 40 Hz and 4 kHz.

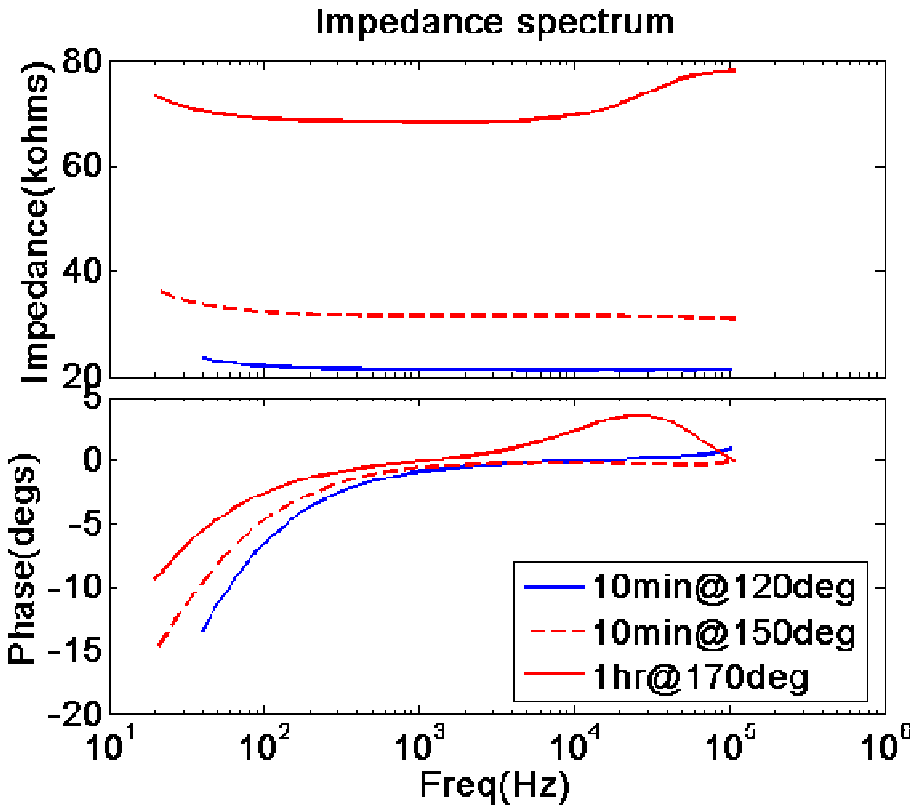

Figure 60: Impedance spectrum of all three PEDOT:PSS devices (control well1). All measurements are from the beginning of the experiments.

Parameter	120 °C	150 °C	170 °C
Aw (Ohms)	$220x10^{3}$	$162x10^{3}$	$133.38x10^{3}$
Rt (Ohms)	$30.5x10^{3}$	$9.88x10^{3}$	$29.38x10^{3}$
Rs (Ohms)	$19.3x10^{3}$	$31.4x10^{3}$	$68.6x10^{3}$
Q ($S.s^{n}$)	$1131x10^{-9}$	$715x10^{-9}$	$559x10^{-9}$
n	0.89	0.95	1
Avg. Residual	51.04	105.6471	4560

Table 9: Curve fitting results for the three devices at the beginning of the experiments. Avg. Residual values show the devices are becoming diffcult to fit to the same model for higher baking temperatures.

Table 9 shows the curve fit results for the three PEDOT:PSS devices. The data to which the fitting was done was taken from the first measurement (shown in Figure 60) of the experiment. The Avg. Residual is higher for the two devices that were baked at 150 °C and 170 °C. For the device baked at 170 °C, the fitting is worse due to the odd trend after 10 kHz which is far from the model used. In the other two cases, the capacitance (*Q*) values are really high and in the case of the 120 °C device the curve fitting gives varying results depending on the initial parameters and restrains. Artifacts in the nyquist plot suggests that the proteins in the solutions have an effect. Ideally these measurements should be done in a simple NaCl solution. The results show trend of increasing series resistance,increasing *n* value, and a decreasing capacitance for higher baking temperatures.

This limits the final bake temperature and time which can be problematic as the possibility of device failure due to Su-8 adhesion loss during an experiment increases. The adhesion loss could also be due to the Su-8 being expired or old, however a final bake above 150°C will alleviate the problem significantly. It may be the Su-8 adhesion to glass itself or it could possibly be due to PEDOT:PSS absorbing lesser quantities of water.

Chapter 6: **MDCK Experiments**

6.1 **Cell Growth**

There are two things that need to be considered when cells are grown. One is that when the cells are seeded and successively grow, what is the difference in results when they grow over the measuring electrode alone and when they grow over the entire well? Secondly what kind of a difference does it make between simply adhered cells and those that make tight confluent layers. In order to do this I began my experiments by containment of the cells on and around the measuring electrode. This was quite tricky and after some well design changes (used square wells instead of round) and the use of Ibidi cell culture inserts, cell death was avoided. The experiments were performed in an incubator set to 37ºC with a 5% carbon dioxide environment. For all cell experiments the first steps were to rinse them with a 70% ethanol solution followed by a rinse with HEPES saline and the then the media that was to be used. If there was a need for a poly-L-lysine (PLL) coating (or anything else) this was done after the HEPES saline rinse. If culture inserts were to be used, it was important to let the surface dry out to allow the inserts to stick to the surface, and then all the compartments rinsed with the media to remove any excess salts.

The first set of results that will be discussed were done using the second generation devices. MDCK cells were seeded for 24 hrs using culture inserts placed in such a way that the reference electrodes were kept out of the culture chamber of the inset. This allowed seeding of cells directly on and around the working electrodes. The inserts were then removed and the measurements over time were started. The media used was DMEM and a PLL coating was applied. Figure 61 shows the cells at the start of the measurements. At this point there were very few cells on the edge of the reference electrode. The experiment was performed over 5 days, Figure 62 shows the results.

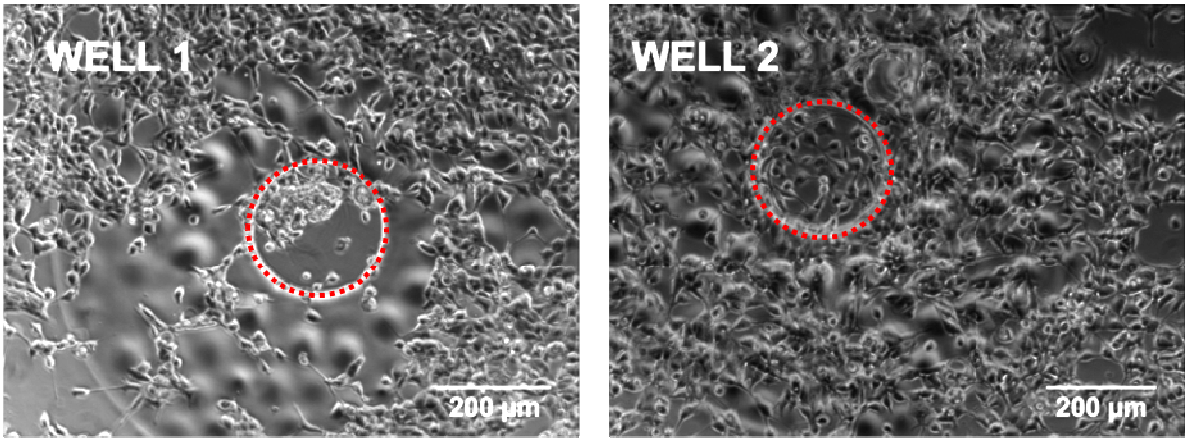

Figure 61: Well 1 and 2 measuring electrodes, 24 hrs after cell seeding. The red circles show the boundary of the working electrode and all the area outside those circles is covered with SU-8.

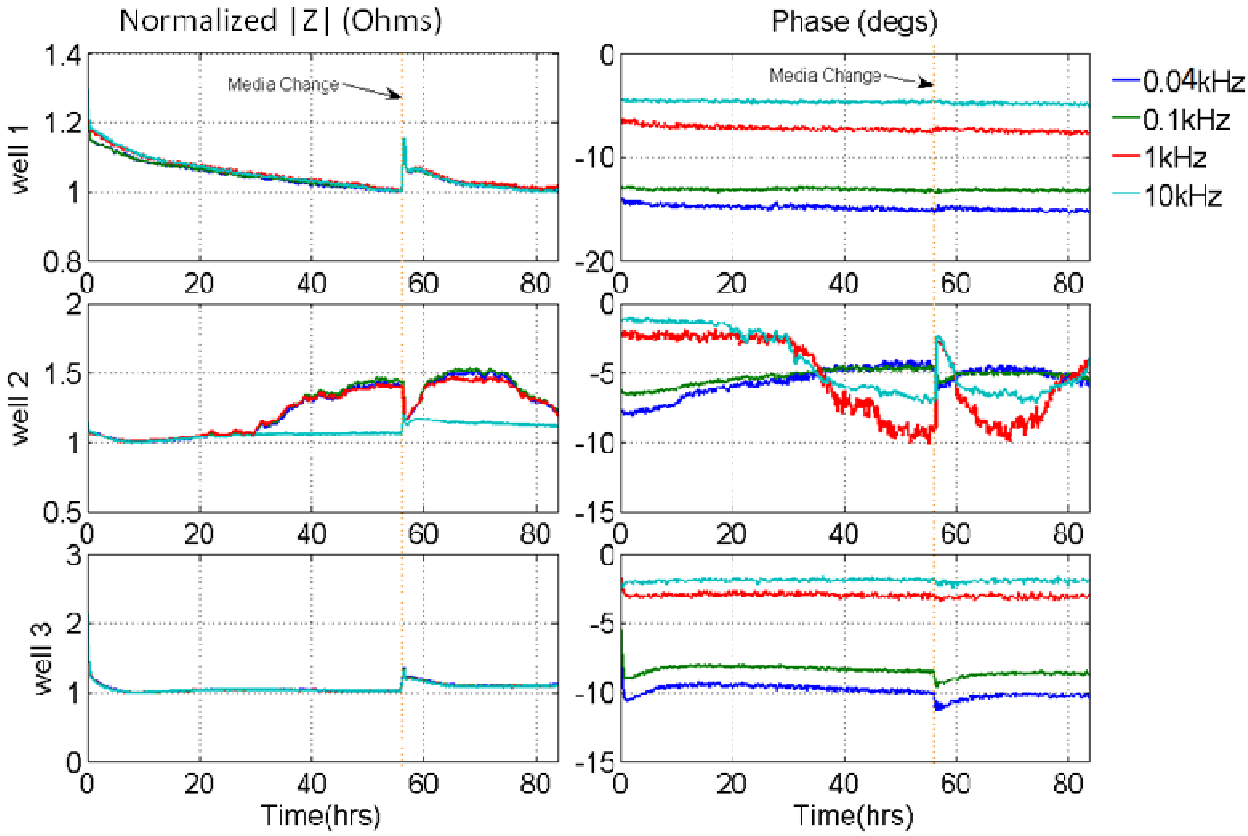

Figure 62: Results of an MDCK experiment using the 2nd generation devices and culture inserts. The |Z| values are normalized to the initial impedance and phase values of electrodes without cells. Well 1 was seeded with MDCK at 0 hrs but the cells failed to cover the electrode completely. Well 2 also had MDCK's seeded and well 3 was the control.

Well1 and the control well (Well3) show sudden rise and fall in the |Z| at approximately 56 hrs. This change corresponds to the change in the media and the initial

temperature variation of the media. Even though the media was pre-warmed, the time between seeding and starting the experiments is not short enough to keep the media temperature from dropping from 37 °C. Well1 however does not show much about the cell growth and has failed as for some reason the cells never covered the working electrode surface very well. Well2 shows a change after almost 30 hrs. At 56.3 hrs, again there is a very odd variation which corresponds to the media change. However instead of |Z| having a rapid rise and an exponential fall, it nearly reaches the initial values of |Z| near 200 kohms and then rises once more back to above 250 kohms at 60 hrs, approximately taking 4 hrs to return to the values before the media change. Further on, |Z| and phase then seem to be changing in a fashion similar to before the media change, as if to show that if the media change was not done it would have continued on without abnormalities. One explanation here would be that when the device was taken out for a media change, the cells were exposed to a change in temperature by more than 10ºC (room temperature was 22ºC) which could have been adverse. Another possibility is that the media change was turbulent. Perhaps this caused the cells to react by reducing their tight adhesion to the surface if not totally loosing it. The media change and microscopy took around 5-10mins and the device was placed back in and measurement started once more. After those 4 hrs the growth has returned back to normal. Figure 63 shows the cell growth over the measuring electrodes and the center of the wells. Cell density is extremely high over and around the measuring electrodes but sparse over the edges of the reference electrode. The difference between Well1 and Well2 is that the cells have not completely spread and covered the measuring electrode of Well1 as they have in Well2. The cells do not seem to have made a healthy looking confluent layer either over the measuring electrode. It might explain why the impedance measurements of Well1 do not show much change.

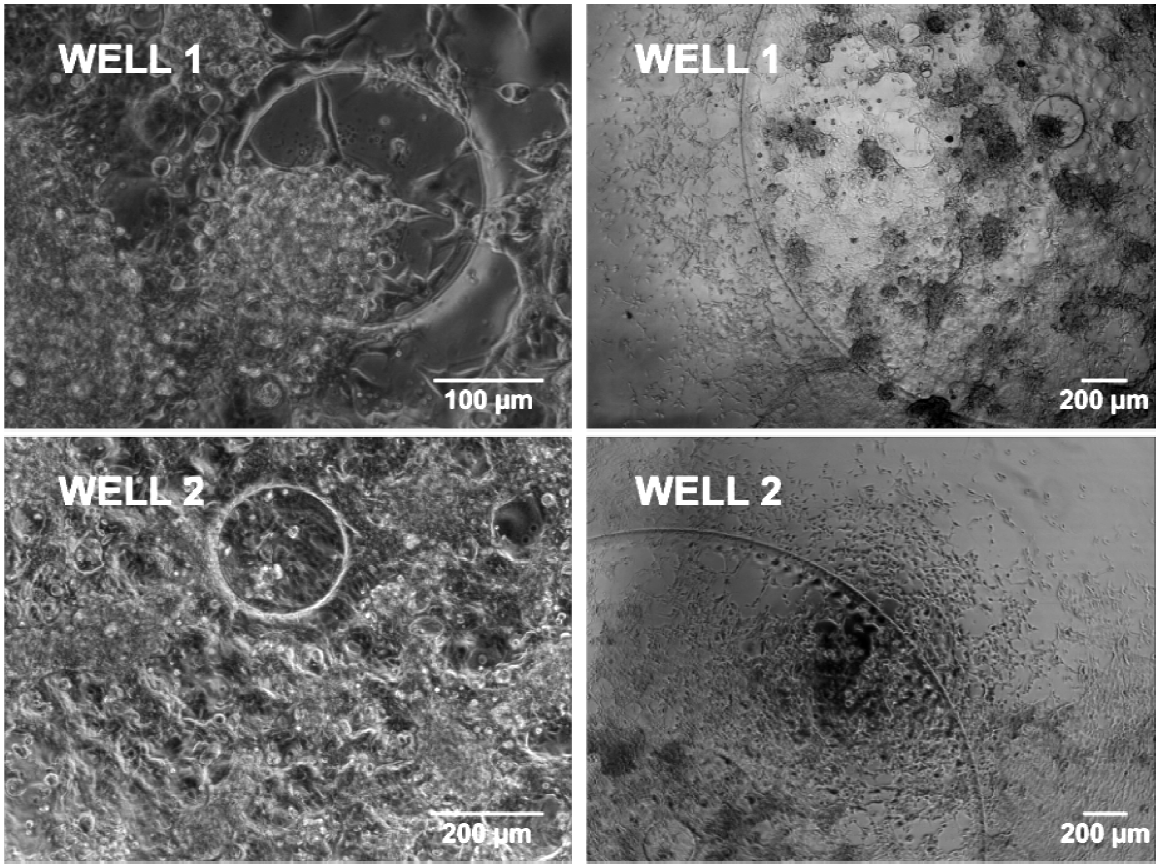

Figure 63: Cell growth after 3days

Then we need to consider why in Well2 does |Z| begin falling after 73 hrs. At the end of these measurements, the media was removed and the wells were rinsed with HS using 0.5 mL of HS. Figure 64 shows the results of the rinse. The cells were initially seeded on the right side area of this picture. They grew most confluent thereafter and made a tight epithelial monolayer which lost adhesion to the substate. Eventually the cells would have lost adhesion to the surface as the light rinse was enough to displace them and they were floating in the media as can be seen by the darker patch in the middle of the picture. Interestingly the cells that are still growing over the reference electrode are not at the same stage as the cells that have lost adhesion. They continue to grow and are still attached to the surface and the tissue which thus is floating but attached on one end to the reference electrode.

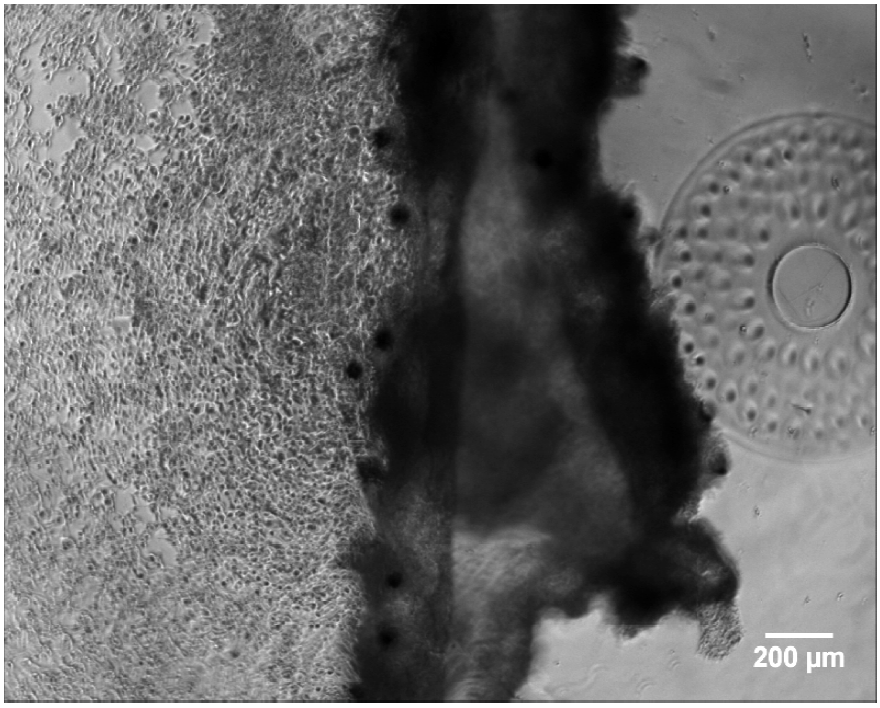

Figure 64: Well2 after rinsing with HS. Reference electrode is in the left half of the picture and has cells adhered to it.

The results show that cell growth over the reference electrode is not as important as the need for a tight confluent layer still attached to the measuring electrode in order to see relatively large observable changes in |Z|. Looking at the control well we can see that variation in phase due to media change is only prominent over all frequencies by a similar factor (remember these results are normalized). These variations due to media changes are discussed in section 5.3.

I also fabricated interdigitated electrode devices and did experiments using MDCK's with them. Some pictures of the experiment are shown in Figure 65. The PEDOT:PSS strips can be seen as shades of gray lines. While these devices are good to measure changes over the entire well, it is harder to relate the electrical changes to the optical observations as there is too much area that is relevant. The electrical changes are also smaller per cell as the overall electrode area becomes rather large. Due to this I returned to using the single measuring electrode device.

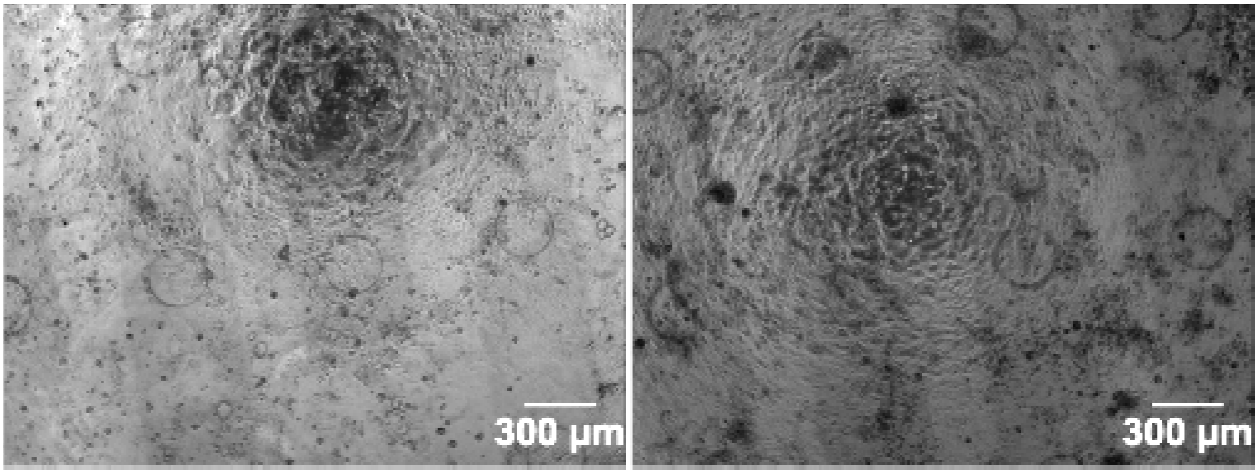

Figure 65: Point 4, day 7 pictures of both wells(Well1 left, Well2 right).

To investigate the comparison experiments of MDCK proliferation when using Au and PEDOT:PSS electrodes, the 3rd generation devices were used. The electrodes for these experiments had an approximate area of $2x10^{-3}$ cm^2, that is a 500 µm diameter window. Figure 66 shows results of the CIS setup measuring all 8 wells using PEDOT:PSS and Au electrodes. Well 1 and 2 (both black lines) are control wells in each case and the rest of the wells were seeded with approximately 8×10^5 cells. The results show real time impedance changes due to the cell coverage on the electrode surface. The plots show the difference from the initial impedance values, that is $\Delta|Z|$ and $\Delta\theta$ (phase angle). Initially the cells begin attachment to the substrate and start covering the electrode which causes a considerable change in the phase but the total change to $\Delta|Z|$ does not look significant. This behavior can be attributed to a more capacitive effect as cell coverage acts like a capacitor. After approximately 20 hrs (23 hrs for Au electrode results), the cell growth increases and cells begin to achieve confluence which causes $\Delta|Z|$ to increase as the cell-cell junctions restrict the current flow and cause higher resistance in the path. In the case of PEDOT:PSS the phase changes due the cells, at this frequency, is increasingly negative where as the experiment with Au electrodes shows increasingly positive phase changes. This is a rather interesting variation. $\Delta|Z|$ for both devices are constantly decreasing initially and show sudden changes right after media is change. The change after the media is changed, has a trend similar to that observed at the start of the experiment. This could mean it is related to chemical changes in the media over time. This could be due to pH/chemical changes (due to buffer etc) over time. Judging from observation of the control wells, it is likely to be due to changes in

concentration of dissolved CO_2.

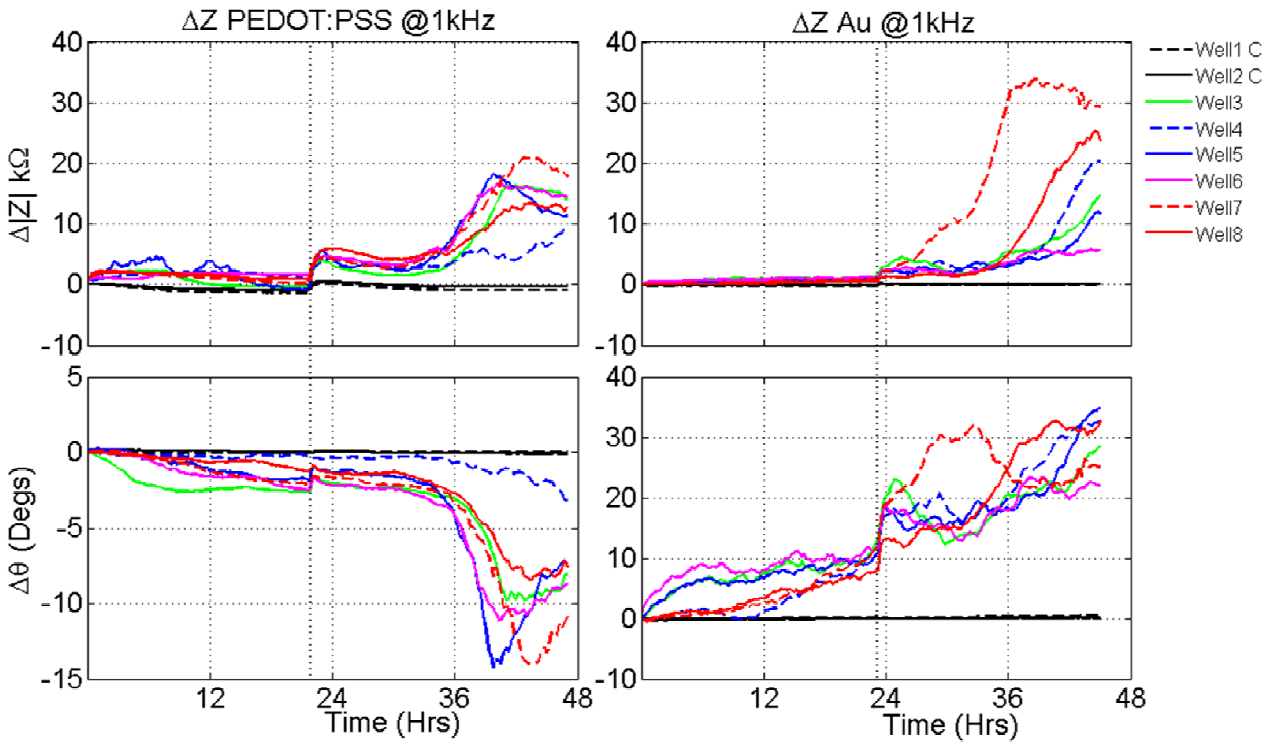

Figure 66: Results of MDCK experiments using PEDOT:PSS and Au electrodes. Data at 1 kHz of all 8-wells is presented. Values shown are the changes from measurement taken at 0 hrs. The black vertical line shows the time point where media was changed. Wells 1 and 2 are the controls (marked C).

Figure 67 shows results of experiments where cells were seeded in a region above the working electrodes using cell culture inserts (Figure 67, bottom). After allowing the cells to settle, spread and migrate for 24 hrs, the inserts were removed and the measurements were started. This allows us to measure cell coverage of an electrode by the means of migration in a particular direction instead of proliferation over the entire well, somewhat similar to a wound healing experiment. It also insures that there is no contribution to the impedance measurements due to cell growth on the reference electrode. Media was changed each day and the micrographs marked (a-d) were taken at the specified time points. The experiments were stopped when the cell confluence was observed by optical microscopy inspection. The inserts were not placed at precisely the same distances from the working electrode, thus the times for the seeded cells growing and reaching the electrodes are not exactly equal for both the experiments. The observed changes in the measured impedance for both electrode systems correspond to the cells covering the electrode area. Changing the media every 24 hrs reduced the effects of variation in pH. However, each time media was changed (indicated by the vertical dotted lines), the electrochemical balance of the electrode was momentarily affected. PEDOT:PSS

electrodes recovered faster from these effects (as seen in Figure 67) than Au electrodes. This is most probably due to the fast charge transfer at the electrode interface. At lower frequencies the electrochemical variations affect Au electrodes more than what is observed with the PEDOT:PSS electrodes and can reduce the reliability of the measurements but could be alleviated by continuously pumping fresh media.

Results of Figure 67 (a) show, that after approximately 30 hrs we find that the real part of the impedance at the lower frequency (40 Hz) keep increasing but the phase part settles. This shows that at these frequencies the change is mostly resistive. At higher frequencies the real part settles but the phase part keeps changing which indicates a reactive behavior. The variation of changes in impedance at the two frequencies shows how they are sensitive to different facets of the impedance due to cell growth.

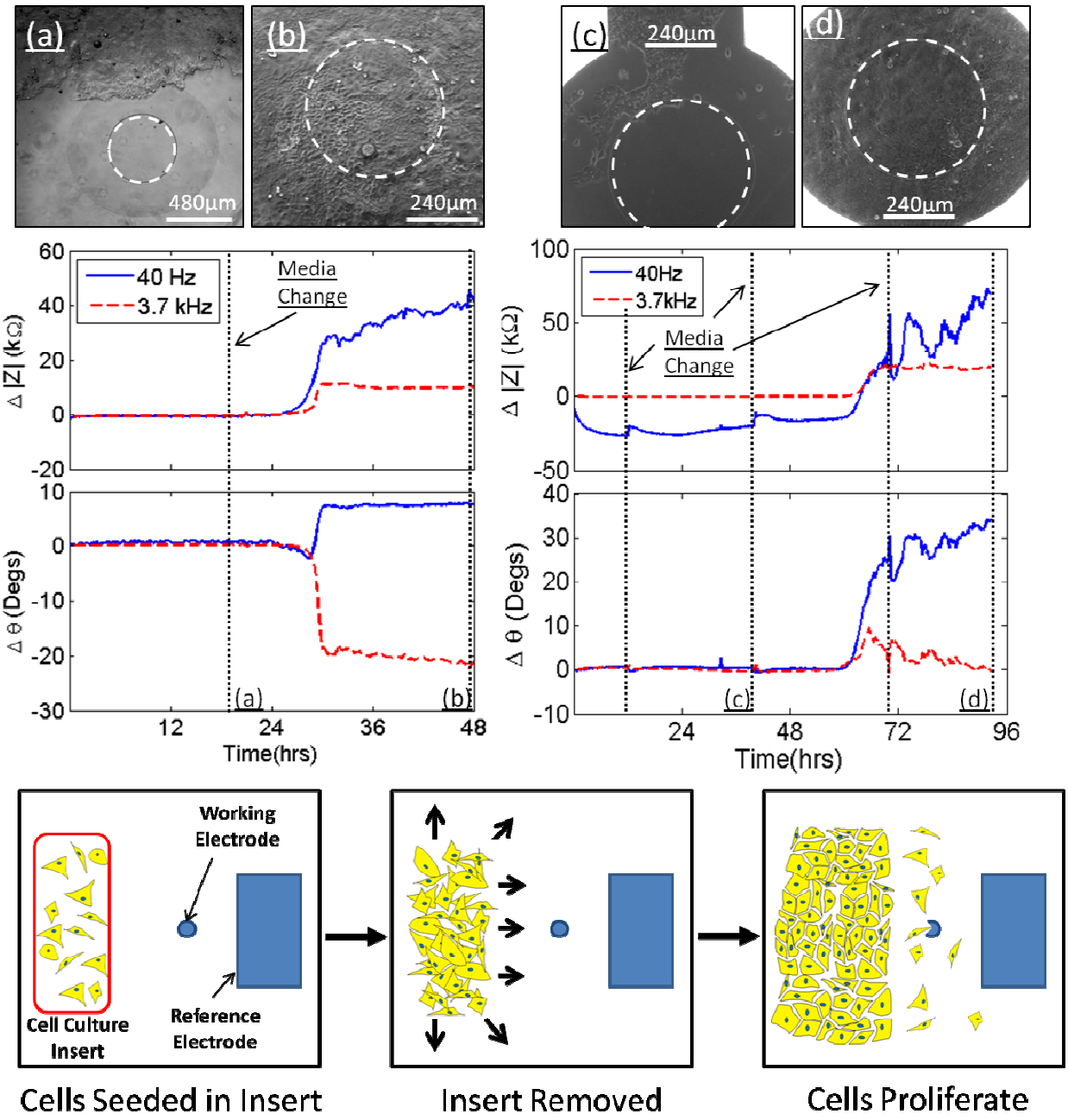

Figure 67: Results of MDCK using PEDOT:PSS electrodes (Left, where (a) is the start and (b) shows pictures of the well at the end) and Au electrodes (Right, (c) and (d) show pictures at the start and the end respectively). The graphs are the differences in absolute impedance |Z| and the phase Θ from the initial values. The electrode windows in the SU-8 are indicated by the white rings and the dotted black vertical lines show when the media was changed. Bottom diagram shows how the culture insert is placed at a distance from the electrodes and cells are seeded inside that insert. Once the cells have adhered to the surface the insert can be removed to allow the cells to grow in an outward direction. The cells will eventually start covering the working electrode and reach confluence.

6.2 Cell Impedance Modeling

Figure 68 (a) shows how the impedance spectrum changed due to cell coverage in the PEDOT:PSS electrode experiment shown in Figure 67. The impedance and phase values shown are not the actual values measured but the difference from the measurements taken after 1 hour of beginning the experiment. This helps to negate any changes due to initial electrochemical variations. By taking the difference from a time point where the electrodes have no cell coverage we assume that the impedance due to cells is in series to the electrode impedance electrical model. Y Qui *et al*. [10] have used a similar approach to measuring the cell-substrate distance for cardiomyocytes, where the cells were modeled by a simple resistor in parallel to a capacitor. The disadvantage of such an assumption is that the model is not valid for partial electrode coverage and holds true once the cells have covered the majority of the electrode. H. Xiaoqui *et al.* [97] have discussed a model that considers the cell coverage of the electrode but their model does not consider the effects of phase changes. Our approach to this was to keep the model simple and use the theory of electrical elements similar to Y Qui *et al.* [10] but with a certain addition.

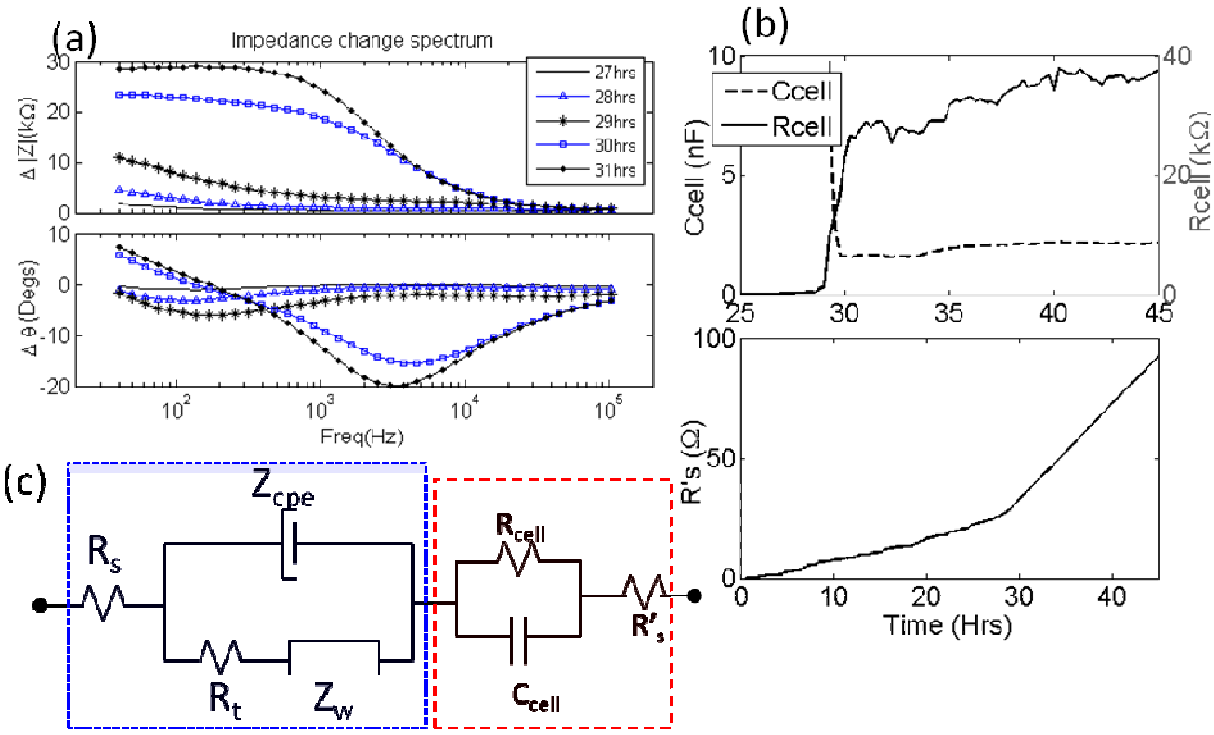

Figure 68: (a) Change in Impedance from a reference measurement (1 hr after starting the experiment) over the frequency spectrum. (b) Curve fit results for the cell model curve fit from 25 hrs onwards (when the model becomes valid) and also shows results for R's. (c) Biological cell electrical model (red) in series with the electrode impedance (blue).

Figure 68 (a) shows that at 31 hrs the Δ|Z| spectrum is similar to the impedance spectrum of a parallel resistor and capacitor circuit (RC circuit). However an inspection of the Δθ shows that the phase does not match a parallel RC circuit. Instead the results show a closer match to a resistor in parallel to a capacitor with both in series to another resistance, R'_s. This series resistance can be theoretically explained as a constriction of current in the small gap under the cell similar to that which Lo, Giaever and Keese have discussed [91]. R_{cell} can be attributed to the resistance to current flow between gaps of adjacent cells and C_{cell} is due to the capacitive effect of cells adhering to the surface. I have used this simple parallel RC circuit in series with a resistance to model the cell (as shown in Figure 68 (c) and mathematically in equations Eq. 23 and Eq. 24, and further analyze the results using curve fitting techniques similar to that applied for the electrode analysis in section Chapter 5: 5.2. The model for Z_{cell} was used to fit the measured change in impedance from after 1 hr of the experiment being started.

$$Z_{cell} = R'_s + \frac{1}{\frac{1}{R_{cell}} + (2\pi\omega C_{cell})} \quad \textbf{Eq. 23}$$

$$Z_{Total} = Z_{electrode} + Z_{cell} \quad \textbf{Eq. 24}$$

Figure 68 (b) shows the results of the curve fit for changes after 25 hrs. R'_s can be found directly as Δ|Z|at higher frequencies. This is because at higher frequencies the majority of the current will flow through C_{cell} which will provide the path of least impedance and thus the impedance seen at these frequencies is due to R'_s alone. We have then used this R'_s value in the curve fit for the cell model. Initially the parallel RC model does not exist as the cell coverage of the electrode does not exist or is not enough to have a significant effect on the curve fit. As the impedance increases, the curve fit results in values for R_{cell}, *which* follows changes in the impedance results shown in Figure 67 (a) for 40 Hz. Values for C_{cell} can be estimated at this point as well and after approximately 30 hrs the value of C_{cell} reaches a value around 2.5 nF and is very slowly increasing towards 3 nF. R'_s has a constant increase and at just before 30 hrs, it starts increasing with a faster rate once the cells begin covering the electrode. R_{cell} keeps increasing and this would show that the cell-cell gap is tightening (increasing confluency). This shows that once the electrode has been fully covered and the cells create a confluent layer, R_{cell} has a more significant contribution to the impedance changes. The increase in R_{cell} and R'_s can be portrayed as a decrease in cell-substrate distance [10, 94] and tighter confluent layers.

Now while the model comes close to predicting the cell behavior to a certain extent, it is important to know how accurate it really is. By measuring the impedance at higher frequencies and considering solely the dependency of on R'_s, we have improved the curve fit, however the lower frequencies are not as tight as for example, the curve fits of the electrode models. This is solely because a cell model would have to be far more complex than an RC circuit. Secondly the changes in the media and the electrode surface are likely to be included in the subtracted data. Figure 69 shows how the model's real part fits quite well but the imaginary part shows some very different shape to what would be expected from a RC circuit. The initial positive imaginary values are very interesting and difficult to explain. There has been work on cell impedance models for cell counting LoC devices. It would also be interesting to consider these and also adapt the different frequencies and digital signal processing techniques used in such devices [128].

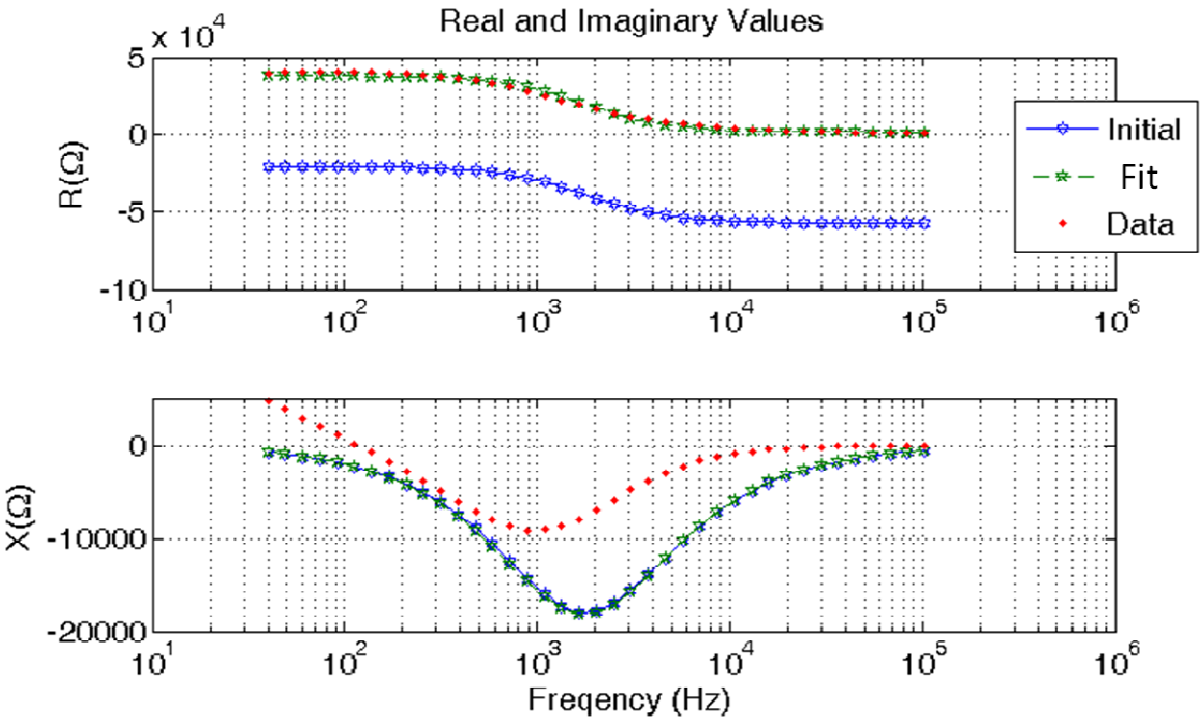

Figure 69: Curve fit of impedance changes to cell model, a single iteration for the results shown in Figure 68 (b).

6.2.1 *Comparison of Sensitivity*

The sensitivity of the system can be defined by Eq. 25 where $\Delta|Z|$ is the change in impedance due to cells. If $|Z|_{Electrode} >> \Delta|Z|$ then the sensitivity of the system is minute.

$$Sensitivity = 1 - \frac{|Z|_{Electrode}}{|Z|_{Electrode} + \Delta|Z|} \qquad \text{Eq. 25}$$

From the observations above we can assume a maximum $\Delta|Z|$ of 40 kOhms at 40 Hz. Assuming a single cell is a circular disk with radius 15µm (an area of approximately $7x10^{-6}$ cm^2) means that for an electrode with an area of approximately $2x10^{-3}$ cm^2, to be fully covered would require approximately 285 cells. Thus, every two cells contribute 280.7 Ohms to the change in impedance. For the experiments shown in Figure 5 the PEDOT:PSS electrodes have |Z| of 23 kOhms and the gold electrodes have |Z| of 170 kOhms at 40 Hz which can be considered as $|Z|_{electrode}$ for each case. Thus, for two cells covering the electrode the sensitivity would be 0.012 and 0.00164 respectively. This shows the improvement in sensitivity of PEDOT:PSS electrodes due to the significantly lower interfacial impedance which would also allow the impedance measurement instrument to work well above its SNR threshold at lower frequencies. The added improvement of reaching electrochemical stability faster than gold electrodes would also mean reduction in errors in the measured impedance. At higher frequencies (above 1 kHz) however, Au electrodes would be better as their |Z| due to the electrode would be lower.

The absolute impedance |Z| incorporates both the real and the imaginary components of the impedance. Phase (θ) is not an absolute value but a relative polar position that will repeat after its maximum of 360°. They can be compared by looking at the relative changes as a ratio of the maximum possible change of 360 degrees. From the values in Figure 70 (a), at 40Hz, we can see that maximum $\Delta\theta$ due to cell growth on PEDOT:PSS electrodes is approximately 8°, hence the ratio is approximately 0.02 and that on Au electrodes is 35° which give us a ratio of 0.097. Here Au has a phase change that is larger by a factor of 5. Considering the maximum value of the phase changes (at whichever frequency that may be) from both electrodes, that is a 25° change (0.069) for PEDOT:PSS electrodes and a 50° change (0.138) for Au electrodes shows that the latter have an improvement on the phase variation due to cell coverage by a factor of 2. The plots also show an interesting trend difference between the two electrode material. The Au electrodes show peaks in $\Delta|Z|$ and $\Delta\theta$ in the same regions of the frequency spectrum and have similar shape. PEDOT:PSS electrodes on the other hand have very different impedance change spectrums.

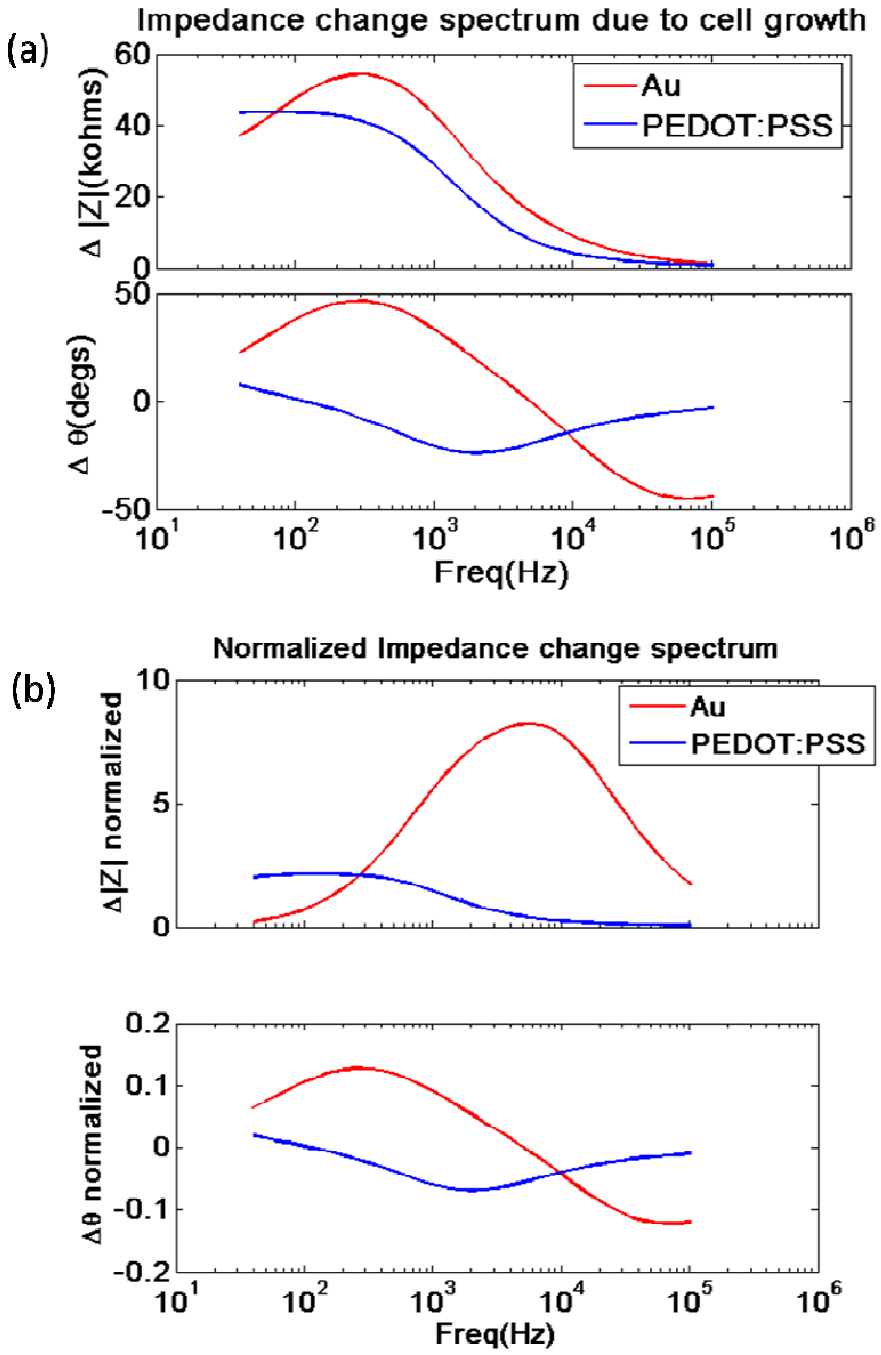

Figure 70: (a) Bode plots of changes in impedance due to cell growth. The changes shown are against reference measurements that is the measurements taken after 1 hr of starting the experiment. Values taken at times where the phase changes were maximum (at 48Hrs for PEDOT:PSS electrodes and 65Hrs for Au electrodes) in the experiment shown in Figure 67. (b) Plots of the same results but normalized ($\Delta Z/Z_{base}$ and $\Delta\Theta/\Theta_{base}$) to the impedance and phase values of the reference measurement.

Figure 70 (b) shows the normalized impedance changes. Here the impedance difference (for each frequency) was divided by the reference measurement (for that particular frequency) taken after 1 hr of starting the experiment, the same reference measurement used to find the impedance change. The gold electrode normalized Δ|Z| plot shows that the

peak is around 6 kHz. The PEDOT:PSS electrode normalized plots have the same shape owing to the more flat electrode impedance spectrum as shown in section 5.2.

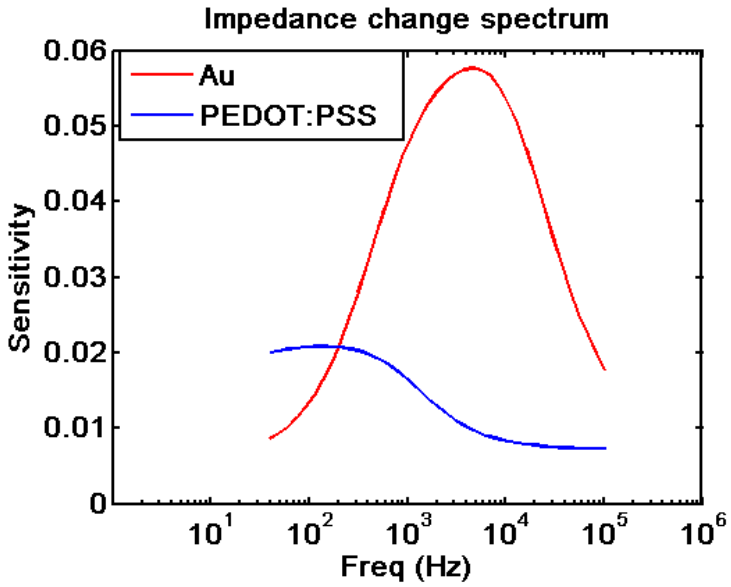

Figure 71: Sensitivity plotted for entire spectrum. Measurements used to calculate the sensitivity were taken from the time points where impedance change was highest in the respective experiment. Values for $Z_{electrode}$ were taken from the start of the experiment.

Figure 71 shows the sensitivity plotted for every frequency. The values were calculated assuming $\Delta|Z|$ for the equation was the change due to two cells covering each electrode. The measurements used to calculate impedance due to two cells were taken from the time points where the impedance at 40 Hz was highest, 48 hrs for PEDOT:PSS device and 84 hrs for Au device. Then sensitivity for each frequency was calculated accordingly. The has a similar trend to what we see in Figure 70 showing better sensitivity below 200 Hz for PEDOT:PSS devices but eventually with Au devices dominating the higher frequency spectrum. Both types of electrodes have their benefits at varying frequencies. PEDOT:PSS electrodes simply provide lower impedance at lower frequencies and the benefit of higher transparency.

Chapter 7: **Human Embryonic Stem Cell Experiments**

Since the advent of human embryonic stem cell (hESC) research, they have been the source of controversy and ethical debates regarding their source. However from a research point of view, their potential is enormous. Their ability to differentiate into any type of cell and almost infinite ability of self-renewal is extremely promising for curing diseases. While adult stem cells have similar abilities, albeit not of the same level, their extraction and maintenance *in vitro* remains a problem, especially for cells related to the nervous system. Recently there has been development of induced pluripotent stem cells (iPSCs). By enforced expression of particular transcription factors (such as OCT4), it is possible to reprogram somatic cells into pluripotent ones. While there is are many similarities to hESCs, including pluripotency and gene expressions, there are also many differences. Apart from that, iPSCs are still relatively new and there is need for more research before they can be utilized in therapeutic medical applications.[129-132]

While the ability of hESCs to differentiate into any form of cell is of great importance, maintenance of their pluripotency *in vitro* is difficult. Given the fact that they could have progressed into any of the germ layers also makes it difficult to distinguish cell types. It can become a difficult issue to researchers to maintain their cultures over long periods of time. While culture mediums have been devisied to help maintain pluripotency while allowing self-renewal and proliferation [133], the overall maintenance and constant screening of the cells is cumbersome. It would be extremely useful if there was a way to monitor cell differentiation using real-time, label-free and non-invasive techniques [134]. Cell impedance measurement techniques have been utilized to look at mesenchymal stem cell differentiation. [7, 8, 57]. We have used the CIS device setup described in this thesis to measure hESC differentiation and considered using a novel approach to distinguish between the two cell types.

7.1 Induced Stem Cell Differentiation Experiment

The experiments were performed in collaboration with the embryonic stem cell research group. Scott Cowan, who is a PhD candidate, performed all the cell culturing, media changes, staining, and fluorescent imaging of the cells. The device fabrication, experimental setup, measurements and data analysis were done by me. We choose to to differentiate hESCs to trophoblasts, which are the cells that create the outer layer of a blastocyst. While this may not be relevant to most current therapeutic research, it was ideal for us. This was due to the fact that the overall differentiation procedure is completed in approximately 72 hrs and the morphological differences between the two cell types are quite distinct and optically visible. The larger cell size of the trophoblasts (compared to pluripotent cells) would also provide significant difference in the impedance (capacitive and resistive) of the two cell types. Xu *et al*. [135] reported using bone morphogenic protein (BMP4) to induce hESCs to differentiate into trophoblasts.

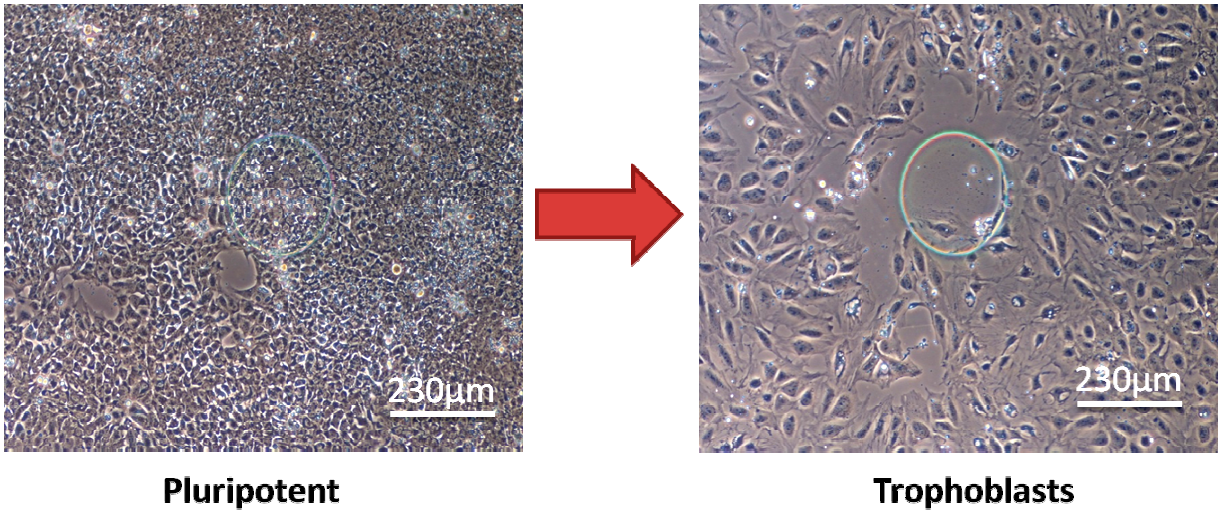

Figure 72: From pluripotent hESCs to trophoblasts. Note the larger size of the trophoblasts in comparison to the pluripotent stem cells.

Device Preparation:

The device, after fabrication is rinsed with ethanol and allowed to dry for an hour. It is then plasma cleaned in an O_2 plasma asher for 2mins at 120 W power. It is then coated with 0.3mg/ml fibronectin (MERCK), for 15 mins and then rinsed with PBS (-Ca/-Mg) (Invitrogen). This procedure is done just prior to cell seeding.

Cell Culture Day 1: Seeding of cells

Once at desired confluence (in petri dish), cells are given a 2 hour pre-treatment with 10uM of the Rho kinase inhibitor Y-27632 (ROCK inhibitor, Calbiochem) in Stempro complete media (DMEM F12+ glutamax (Gibco), Stempro SFM growth supplement (Gibco), 25% BSA (Gibco), 50mM mercaptoethanol (Gibco), 20 μg/ml bFGF (R&D Systems)). After 2 hrs, stempro is removed and cells washed with PBS (-Ca/-Mg). 1.5 ml of TrypLE select (Invitrogen) is added and cells returned to incubator to dissociate to single cell (2-5 min). 1.5 ml of Stempro is added to well to deactivate TrypLE select. At this point cells are titrated using 5 ml pipette to aid dissociation of cell clumps. Cells are counted, spun down at 1200 RPM for 3 min and re-suspended in stempro complete media and10uM Y27632. Cells are reseeded at a density of $5x10^4$ cells per well in stempro and 10uM Y27632.

Cell Culture Day 2-4: Induce Cells

Remove media from well and replace with MEF media (DMEM (invitrogen), 10% FCS (Invitrogen), 1x pen/strep/glutamine (Gibco)) and 10 ng/ml Recombinant human BMP4 (R&D systems). Return cells to incubator.

Cell Culture Day 5: End experiment

Remove media from well and wash 3x in PBS(-Ca/-Mg). Add 4% PFA (Parafarmaldehyde (Sigma)) to wells and leave for 20 min at room temperature. Wash further 3 times and store at 4 ^oC with some PBS for subsequent staining.

The first set of experiments were done using the second generation devices (Figure 27 section 3.2) and helped understand the differences between cells that were pluripotent and those that were in the process of differentiation, or had already differentiated to trophoblasts. The cells were first seeded on the device and the measurements were started once they had reached confluence or were close to do so. This would help distinguish changes due to cell growth and those due to differentiation. It is however not possible to curb growth and this is an ever present issue to consider during analysis. Once the cells reached a certain level of confluence that seemed appropriate enough, ROCK inhibitor

media was used in the well that will now be called the “Pluripotent well” and MEF media with BMP4, was used in the “Induced differentiation well” in which we wish the cells to differentiate. The control well had the media used for the induced differentiation wells but without cells.

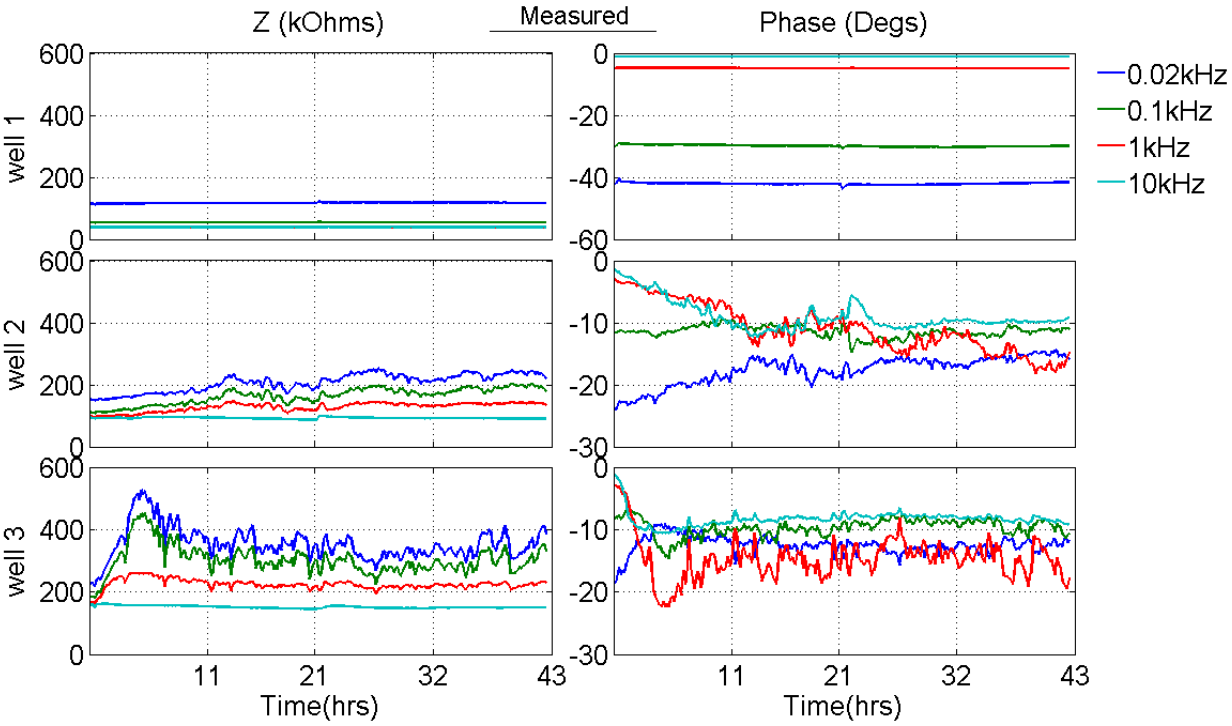

Figure 73: Results from the induced differentiation experiment, Well1 is the control, Well2 is the pluripotent well. Well 3 is the induced well. The values are the actual measured values, not normalized nor results of any subtraction.

One of the major differences we see are the large fluctuations in the values for the differentiation well (well3) in comparision to the pluripotent well (well2). This could possibly be attributed to the high activity and motility of cells during the biological changes or it could be their morphological variations. Larger sized cells (trophoblasts much larger than hESC) will cause more variation in the impedance with their motility. Well3 also shows rapid changes immediately after adding the inducing BMP4 media. At 43 hrs the absolute impedance values of the two wells varies however the phase seem very similar.

Experiments were then conducted thoroughly with the 8-well setup. Figure 74 shows the results of changes in impedance relative to the first measured impedance. The cells were seeded at 0 hrs and then induction media was introduced in wells 5-8 (marked D for differentiation). The pluripotent wells are wells 2-4 (marked P) and show smoother and slower increase in comparison to the differentiation wells, which themselves show the traits discussed for the results of Figure 73. The control (well1 marked Cc in legend) seems

to be quite stable other than the typical spikes right after the media changes associated to chemical and temperature variations. The values of the absolute impedance change (Δ|Z|) for the differentiation wells are larger in comparison to the pluripotent wells. In order to analyze this further, we will focus on two wells in particular, well 4 for pluripotent cells and well 6 for differentiation induced cells.

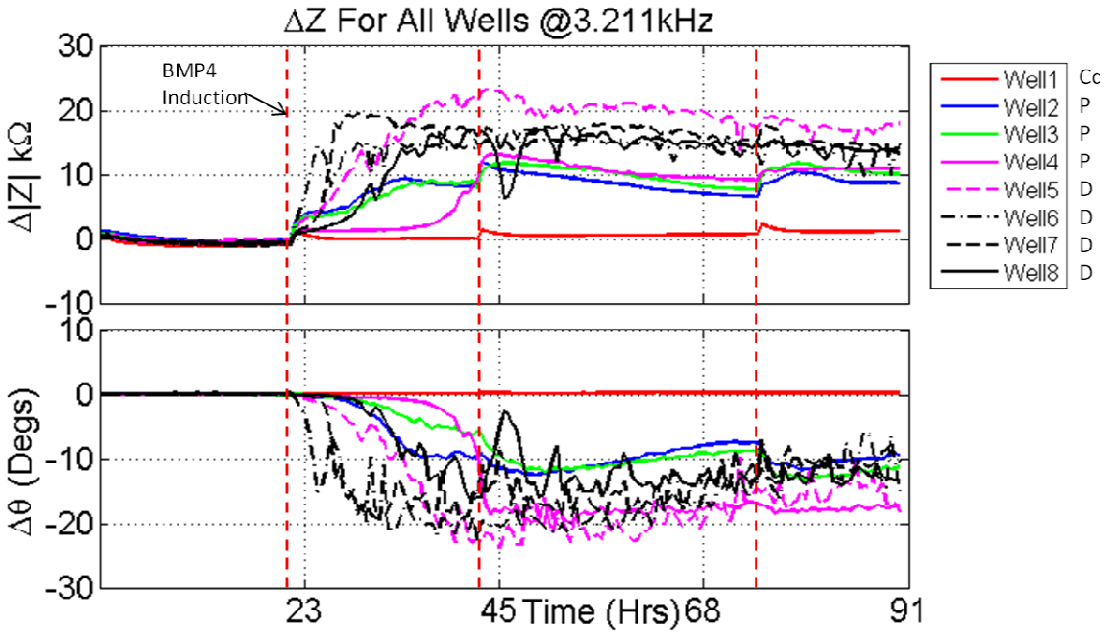

Figure 74: Results of stem cell induction experiments. Vertical red lines indicate points of media changes and microscopy. Cc is the control well (well1). The wells marked P (pluripotent) do not have any BMP4 added to them and those marked D (differentiation) have BMP4 added to the media at the time point marked (roughly 22 hrs).

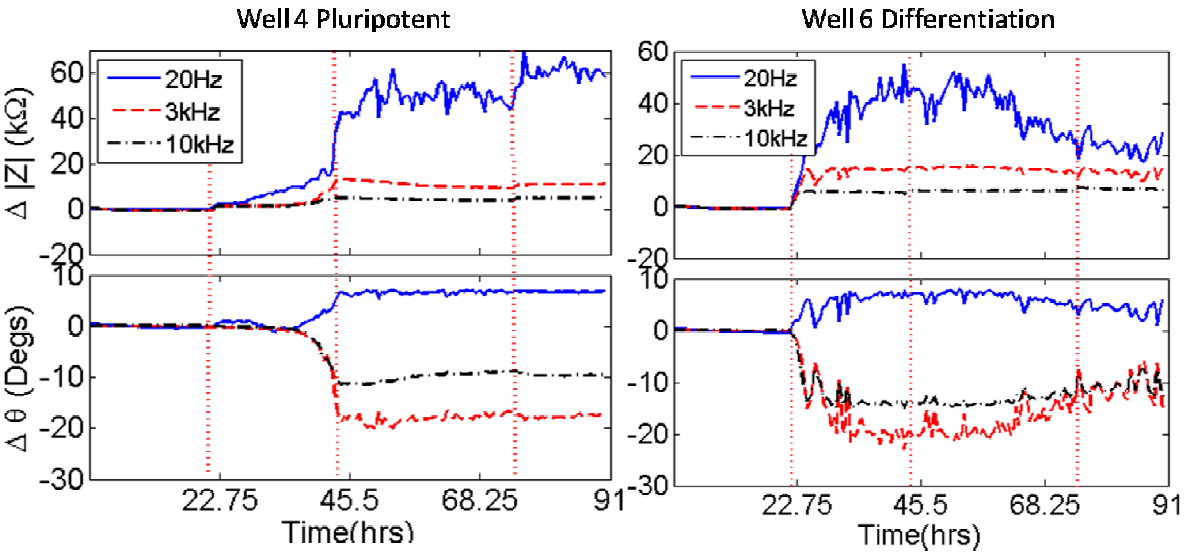

Figure 75: Impedance changes for a pluripotent well and well with induced differentiation. Vertical red lines indicate media change and the first vertical red line indicates introduction of induction media in differentiation cells (22.5 hrs).

One might assume that the sudden rise for the differentiation well, shows that the cells change their morphology very quickly, however the pluripotent well also shows immediate increase (smaller in comparison though) after the first media change. This could simply be due to cell growth and electrode coverage similar to the MDCK cell experiments. It would require further experiments (with time lapse) to ascertain the actual reason or reasons that cause this rapid change. The rapid variations in the impedance results for the differentiation well make it difficult to consider the absolute impedance as a factor of differentiation. The Δ|Z| at 20 Hz for the differentiation well also falls after approximately 50 hrs, making it further more confusing. Could it be that the stem cells loose adhesion after a certain time point? However at higher frequencies Δ|Z| is still consistent which would mean that the cells are still adhering.

Let us focus on the behavior of changes for various frequencies instead. The Δ|Z| of the different frequencies of the pluripotent well tends to reach a particular value and then seems to be consistant. The phase values for the three frequencies are also settled after approximately 45 hrs as well. The differentiation well has similar values for phase but after approximately 70 hrs, the phase at 3 kHz and 10 kHz starts increasing (that is, becoming less negative). This observation is consistent for all the differentiation wells (Figure 74). Thus I considered looking at the spectrums at various time points for each of the wells as shown in Figure 76. Impedance values may go up and down but the frequency of the phase minimum (or the minimum phase frequency), for the pluripotent well (well4), is lower than the minimum phase frequency of the differentiation well (well6) at 90 hrs.

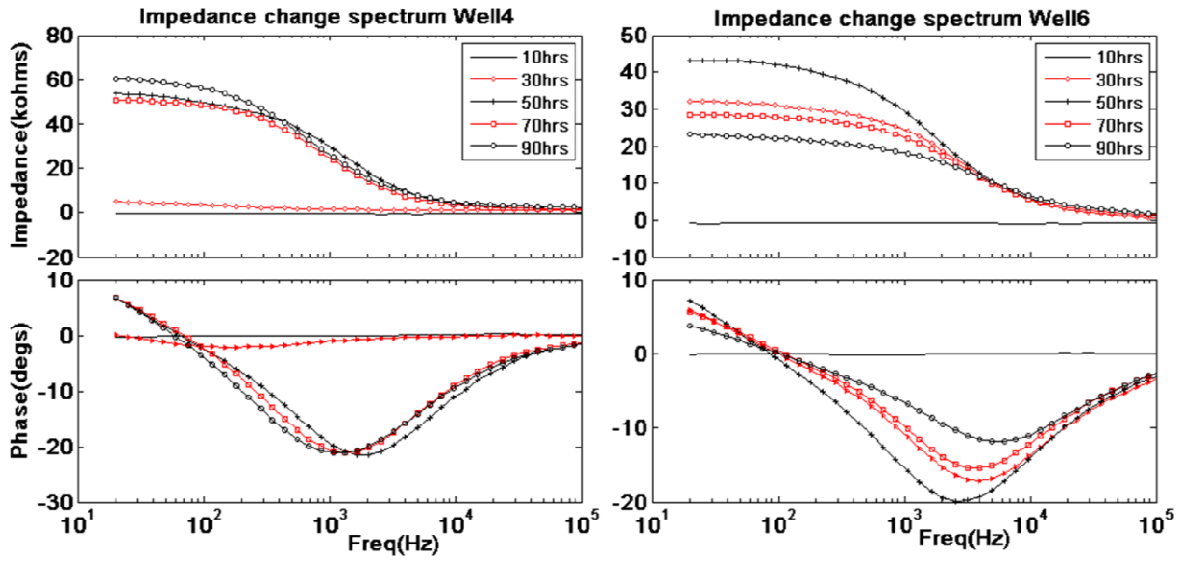

Figure 76: Impedance spectrum for well4 and well 6

Considering this observation I looked at the minimum phase frequencies over the experiment time period, shown in Figure 77. We can see a clear distinction between the mean value, with well4 approximately 550 Hz and well 6 approximately 1600 Hz. There are some quantization errors in the measured values which are limited by the measurement setup. It can be reduced by increasing the total frequency points. However these results show there is a possible factor which could be used to clearly distinguish between pluripotent and differentiated cell cultures using the minimum phase frequency. After 70 hrs, the values become even further apart.

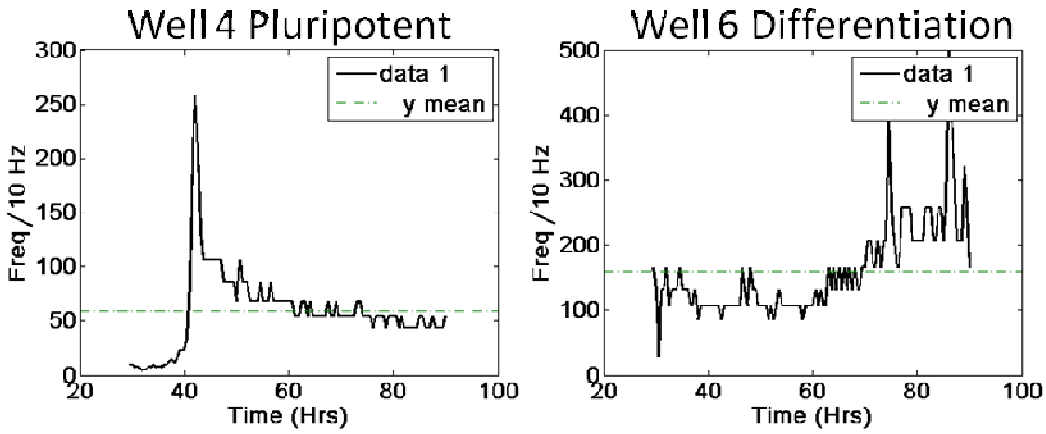

Figure 77: Resonant frequency plots for well 4 and well 6. Green line shows the mean value for all the data points (measurements shown are for after 30 hrs).

Using this method we can collect data from the two wells and the bar plots in Figure 78 show a clear distinction in the phase minimum frequencies for the two different cell types. The results shown in Figure 78 were calculated by taking the mean of the frequencies from the total experiments of the particular cell type. The error bars were

created using the standard deviation of those results. The pluripotent cells types show lower phase minimum frequencies in comparison to the differentiated cell types. If the cells are considered as electrical elements, this shows that the pluripotent cell layer has a larger capacitance value. Just as we saw with the MDCK, the effect due to confluent layers on the impedance is far greater than that due to a single cell or complete electrode coverage by multiple cells as well. The fact that the values become further apart after 70 hrs raises the question of whether this is due to the cells reaching confluence after the time period or is it due cells completing their differentiation cycle. An interesting observation was that all the differentiated wells had a similar increase after 70 hrs and the differentiation cycle for these cells is approximately 72 hrs. To completely disprove the possibility that the frequency is dependent on the cell type and not the confluence, we would need to perform multiple observations of the cells at different time points.

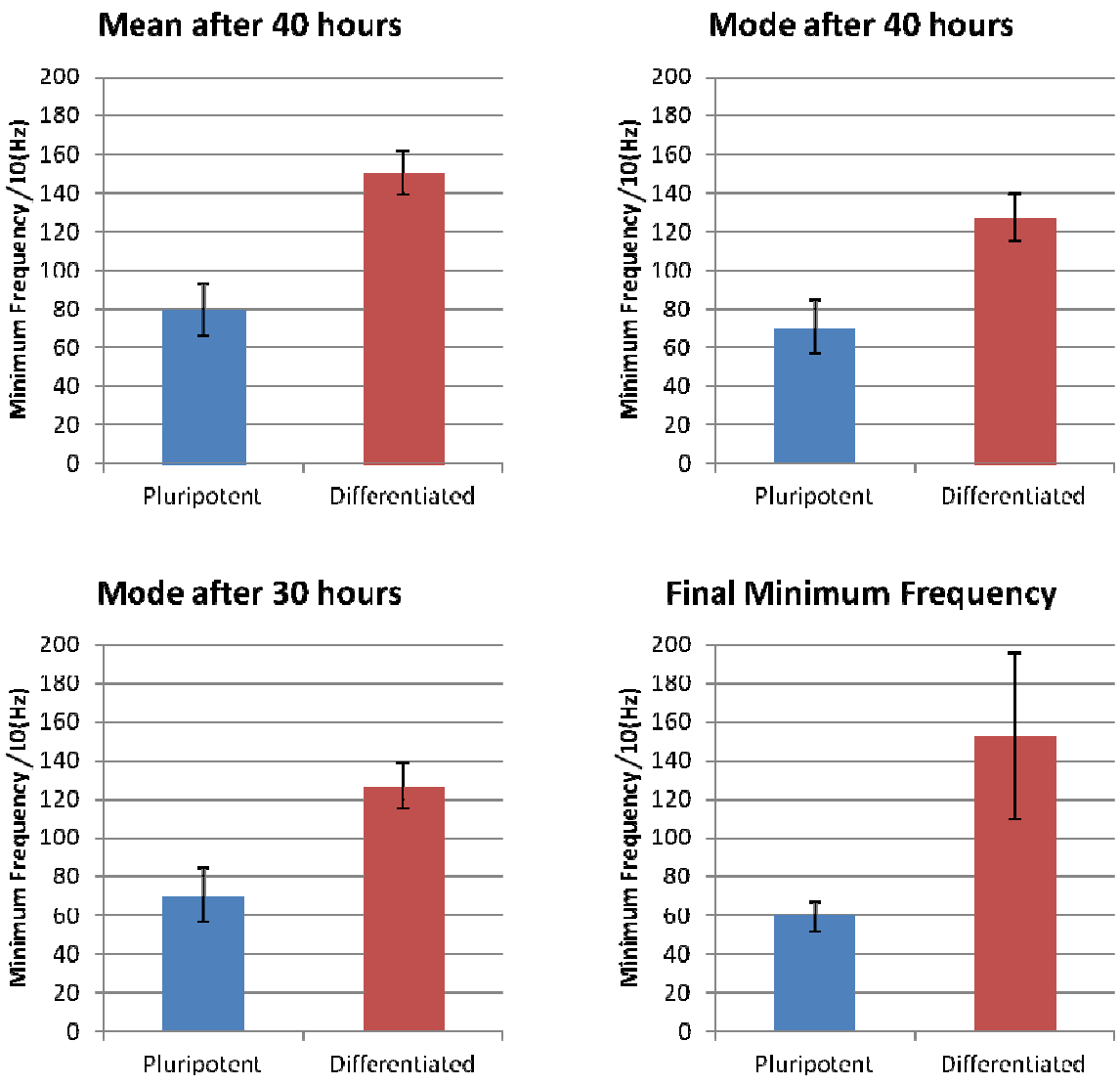

Figure 78: Statistical results for the resonant frequency measurements for all wells. The red line seperate the two types of cells, left are pluripotent and those on the right a differentiated cells.

Figure 79 shows the fluorescent images of at the end of the experiment. Here, the cells have been stained for the pluripotency transcription factor OCT4 (red), the actin filaments (green) and the nucleus using DAPI stains. The top three pictures are for the pluripotent wells. The bottom four are for the differentiation wells. The differentiation wells have lost their pluripotency and show either none, or very little OCT4. This helps validate the results in Figure 78.

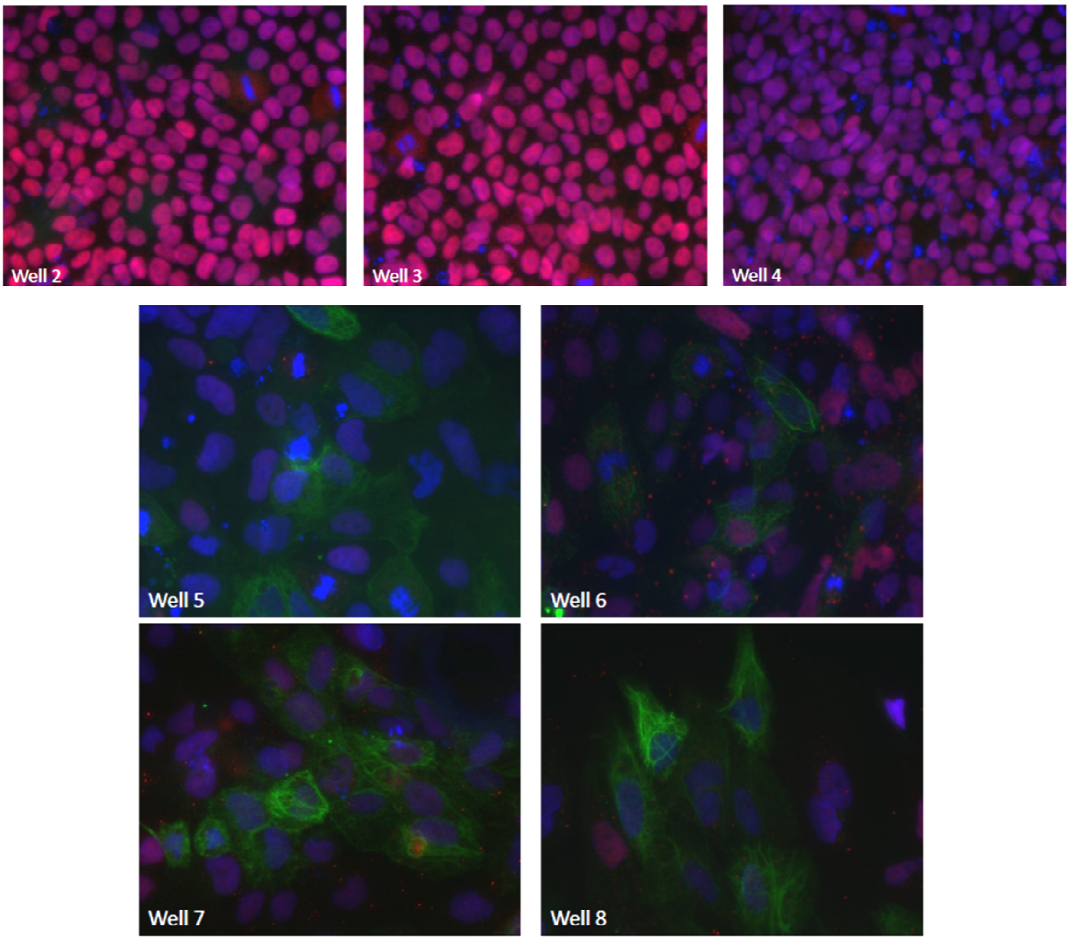

Figure 79: Fluorescent images at the end of the experiment. Blue stain is the DAPI stain for the nucleus. Red shows the OCT4 marker in the pluripotent cells and the green stains are for the actin. Wells 2-4 show the OCT4 stain, proving their pluripotency. Wells 5-8 do not show OCT4 (or very small traces) and hence most cell in those wells have differentiated.

One issue encountered during these experiments was that the stem cells do not differentiate very well if the density of the cells is too high. They also make it difficult to stain them. This creates a problem as the CIS measurement procedure used in this project, works best with confluent layers as explained in section 6.2. Finding the perfect balance has been difficult and reduced the success output of our experiments. I am working towards improving the cell impedance model and measurement procedure as well as improving our experimental technique with Scott in order to get more results and make this technique more reliable.

Chapter 8: **Microstructure Devices to Measure Deformation of Cells**

One of the interests for our research was to explore new forms of electrodes and applications of CIS. It was why we opted to devise a complete fabrication procedure so that we could customize our devices rather than to depend on commercially available products. One interesting idea was put forward by Dr. Mathis Riehle which was based on research published by Davidson *et al.* [136]. They have shown how cell nuclei can deform on microstructures into the gaps. They found that cancerous cell lines deform and take shape of the micro pillars that had dimensions closely related to those of a cell nucleus. They cultured SaOs-2 and MG-63 cells on micro pillars (squares of 7 µm by 7 µm and 4 µm tall) and show that the cell deforms into the grooves and the nucleus deforms to fit inside or partly stretches on top of the pillars while hanging into the grooves(Figure 80 and Figure 81). When HOP cells were cultured onto the structures they were not as flexible and while they did adhere to the surface, they did not deform. Therefore it is assumed that the cell behavior on such a structure is related to the flexibility of the cell type.

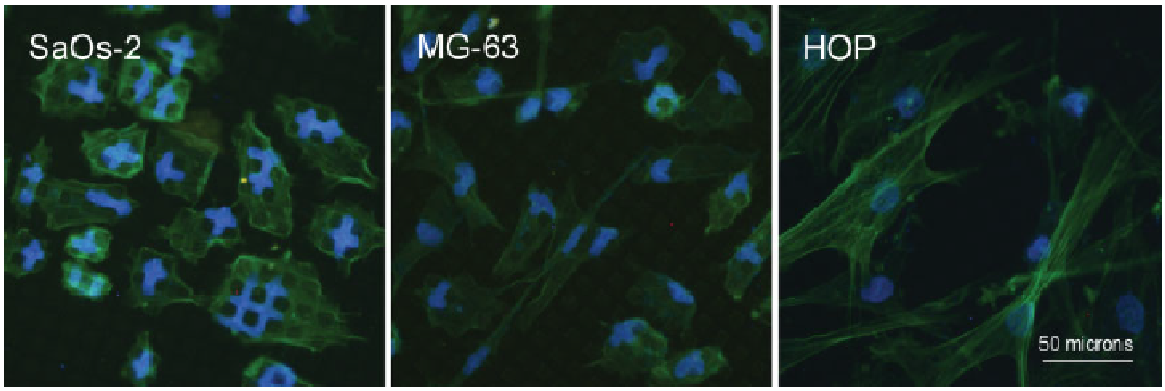

Figure 80: Deformation of cells over microstructures. SaOs-2 and MG-63 are cancerous cell lines, showing deformation, and HOP are osteoblasts. Picture by Davidson *et al*[136].

Davidson *et al* have used this behavior to distinguish between cancerous and non-cancerous cell lines owing to their different flexibilities. I aimed to use CIS, along with this behavior of cells, to see if there is any possibility of using the two techniques to distinguish between the two cell types in real time using impedance changes. Due to shortage of time,

I was not able to prepare the microstructures on PEDOT:PSS electrodes, learn to work with cancerous cell lines and present the work here. This is ongoing, however I was able to try some preliminary experiments of trying a similar theory to measure differentiation in hESCs using Au electrode devices with similar microstructures. The results presented here are not to prove the concept but simply to present work under progress and the observations made.

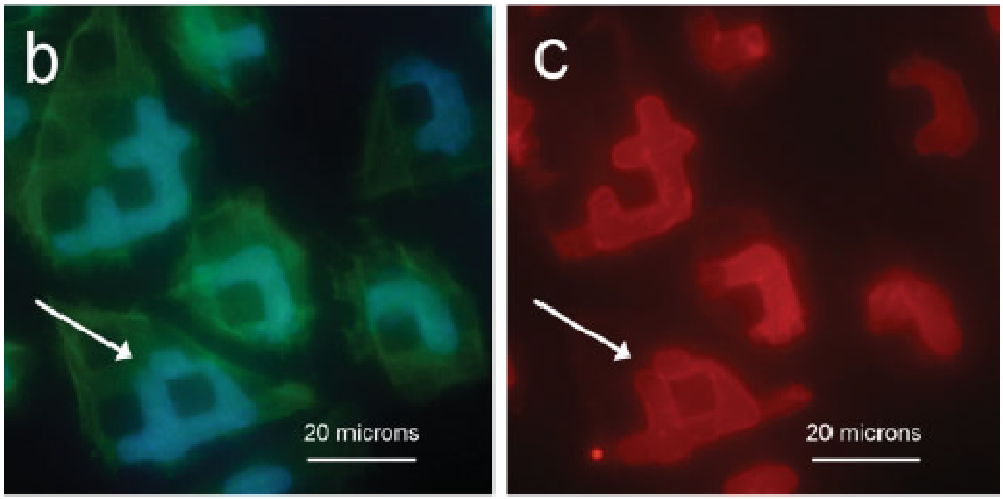

Figure 81: The nucleus doesn't necessarily slip into the groves, it can also stretch over the pillar as shown on the left. The blue stain is for the DNA, the green is for the cytoskeleton and the red is for the nucleus membrane.

The microstructures on the device were similar to that used by Davidson *et al.* These were square shaped pillars, 7 μm x 7 μm dimensions spaced 7 μm apart (in all four directions) but were 6 μm high, something that will be rectified in future experiments. The optical images of a single well (well3) where the hESCs were induced to differentiate into trophoblasts are shown in Figure 82. Image (b) shows the Oct4 marker expression in the cells. By taking a closer look at two regions of varying brightness, on top of the microstructure, we find that not all the cells have lost their pluripotency. However the images show that the pluripotent cells deform more into the pattern than the trophoblasts. This could lead to an interesting change in the impedance which could help show cell differentiation. Figure 83 shows the impedance measured during the course of the experiment over two frequencies. Well1 was the control, well2-5 were induced, and wells 6-8 were to remain pluripotent. We can see a sudden rise in the $\Delta|Z|$ the moment BMP4 is added to the wells. This is something we did not see in the experiment (which showed very good results when stained) shown in Figure 74 in Chapter 7: , however it is something I have observed in other experiments and may be related to higher density of cells. We can

also see the rapid fall and rise of the impedance when media is changed, similar to the MDCK experiment of Figure 62, and it is more prominent in the differentiation wells. The pluripotent cells do not get affected in a similar manner. It could be an indication of how cell that are undergoing a differentiation cycle are sensitive to changes in surroundings. They possibly lose their adhesion and gain it very quickly once the conditions are normalized.

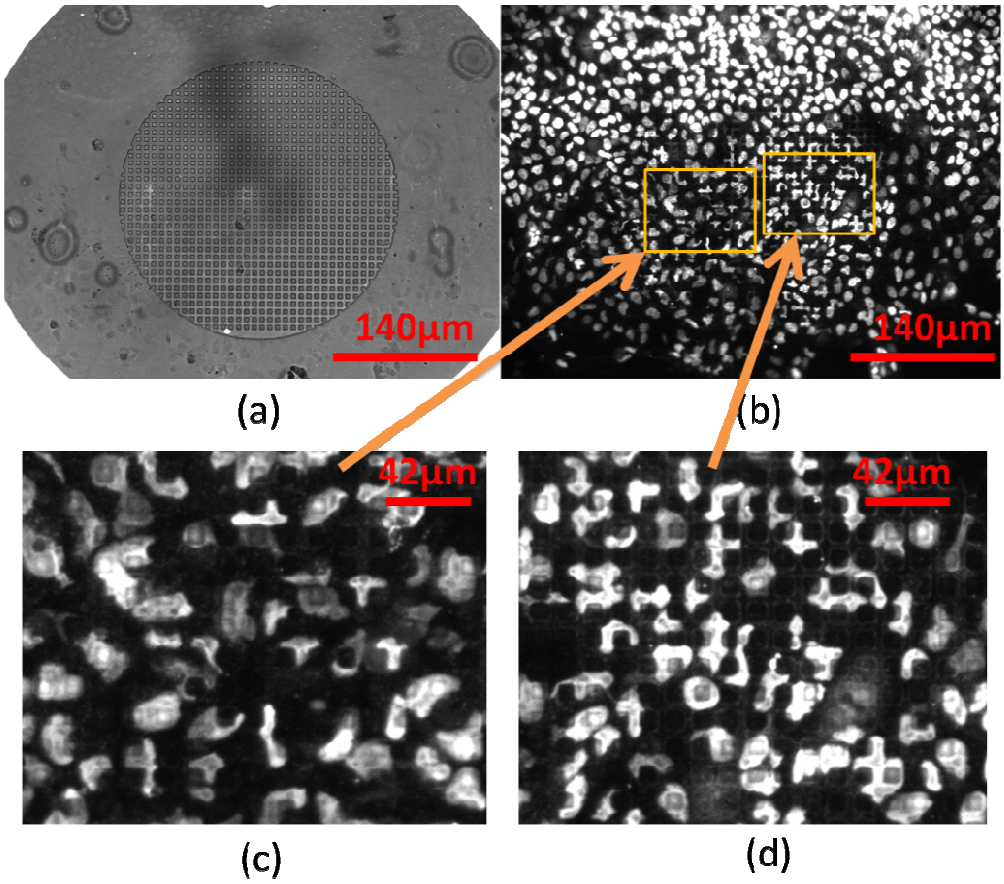

Figure 82: Some preliminary results of stem cell differentiation on microstructure pillars. (a) shows the microstructure pillars on a gold electrode. (b) shows Oct4 pluripotency marker fluorescent image on the same electrode at the end of the experiment. The cells shown in (c) show lower Oct4 than those in (d), and they (cell in (d)) also deform more than those in (c).

Figure 83 shows the impedance results. The differentiation wells show higher $\Delta|Z|$ at the beginning and then after approximately 60 hrs it begins to fall. The results, especially those at 1 kHz, show the impedance of the differentiation wells falling below that of the pluripotent ones. Another thing to notice is that at 1 kHz, $\Delta\theta$ for differentiation wells increases with increasing $\Delta|Z|$ just when BMP4 is induced, and then at the end this relationship changes to increasing $\Delta\theta$ but decreasing $\Delta|Z|$. This could be an indication of the cell deformation reducing for trophoblasts, as shown in Figure 82. Now is this due to

the stiffness of the cytoskeleton and cell functionality, or if it is due to the change in size? This can only be answered by some more experiments looking into the size changes and further analysis. The experiments with a flat PEDOT:PSS electrode (Figure 74) show similar reduction in the impedance and this creates ambiguity with regards to the effect of the stiffness of the cells and the microelectrode device impedance results. However the impedance changes in with these microstructured devices could look more distinct between each well and could be an improvement on the flat electrodes.

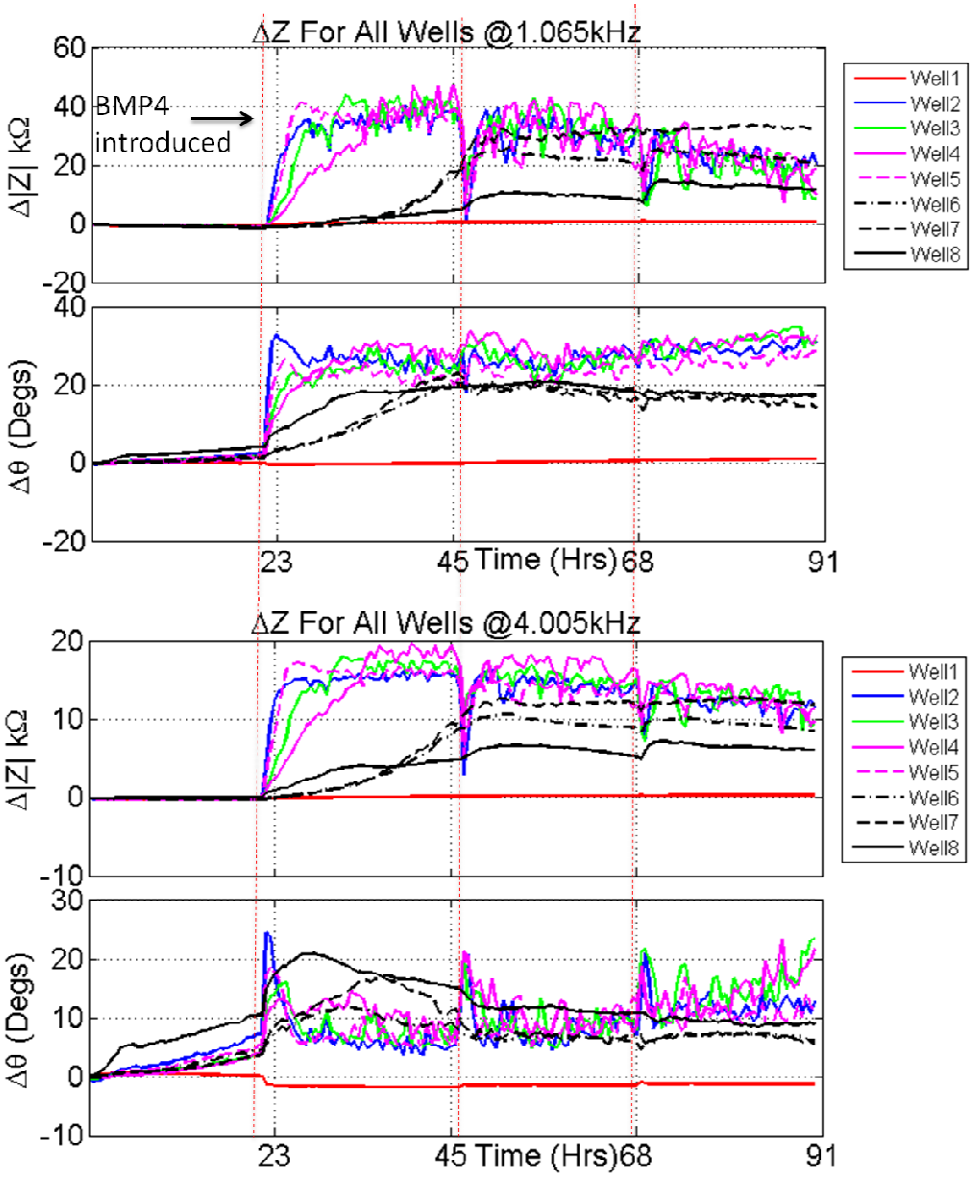

Figure 83: Results of the experiment over two different frequencies. The thin dotted red lines indicate media change and microscopy time points. Well 1 was the control, well 2,3,4 and 5 were induced using BMP4, and wells 6,7 and 8 were maintained as pluripotent and no BMP4 was added to them.

Unfortunately this is only one experiment, which I am not fully confident of especially since we lost the pluripotent wells during removal of the glued wells, thus losing

the possibility of optical observations for the stains of pluripotent wells. The cells have not fully differentiated in the others either, most probably due to the high density of cells when seeded, hindering the process. These images however do show some interesting properties that should be explored further. It would be most beneficial to look at the impedance results of such an experiment using PEDOT:PSS electrodes where lower frequencies can be measured more accurately and the phase changes modeled to the circuit model discussed in section 6.2. Another issue that took place, as mentioned in the earlier section was that the electrode area was halved due to the microstructures. This would need to be tackled else it could lead to a wider and less effective phase result as observed by myself during the course of my work.

Chapter 9: **Conclusion**

The application of conducting polymers, particularly PEDOT:PSS, to CIS is potentially very interesting. The work here has shown how it can improve the measurement capabilities of the technique due to its inherent ability of fast charge transfer with an electrolyte. Its properties of transparency and biocompatibility make it ideal for cell culturing and being a polymer, it presents the possibility of integration with topographies. Furthermore, the many options of processing PEDOT:PSS, especially through aqueous solution based processes, give it a great advantage in commercial manufacturing. Coupled with the use of SU-8 photo resist for insulation, the work presented here also shows that opportunity of using only polymers (including substrate) to create culture wells for CIS applications.

A complete setup for the impedance measurement of devices inside an incubator was developed and implemented. This involved the integration of commercial impedance measurement with software developed using LabView. A platform for connection to custom made devices for cell culturing was designed and developed using SMD components integrated onto a PCB. This platform also included the multiplexers that would allow multiple experiments to be monitored and measurements performed using a 4 probe connection for higher accuracy. The setup allowed measurements of up to 8 different cell cultures over multiple frequencies. It allows the user to control the time between each set of measurements, displays graphs, stores the data for the experiment and also copies that data to a network drive for mobile access. Matlab scripts were made for reading the data and generating custom graphs as well as performing curve fit analysis.

While the development of the device was aimed towards cost effectiveness and simplicity, it was not trivial. Conducting polymers must be processed with great care and the fabrication procedure needs to be optimized in order to achieve good reliability and life span of the device as well as similar electrochemical characteristics between different devices. While using Inkjet printing is useful for prototyping, it does not provide a homogenous surface and reproducibility that can be achieved through spin coating and photolithography. Gravure printing would improve the time required to process, but such techniques are best left for mass manufacturing else they can be costly and reduce the

flexibility for making changes, which is a necessity for research. Temperature processing is critical for the fabrication process and will not only affect the morphology of the electrodes but also the subsequent impedance and measurements when used for CIS. Another thing which is critical is the oxidation using bleach. This method is extremely simple and provided good results. However it cannot be used for high resolution patterning as the solution penetrates under the masking layer and oxidizes more parts of the polymer then required. Coupled with the fact that oxidized PEDOT:PSS is not entirely a complete insulator, and hence must etched off completely, this restrains us from shortening the time of exposure to the oxidizing agent and limits the resolution of the technique further. To create smaller dimensions requires using techniques such as reactive ion etching. Such complications can be easily eluded by changing the design, such as those used for the devices used in this study. By using larger electrode dimensions but smaller windows in the insulation we can have smaller electrode geometries which satisfy the requirements for CIS.

The electrochemical characteristics of PEDOT:PSS have also shown promising results for its use in CIS. Its lower interfacial impedance means that lower frequencies can be measured with more accuracy and lower noise due to electrochemical changes in the media. This lower interfacial impedance is due to the fast charge transfer between PEDOT:PSS electrodes with the electrolyte which stems from its ability to absorb ions and solvent into itself. It is less sensitive, in comparison with Au electrodes, to the changes in media at lower frequencies as the absolute impedance values are far lower. While the absorption of water and ions significantly reduces the interfacial impedance, it also creates a disadvantage when using the polymer as an electrode. Due to the water absorption it tends to lose adhesion to the substrate. This reduced the overall life span of the electrodes when in aqueous media. One thing to consider is that the substrates used in this study were glass and PEDOT:PSS has better adhesion to polymers than glass substrates. This could be rectified by using the polymer blending devised by T. Hansen *et al* [44]. They have managed to integrate PEDOT:PSS and PMMA creating a more mechanically stable conducting polymer layer on a polymer substrate. By using polymer substrates we could eradicate the problem. Another method would be to create a new polymer blend by cross linking PEDOT and PMMA as shown by G. Zhang *et al* [137]. This may affect the electrochemical behavior of the electrode and would need to be characterized further. If the adhesion is still insufficient, we could fabricate the electrodes in such a way as to slightly emboss the electrode into the polymer substrate, while it is at glass transition.

The PEDOT:PSS electrode devices were successfully tested with MDCK cells. The results were compared with those from Au electrodes. The results showed significant improvement in the measurements for lower frequencies and more stability over time. When changes in impedance due to cells were measured, they showed a uniquely different phase result in comparison to that shown by the Au electrodes. When the changes were observed over the entire frequency spectrum, they were found to mimic an electrical circuit, a parallel resistor and capacitor in series with another resistor. This was used to model the cell impedance against a mathematically defined electrical circuit and the values of the individual elements plotted over time. This provided information about the cell substrate adhesion and the cell behaviour. This technique is not novel and has been performed by others, but the electrical model used was slightly different and simpler to implement. The model does not fit perfectly and requires more work to be improved.

Since the implementation of conducting polymers to CIS was successful, the devices and measurement setup were applied to the study human embryonic stem cell differentiation in real time. The experiments involved measuring the impedance of the pluripotent cells during proliferation and then during differentiation to trophoblasts, after being induced using BMP4. The results showed differences in absolute impedance immediately after induction. In order to find further distinctness in impedance of the two cell types, the impedance spectrums were observed closely and analyzed. Results showed that the frequency of the curve minima for the phase change over time, were distinct for the two cell types. This has the potential to become a new method of using CIS to analyze stem cell differentiation.

The idea of distinguishing cell types based on the flexibility and adaptability of the cytoskeleton of cells, as shown by Davidson *et al* [136], was also explored. Devices were fabricated using Au electrodes with square shaped micro pillars on them. Preliminary results using stem cells show pluripotent cells being more adaptable and sinking into the grooves of the microstructures. The trophoblasts show less flexibility in comparison. This is a highly promising application of CIS and further work is ongoing to prove the concept.

References

1. Chin, C.D., V. Linder, and S.K. Sia, *Commercialization of microfluidic point-of-care diagnostic devices.* Lab on a Chip, 2012.

2. Giaever, I. and C.R. Keese, *Micromotion of mammalian cells measured electrically.* Proceedings of the National Academy of Sciences of the United States of America, 1991. **88**(17): p. 7896-7900.

3. Keese, C.R. and I. Giaever, *A biosensor that monitors cell morphology with electrical fields.* Engineering in Medicine and Biology Magazine, IEEE, 1994. **13**(3): p. 402-408.

4. Keese, C.R., *et al.*, *Real-time impedance assay to follow the invasive activities of metastatic cells in culture.* BioTechniques, 2002. **33**(4): p. 842-4, 846, 848-50.

5. Curtis, T.M., *et al.*, *A portable cell-based impedance sensor for toxicity testing of drinking water.* Lab on a Chip, 2009. **9**(15): p. 2176-2183.

6. Xie, F., *et al.*, *Use of cellular electrical impedance sensing to assess in vitro cytotoxicity of anticancer drugs in a human kidney cell nephrotoxicity model.* Analyst, 2012. **137**(6): p. 1343-1350.

7. Angstmann, M., *et al.*, *Monitoring human mesenchymal stromal cell differentiation by electrochemical impedance sensing.* Cytotherapy, 2011. **13**(9): p. 1074-1089.

8. Hildebrandt, C., *et al.*, *Detection of the osteogenic differentiation of mesenchymal stem cells in 2D and 3D cultures by electrochemical impedance spectroscopy.* Journal of Biotechnology, 2010. **148**(1): p. 83-90.

9. Reitinger, S., *et al.*, *Electric impedance sensing in cell-substrates for rapid and selective multipotential differentiation capacity monitoring of human mesenchymal stem cells.* Biosensors and Bioelectronics, 2012. **34**(1): p. 63-69.

10. Qiu, Y., R. Liao, and X. Zhang, *Real-Time Monitoring Primary Cardiomyocyte Adhesion Based on Electrochemical Impedance Spectroscopy and Electrical Cell−Substrate Impedance Sensing.* Analytical Chemistry, 2008. **80**(4): p. 990-996.

11. Haas, S., *et al.*, *Real-time monitoring of relaxation and contractility of smooth muscle cells on a novel biohybrid chip.* Lab on a Chip, 2010. **10**(21).

12. Snook, G.A., P. Kao, and A.S. Best, *Conducting-polymer-based supercapacitor devices and electrodes.* Journal of Power Sources, 2011. **196**(1): p. 1-12.

13. Bobacka, J., *Conducting Polymer-Based Solid-State Ion-Selective Electrodes.* Electroanalysis, 2006. **18**(1): p. 7-18.

14. Gerard, M., A. Chaubey, and B.D. Malhotra, *Application of conducting polymers to biosensors.* Biosensors and Bioelectronics, 2002. **17**(5): p. 345-359.

15. McNeill, R., D. Weiss, and D. Willis, *Electronic conduction in polymers. IV. Polymers from imidazole and pyridine.* Australian Journal of Chemistry, 1965. **18**(4): p. 477-486.

16. B A Bolto, R.M.a.D.W., *Electronic Conduction in Polymers. III. Electronic Properties of Polypyrrole.* Australian Journal of Chemistry 1963. **16**(6): p. 1090.

17. Inzelt, G., *Conducting Polymers: A New Era in Electrochemistry.* 2008.

18. Chiang, C.K., *et al*., *Electrical Conductivity in Doped Polyacetylene.* Physical Review Letters, 1977. **39**(17): p. 1098-1101.

19. Burroughes, J.H., C.A. Jones, and R.H. Friend, *NEW SEMICONDUCTOR-DEVICE PHYSICS IN POLYMER DIODES AND TRANSISTORS.* Nature, 1988. **335**(6186): p. 137-141.

20. Pope, M. and C.E. Swenberg, *Electronic processes in organic crystals and polymers*1999: Oxford University Press.

21. Kumar, D. and R.C. Sharma, *Advances in conductive polymers.* European Polymer Journal, 1998. **34**(8): p. 1053-1060.

22. Guimard, N.K., N. Gomez, and C.E. Schmidt, *Conducting polymers in biomedical engineering.* Progress in Polymer Science, 2007. **32**(8-9): p. 876-921.

23. Zinger, B. and L.L. Miller, *Timed release of chemicals from polypyrrole films.* Journal of the American Chemical Society, 1984. **106**(22): p. 6861-6863.

24. Abidian, M.R., D.-H. Kim, and D.C. Martin, *Conducting-Polymer Nanotubes for Controlled Drug Release.* Advanced Materials, 2006. **18**(4): p. 405-409.

25. Wong, J.Y., R. Langer, and D.E. Ingber, *Electrically conducting polymers can noninvasively control the shape and growth of mammalian cells.* Proceedings of the National Academy of Sciences of the United States of America, 1994. **91**(8): p. 3201-3204.

26. Serra Moreno, J., *et a*l., *Synthesis and characterization of new electroactive polypyrrole-chondroitin sulphate A substrates.* Bioelectrochemistry, 2008. **72**(1): p. 3-9.

27. Kip, A.L. *et al.*, *Chronic neural recordings using silicon microelectrode arrays electrochemically deposited with a poly(3,4-ethylenedioxythiophene) (PEDOT) film.* Journal of Neural Engineering, 2006. **3**(1): p. 59.

28. Thaning, E.M., *et al., Stability of poly(3,4-ethylene dioxythiophene) materials intended for implants.* Journal of Biomedical Materials Research Part B: Applied Biomaterials, 2010. **93B**(2): p. 407-415.

29. Yang, J., *et al., Ordered surfactant-templated poly(3,4-ethylenedioxythiophene) (PEDOT) conducting polymer on microfabricated neural probes.* Acta Biomaterialia, 2005. **1**(1): p. 125-136.

30. Guan, J.-G., Y.-Q. Miao, and Q.-J. Zhang, *Impedimetric biosensors.* Journal of Bioscience and Bioengineering, 2004. **97**(4): p. 219-226.

31. Kros, A., *et al., Poly(3,4-ethylenedioxythiophene)-Based Glucose Biosensors.* Advanced Materials, 2001. **13**(20): p. 1555-1557.

32. Berggren, M. and A. Richter-Dahlfors, *Organic Bioelectronics.* Advanced Materials, 2007. **19**(20): p. 3201-3213.

33. Okuzaki, H., H. Suzuki, and T. Ito, *Electrically driven PEDOT/PSS actuators.* Synthetic Metals, 2009. **159**(21-22): p. 2233-2236.

34. Peng, H., *et al., Conducting polymers for electrochemical DNA sensing.* Biomaterials, 2009. **30**(11): p. 2132-2148.

35. Simon, D.T., *et al. An organic electronic ion pump to regulate intracellular signaling at high spatiotemporal resolution*. in *Solid-State Sensors, Actuators and Microsystems Conference, 2009. TRANSDUCERS 2009. International*. 2009.

36. Hansen, T.S. *et a*l., *An all-polymer micropump based on the conductive polymer poly(3,4-ethylenedioxythiophene) and a polyurethane channel system.* Journal of Micromechanics and Microengineering, 2007. **17**(5): p. 860.

37. Rylie, A.G. *et al., Conducting polymer-hydrogels for medical electrode applications.* Science and Technology of Advanced Materials, 2010. **11**(1): p. 014107.

38. van Dijken, A., *et al., The influence of a PEDOT:PSS layer on the efficiency of a polymer light-emitting diode.* Organic Electronics, 2003. **4**(2–3): p. 131-141.

39. del Valle, L.J., *et al., Cellular Adhesion, Proliferation and Viability on Conducting Polymer Substrates.* Macromolecular Bioscience, 2008. **8**(12): p. 1144-1151.

40. Groenendaal, L., *et al., Poly(3,4-ethylenedioxythiophene) and Its Derivatives: Past, Present, and Future.* Advanced Materials, 2000. **12**(7): p. 481-494.

41. Dietrich, M., *et al., Electrochemical and spectroscopic characterization of polyalkylenedioxythiophenes.* Journal of Electroanalytical Chemistry, 1994. **369**(1–2): p. 87-92.

42. Jonas, F. and L. Schrader, *Conductive modifications of polymers with polypyrroles and polythiophenes.* Synthetic Metals, 1991. **41**(3): p. 831-836.

43. Hansen, T.S., *et al., Highly Stretchable and Conductive Polymer Material Made from Poly(3,4-ethylenedioxythiophene) and Polyurethane Elastomers.* Advanced Functional Materials, 2007. **17**(16): p. 3069-3073.

44. Hansen, T.S., *et al., Integration of conducting polymer network in non-conductive polymer substrates.* Synthetic Metals, 2006. **156**(18-20): p. 1203-1207.

45. Asplund, M. *et al., Toxicity evaluation of PEDOT/biomolecular composites intended for neural communication electrodes.* Biomedical Materials, 2009. **4**(4): p. 045009.

46. Yamato, H., M. Ohwa, and W. Wernet, *Stability of polypyrrole and poly(3,4-ethylenedioxythiophene) for biosensor application.* Journal of Electroanalytical Chemistry, 1995. **397**(1-2): p. 163-170.

47. Elin, M.T., *et al., Stability of poly(3,4-ethylene dioxythiophene) materials intended for implants.* Journal of Biomedical Materials Research Part B Applied Biomaterials, 2010. **9999b**: p. NA.

48. Cogan, S.F., *Neural Stimulation and Recording Electrodes.* Annual Review of Biomedical Engineering, 2008. **10**(1): p. 275-309.

49. Venkatraman, S., *et al., In Vitro and In Vivo Evaluation of PEDOT Microelectrodes for Neural Stimulation and Recording.* Neural Systems and Rehabilitation Engineering, IEEE Transactions on, 2011. **19**(3): p. 307-316.

50. Green, R.A., *et al., Conducting polymers for neural interfaces: Challenges in developing an effective long-term implant.* Biomaterials, 2008. **29**(24-25): p. 3393-3399.

51. Reza, M.A., *et al., Conducting-Polymer Nanotubes Improve Electrical Properties, Mechanical Adhesion, Neural Attachment, and Neurite Outgrowth of Neural Electrodes.* Small, 2010: p. NA.

52. Reza, M.A., *et al., Interfacing Conducting Polymer Nanotubes with the Central Nervous System: Chronic Neural Recording using Poly(3,4-ethylenedioxythiophene) Nanotubes.* Advanced Materials, 2009: p. NA.

53. Abidian, M.R., D.H. Kim, and D.C. Martin, *Conducting-Polymer Nanotubes for Controlled Drug Release.* Advanced Materials, 2006. **18**(4): p. 405-409.

54. Randles, J.E.B., *Kinetics of rapid electrode reactions.* Discussions of the Faraday Society, 1947. **1**: p. 11-19.

55. Connick, P., R. Patani, and S. Chandran, *Stem cells as a resource for regenerative neurology.* Practical Neurology, 2011. **11**(1): p. 29-36.

56. Pera, M.F. and P.P.L. Tam, *Extrinsic regulation of pluripotent stem cells.* Nature, 2010. **465**(7299): p. 713-720.

57. Bagnaninchi, P.O. and N. Drummond, *Real-time label-free monitoring of adipose-derived stem cell differentiation with electric cell-substrate impedance sensing.* Proceedings of the National Academy of Sciences, 2011.

58. Hart, H., L.E. Craine, and D. Hart, *Organic Chemistry: A Short Course*2002: Houghton Mifflin.

59. Skotheim, T.A., R.L. Elsenbaumer, and J.R. Reynolds, *Handbook of Conducting Polymers*1998, New York: Marcel Dekker.

60. Jain, S.C. and V. Kumar, *Conducting organic materials and devices*2007: Elsevier/Academic Press.

61. Nardes, A.M., *On the conductivity of PEDOT:PSS thin films*, in *department of Applied Physics*2007, Eindhoven University of Technology: Eindhoven.

62. Stallinga, P., *Electronic Transport in Organic Materials: Comparison of Band Theory with Percolation/(Variable Range) Hopping Theory.* Advanced Materials, 2011. **23**(30): p. 3356-3362.

63. Friedel, B., *et al., Influence of solution heating on the properties of PEDOT:PSS colloidal solutions and impact on the device performance of polymer solar cells.* Organic Electronics, 2011. **12**(10): p. 1736-1745.

64. Kirchmeyer, S. and K. Reuter, *Scientific importance, properties and growing applications of poly(3,4-ethylenedioxythiophene).* Journal of Materials Chemistry, 2005. **15**(21): p. 2077-2088.

65. de Kok, M.M., *et al., Modification of PEDOT:PSS as hole injection layer in polymer LEDs.* physica status solidi (a), 2004. **201**(6): p. 1342-1359.

66. Aleshin, A.N., S.R. Williams, and A.J. Heeger, *Transport properties of poly(3,4-ethylenedioxythiophene)/poly(styrenesulfonate).* Synthetic Metals, 1998. **94**(2): p. 173-177.

67. Onorato, A., *et al., Enhanced conductivity in sorbitol-treated PEDOT-PSS. Observation of an in situ cyclodehydration reaction.* Synthetic Metals, 2010. **160**(21-22): p. 2284-2289.

68. Yu-Sheng Hsiao, W.-T.W., Chih-Ping Chen and Yi-Chun Chen, *High-conductivity poly(3,4-ethylenedioxythiophene):poly(styrene sulfonate) film for use in ITO-free polymer solar cells.* J. Mater. Chem., 2008(18): p. 5948 - 5955.

69. Nardes, A.M., *et al., Conductivity, work function, and environmental stability of PEDOT:PSS thin films treated with sorbitol.* Organic Electronics, 2008. **9**(5): p. 727-734.

70. Snaith, H.J., *et al., Morphological and electronic consequences of modifications to the polymer anode 'PEDOT:PSS'.* Polymer, 2005. **46**(8): p. 2573-2578.

71. Jönsson, S.K.M., *et al.*, *The effects of solvents on the morphology and sheet resistance in poly(3,4-ethylenedioxythiophene)–polystyrenesulfonic acid (PEDOT–PSS) films.* Synthetic Metals, 2003. **139**(1): p. 1-10.

72. Kim, J.Y., *et al.*, *Enhancement of electrical conductivity of poly(3,4-ethylenedioxythiophene)/poly(4-styrenesulfonate) by a change of solvents.* Synthetic Metals, 2002. **126**(2–3): p. 311-316.

73. Ghosh, S. and O. Inganäs, *Nano-structured conducting polymer network based on PEDOT-PSS.* Synthetic Metals, 2001. **121**(1–3): p. 1321-1322.

74. Ouyang, J., *et al.*, *On the mechanism of conductivity enhancement in poly(3,4-ethylenedioxythiophene):poly(styrene sulfonate) film through solvent treatment.* Polymer, 2004. **45**(25): p. 8443-8450.

75. Fan, B., X. Mei, and J. Ouyang, *Significant Conductivity Enhancement of Conductive Poly(3,4-ethylenedioxythiophene):Poly(styrenesulfonate) Films by Adding Anionic Surfactants into Polymer Solution.* Macromolecules, 2008. **41**(16): p. 5971-5973.

76. Bard, A.J. and L.R. Faulkner, eds. *Electrochemical Methods:Fundamentals and Applications*. 2001, John Wiley & Sons: New York.

77. Lasia, A., *Electrochemical Impedance Spectroscopy and its Applications*, in *Modern Aspects of Electrochemistry*, B.E. Conway, J.O.M. Bockris, and R. White, Editors. 2002, Springer US. p. 143-248.

78. *Double layer (interfacial).* [cited 2012; Available from: http://en.wikipedia.org/wiki/Double_layer_(interfacial).

79. Borkholder, D.A., *Cell Based Biosensors Using Microelectrodes*, in *Department of Electrical Engineering*1998, Stanford University.

80. *Gamry Instruments: Basics of Electrochemical Impedance Spectroscopy*.

81. Chang, B.-Y. and S.-M. Park, *Electrochemical Impedance Spectroscopy.* Annual Review of Analytical Chemistry, 2010. **3**(1): p. 207-229.

82. Newman, J., *Resistance for Flow of Current to a Disk.* Journal of The Electrochemical Society, 1966. **113**(5): p. 501-502.

83. Park, S.-M. and J.-S. Yoo, *Peer Reviewed: Electrochemical Impedance Spectroscopy for Better Electrochemical Measurements.* Analytical Chemistry, 2003. **75**(21): p. 455 A-461 A.

84. Kuphaldt, T.R. *Lessons In Electric Circuits*. Available from: http://www.opamp-electronics.com/tutorials/ac_capacitor_circuits_2_04_02.htm.

85. McAdams, E.T., *et al., The linear and non-linear electrical properties of the electrode-electrolyte interface.* Biosensors and Bioelectronics, 1995. **10**(1–2): p. 67-74.

86. Jorcin, J.-B., *et al., CPE analysis by local electrochemical impedance spectroscopy.* Electrochimica Acta, 2006. **51**(8–9): p. 1473-1479.

87. Bisquert, J., *et al., Impedance of constant phase element (CPE)-blocked diffusion in film electrodes.* Journal of Electroanalytical Chemistry, 1998. **452**(2): p. 229-234.

88. Giaever, I. and C.R. Keese, *Micromotion of mammalian cells measured electrically.* Proceedings of the National Academy of Sciences, 1991. **88**(17): p. 7896-7900.

89. Ivar Giaever, C.R.K., *A morphological biosensor for mammalian cells.* Nature, 1993. **366**: p. 591 - 592.

90. Joachim Wegener, C.R.K., Ivar Giaever, *Electric Cell–Substrate Impedance Sensing (ECIS) as a Noninvasive Means to Monitor the Kinetics of Cell Spreading to Artificial Surfaces.* Experimental Cell Research, 2000. **259**: p. 158–166.

91. Lo, C.M., C.R. Keese, and I. Giaever, *Impedance analysis of MDCK cells measured by electric cell-substrate impedance sensing.* Biophysical journal, 1995. **69**(6): p. 2800-2807.

92. Kickler, T.S., *Clinical Analyzers. Advances in Automated Cell Counting.* Analytical Chemistry, 1999. **71**(12): p. 363-365.

93. *Applied Biophysics*. [cited 2012 1 Nov]; Available from: www.biophysics.com.

94. Cho, S. and H. Thielecke, *Electrical characterization of human mesenchymal stem cell growth on microelectrode.* Microelectronic Engineering, 2008. **85**(5-6): p. 1272-1274.

95. Bouafsoun, A., *et al., Evaluation of Endothelial Cell Adhesion onto Different Protein/Gold Electrodes by EIS.* Macromolecular Bioscience, 2007. **7**(5): p. 599-610.

96. Lo, C.-M. and J. Ferrier, *Impedance analysis of fibroblastic cell layers measured by electric cell-substrate impedance sensing.* Physical Review E, 1998. **57**(6): p. 6982.

97. Xiaoqiu, H., *et al., Simulation of microelectrode impedance changes due to cell growth.* Sensors Journal, IEEE, 2004. **4**(5): p. 576-583.

98. Woland, M. *Cytoplasm*. [cited 2012; Available from: http://en.wikipedia.org/wiki/Cytoplasm.

99. Alberts, B., *Essential cell biology*2010, New York; London: Garland Science.

100. *Cell Membrane*. [cited 2012; Available from: http://en.wikipedia.org/wiki/Cell_membrane.

101. Roberts, K.J. *Lecture and Laboratory Notes* [cited 2012; Available from: http://academic.pgcc.edu/~kroberts/Lecture/Chapter%203/nonmemb.html.

102. Nanci, A. and A.R.T. Cate, *Ten Cate's oral histology: development, structure, and function*2003, Michigan: Mosby.

103. Darling, D. *Cell Cycle*. Available from: http://www.daviddarling.info/encyclopedia/C/cell_cycle.html.

104. Bidanset, D.J., *et al., Regulation of cell substrate adhesion: effects of small galactosaminoglycan-containing proteoglycans.* The Journal of Cell Biology, 1992. **118**(6): p. 1523-1531.

105. Childs, G.V. *The actin cytoskeleton*. 2001 [cited 2012; Available from: http://www.cytochemistry.net/cell-biology/actin_filaments_intro.htm.

106. Dejana, E., *Endothelial cell-cell junctions: happy together*. Nat Rev Mol Cell Biol, 2004. **5**(4): p. 261-270.

107. *Embryonic Stem Cells*. [cited 2012; Available from: http://en.wikipedia.org/wiki/Embryonic_stem_cell.

108. Wright, W.E. and J.W. Shay, *Telomere dynamics in cancer progression and prevention: fundamental differences in human and mouse telomere biology.* Nat Med, 2000. **6**(8): p. 849-851.

109. Hayflick, L. and P.S. Moorhead, *The serial cultivation of human diploid cell strains.* Experimental Cell Research, 1961. **25**(3): p. 585-621.

110. Shenghui, H., D. Nakada, and S.J. Morrison, *Mechanisms of Stem Cell Self-Renewal.* Annual Review of Cell and Developmental Biology, 2009. **25**(1): p. 377-406.

111. Morrison, S.J., N. Uchida, and I.L. Weissman, *The Biology of Hematopoietic Stem Cells.* Annual Review of Cell and Developmental Biology, 1995. **11**(1): p. 35-71.

112. Giaever, I. and C.R. Keese, *Use of Electric Fields to Monitor the Dynamical Aspect of Cell Behavior in Tissue Culture.* Biomedical Engineering, IEEE Transactions on, 1986. **BME-33**(2): p. 242-247.

113. DUINEVELD, P.C., *The stability of ink-jet printed lines of liquid with zero receding contact angle on a homogeneous substrate.* Journal of Fluid Mechanics, 2003. **477**: p. 175-200.

114. Derby, B., *Inkjet Printing of Functional and Structural Materials: Fluid Property Requirements, Feature Stability, and Resolution.* Annual Review of Materials Research, 2010. **40**(1): p. 395-414.

115. Stringer, J. and B. Derby, *Formation and Stability of Lines Produced by Inkjet Printing.* Langmuir, 2010. **26**(12): p. 10365-10372.

116. AGFA, O., *Patterning Orgacon™ film by means of UV lithography. Guidelines*, in *Application Sheets*.

117. Zaveri, J., *Micropatterning of Conducting Polymers*, in *Masters Dissertation* 2010, University of Glasgow.

118. Jiang, L., X. Wang, and L. Chi, *Nanoscaled Surface Patterning of Conducting Polymers.* Small, 2011. **7**(10): p. 1309-1321.

119. Hansen, T.S., *et al.*, *Direct Fast Patterning of Conductive Polymers Using Agarose Stamping.* Advanced Materials, 2007. **19**(20): p. 3261-3265.

120. Hernández-Labrado, G.R., *et al.*, *Subdiffusion behavior in poly(3,4-ethylenedioxythiophene): Polystyrene sulfonate (PEDOT:PSS) evidenced by electrochemical impedance spectroscopy.* Journal of Electroanalytical Chemistry, 2011. **659**(2): p. 201-204.

121. Liu, G., Y. Tian, and Y. Kan, *Fabrication of high-aspect-ratio microstructures using SU8 photoresist.* Microsystem Technologies, 2005. **11**(4): p. 343-346.

122. *MemsCyclopedia*. Available from: http://memscyclopedia.org/su8.html.

123. Ru, F. and J.F. Richard, *Influence of processing conditions on the thermal and mechanical properties of SU8 negative photoresist coatings.* Journal of Micromechanics and Microengineering, 2003. **13**(1): p. 80.

124. Atkins, P.P.W. and J. De Paula, *Atkin's Physical Chemistry*2002: Oxford University Press, Incorporated.

125. Richardot, A. and E.T. McAdams, *Harmonic analysis of low-frequency bioelectrode behavior.* Medical Imaging, IEEE Transactions on, 2002. **21**(6): p. 604-612.

126. Bobacka, J., A. Lewenstam, and A. Ivaska, *Electrochemical impedance spectroscopy of oxidized poly(3,4-ethylenedioxythiophene) film electrodes in aqueous solutions.* Journal of Electroanalytical Chemistry, 2000. **489**(1–2): p. 17-27.

127. Tang, R., *Listening to neurons - Development and understanding of microelectrode arrays (MEA's) systems.* University of Glasgow, 2009.

128. Sun, T. and H. Morgan, *Single-cell microfluidic impedance cytometry: a review.* Microfluidics and Nanofluidics, 2010. **8**(4): p. 423-443.

129. Puri, M.C. and A. Nagy, *Concise Review: Embryonic Stem Cells Versus Induced Pluripotent Stem Cells: The Game Is On.* STEM CELLS, 2012. **30**(1): p. 10-14.

130. Mandal, P.K., C. Blanpain, and D.J. Rossi, *DNA damage response in adult stem cells: pathways and consequences.* Nat Rev Mol Cell Biol, 2011. **12**(3): p. 198-202.

131. Nombela-Arrieta, C., J. Ritz, and L.E. Silberstein, *The elusive nature and function of mesenchymal stem cells.* Nat Rev Mol Cell Biol, 2011. **12**(2): p. 126-131.

132. Takahashi, K. and S. Yamanaka, *Induction of Pluripotent Stem Cells from Mouse Embryonic and Adult Fibroblast Cultures by Defined Factors.* Cell, 2006. **126**(4): p. 663-676.

133. Lu, J., *et al.*, *Defined culture conditions of human embryonic stem cells.* Proceedings of the National Academy of Sciences, 2006. **103**(15): p. 5688-5693.

134. Gupta, K., *et al.*, *Lab-on-a-chip devices as an emerging platform for stem cell biology.* Lab on a Chip, 2010. **10**(16): p. 2019-2031.

135. Xu, R.-H., *et al.*, *BMP4 initiates human embryonic stem cell differentiation to trophoblast.* Nat Biotech, 2002. **20**(12): p. 1261-1264.

136. Davidson, P.M., *et al.*, *Microstructured Surfaces Cause Severe but Non-Detrimental Deformation of the Cell Nucleus.* Advanced Materials, 2009. **21**(35): p. 3586-3590.

137. Guandong, Z., V. Chu, and C. Joao Pedro, *Conductive Blended Polymer MEMS Microresonators.* Microelectromechanical Systems, Journal of, 2007. **16**(2): p. 329-335.

138. JENWAY, *The effect of temperature on conductivity measurement*, JENWAY (Bibby Scientific).

139. Haynes, W.M., D.R. Lide, and T.J. Bruno, *CRC Handbook of Chemistry and Physics 2012-2013*2012: CRC Press.

Appendix

Calculation of conductivities for 0.1 M NaCl

We would like to find out the conductivity of a 0.1 M NaCl solution over different temperatures. As the data was not readily available, I used data from JENWAY [138] for the conductivities of various NaCl dilutions as shown in the table below.

Temperature(C)	0.5 g/l	1g/l	10g/l	5.8g/l
5	652	1272	11140	6569
10	746	1462	12760	7594
15	841	1639	14340	8619
20	936	1828	15910	9644
25	1037	2030	17610	10669
30	1136	2230	19180	11694
35	1246	2440	20900	12719
40	1370	2640	23000	13744
45	1470	2870	25000	14769
50	1595	3080	26800	15794

Table 10: Conductivities of NaCl solutions in μS cm^{-1}. The last column shows the results for the calculated conductivities of a 0.1 M solution.

These conductivities are plotted in Figure 84. The gradient of the three dilutions (0.5 g/l, 1 g/l and 10 g/l) are calculated using a linear fit. These gradients are then used to find the slope for a 5.8 g/l (0.1 M) solution (Figure 85) assuming the relationship between the concentration and the gradient is linear. 0.1 M NaCl has a equivalent conductivity of 106.69 cm^2 S mol^{-1} [139] at 25 °C. This means that a 0.1 M solution has a conductivity of 10669 μS cm^{-1}. Hence we can use this to determine the linear equation for the particular concentration and find that the conductivity at 35 °C and 37 °C is 12719 μS cm^{-1} and 13129 μS cm^{-1} respectively. The resistivity is then calculated as 78.62 Ω cm and 76.16 Ω cm. The gaps between the electrode in the device is roughly 3mm which gives us a resistance of 23.5 Ω and 22.8 Ω.

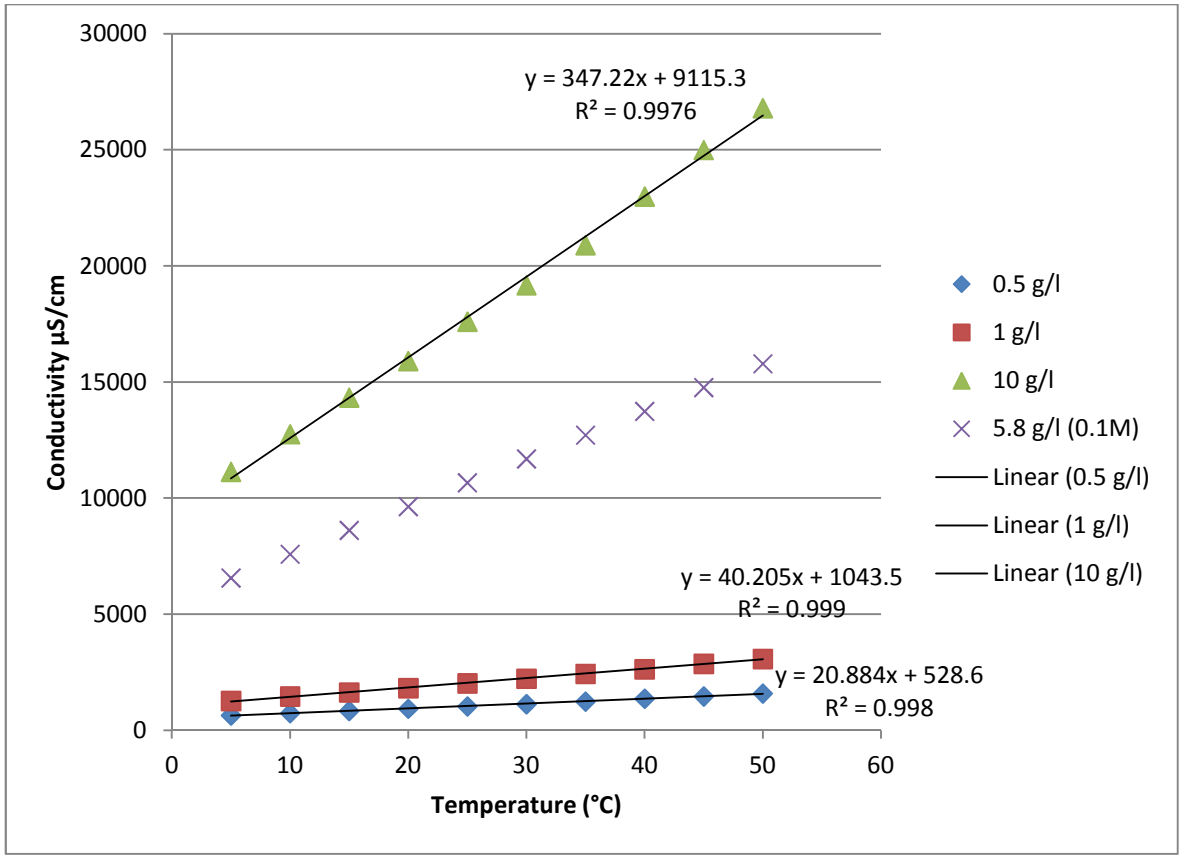

Figure 84: Conductivity of different NaCl solutions plotted against temperature. The equations shown are for the linear fits.

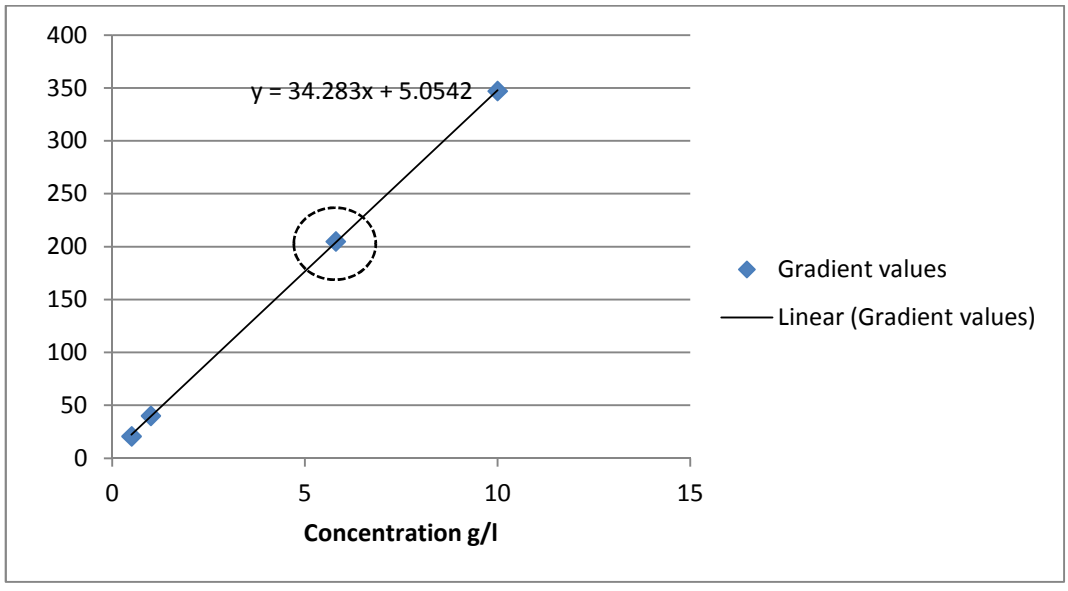

Figure 85: Gradient values for the lines plotted in Figure 84. The point with the circle is the value for 0.1 M NaCl solution.